**TRIBHUVAN UNIVERSITY**

**INSTITUTE OF ENGINEERING**

**PULCHOWK CAMPUS**

**THESIS NO.**: PUL078MSGtE017

# Rainfall Induced Cascading Hazard Modeling: An Integrated Study of Landslides, Floods, and Soil Erosion in the Kankai Basin, Nepal

by

Suman Bahadur Basnet

A THESIS

SUBMITTED TO THE DEPARTMENT OF CIVIL ENGINEERING
IN PARTIAL FULFILLMENT OF THE REQUIREMENTS FOR THE
DEGREE OF MASTER OF SCIENCE IN GEOTECHNICAL
ENGINEERING

DEPARTMENT OF CIVIL ENGINEERING
LALITPUR, NEPAL

APRIL, 2026

## DEDICATION

*This thesis is dedicated to the memory of the unknown families who tragically lost their lives in the devastating landslides and floods of October 2025 in ilam*

## COPYRIGHT

**TRIBHUVAN UNIVERSITY**

**INSTITUTE OF ENGINEERING**

**PULCHOWK CAMPUS**

**DEPARTMENT OF CIVIL ENGINEERING**

The thesis titled "*Rainfall-Induced Cascading Hazard Modeling: An Integrated Study of Landslides, Floods, and Soil Erosion in the Kankai Basin, Nepal*" prepared and submitted by *Suman Bahadur Basnet* in partial fulfilment of the requirements for the degree of Master of Science (M. Sc.) in Geotechnical Engineering has been examined by us and is accepted for the award of M. Sc. in Geotechnical Engineering by Tribhuvan University.

The undersigned certify that they have read and recommended to Institute of Engineering, TU, Nepal, for acceptance, a thesis report entitled "*Rainfall-Induced Cascading Hazard Modeling: An Integrated Study of Landslides, Floods, and Soil Erosion in the Kankai Basin, Nepal*", submitted by *Suman Bahadur Basnet* in partial fulfillment of the requirement for the degree of Master of Science in Geotechnical Engineering.

……

Supervisor

Prof. Dr. **Indra Prasad Acharya**

Department of Civil Engineering,

Pulchowk Campus, IOE, TU, Nepal

……

External Examiner

Er. **Tuk Lal Adhikari**

ITECO Nepal Pvt. Ltd.

……

Program Coordinator

Assist. Prof. Dr. **Bhim Kumar Dahal**

Department of Civil Engineering,

Pulchowk Campus, IOE, TU, Nepal

April, 2026

## DECLARATION

I hereby declare that this study titled "Rainfall-Induced Cascading Hazard Modeling: An Integrated Study of Landslides, Floods, and Soil Erosion in the Kankai Basin, Nepal" is based on my original research work. Related works on the topic by other researchers have been duly acknowledged. I owe all the liabilities relating to the accuracy and authenticity of the data and any other information included hereunder.

……

**Suman Bahadur Basnet**

078 MSGtE 017

M.Sc. in Geotechnical Engineering

Date: April, 2026

## ACKNOWLEDGEMENTS

I would extend my sincere gratitude and heartfelt appreciation to my supervisor Dr. Indra Prasad Acharya (Professor, Pulchowk Campus, IOE, TU, Nepal) for his patient guidance, constant encouragement, and invaluable support throughout my Master's study. His mentorship inspired me to grow both professionally and personally, and his continuous motivation helped me expand my knowledge and confidence as an engineer.

My special thank goes to Dr. Bhim Kumar Dahal (Coordinator, Department of Geotechnical Engineering, Pulchowk Campus, IOE, TU, Nepal) and Dr. Santosh Kumar Yadav (Assistant Professor, IOE, TU, Nepal) for their continuous guidance and encouragement throughout my study. Their consistent support in various aspects greatly contributed to the successful completion of my work. Furthermore, I would like to sincerely thank all the friends and staff of the Department of Geotechnical Engineering at Pulchowk Campus for their support and cooperation. I am especially grateful to Mr. Nir Kumar Karki for his valuable assistance in data collection and report preparation, which significantly contributed to the successful completion of this thesis.

Finally, I express my heartfelt gratitude to my family for their unwavering faith, endless love, and constant encouragement throughout my journey. Their steadfast support has been the foundation of my achievements. I am also deeply thankful to my birthplace, where my path of learning first began.

With heartfelt appreciation

Suman Bahadur Basnet

078 MSGtE 017

## Abstract

The Kankai Basin, extending from the alluvial deposits in the South to the Siwalik at middle and the Lesser Himalayan in the North, is highly susceptible to floods, landslides and bank erosion, threatening infrastructure and local livelihoods. Despite increasing multi-hazard events, hazard–infrastructure interactions remain underexplored in eastern Nepal. This study presents an integrated multi-hazard framework combining machine learning, geospatial analysis, and Monte Carlo simulation to assess associated risks to roads and building infrastructure. A Support Vector Machine was applied to evaluate landslide susceptibility, using a multi-temporal inventory of 842 polygons and 13 conditioning factors including topography, lithology, rainfall, soil, land use, and proximity to roads, rivers, and faults. Similarly, flood susceptibility modeled using 2147 pixels (30 m resolution) of historical flood locations and 17 influencing factors in SVC framework. Soil erosion was estimated through a weighted overlay of six geomorphic and hydrological indicators, complemented by RUSLE calculations. A multi-hazard exposure map was then generated using a weighted overlay approach, with Weights were first assigned using AHP and then tested with Monte-Carlo simulations to reduce uncertainty. Validation showed strong predictive capacity, with landslide and flood simulations achieving accuracies above 0.87 and AUC values near 0.95, along with a spatially heterogeneous multi-hazard pattern across the Basin. Hazard distribution revealed landslides clustering in Siwalik and Lesser Himalayan slopes particularly along MBT zone, floods dominating the Terai plains, and erosion following river corridors and steep slopes, reflecting strong topographic and fluvial controls. Further, overlay analysis showed significant exposure: over 10 % of roads and nearly 5 % of buildings intersected very high-risk zones. Overall, the study demonstrates the effectiveness of integrating geospatial data, machine learning, and GIS for multi-hazard mapping in Himalayan terrain, highlighting its significance resilient land-use planning.

**Keywords:** Cascading Hazards, Landslide Susceptibility, Flood Susceptibility, Soil Erosion, Support Vector Machine, Kankai Basin, Geographic Information System

## List of Figures

# List of Tables

## List of Abbreviations

| | | |
|---|---|---|
| AUC | : | Area under the Curve |
| CBS | : | Central Bureau of Statistics |
| DEM | : | Digital Elevation Model |
| FN | : | False Negative |
| FP | : | False Positive |
| GIS | : | Geographic Information System |
| HKH | : | Hindu Kush Himalayan |
| MCA | : | Multi-Criteria Analysis |
| MHT | : | Main Himalayan Thrust |
| ML | : | Machine Learning |
| NDVI | : | Normalized Difference Vegetative Index |
| RBF | : | Radial Basis Function |
| ROC | : | Receiver Operating Curve |
| SVM | : | Support Vector Machine |
| TN | : | True Negative |
| TP | : | True Positive |

# Table of Contents

*This page is left intentionally blank …*

# 1. INTRODUCTION

## 1.1 Background

In today's interconnected world, every hazard is cascading; few hazards can be considered purely natural (Aksha, Resler, Juran, Jr, et al., 2020; Clarke & Obrien, 2016). Increasingly complex human - environment interactions driven by urbanization, technological advancement, and climate change - have amplified the coexistence and interaction of multiple hazards (Thompson et al., 2024). Multi-hazard risk analysis, though relatively young, has gained attention because single-hazard approaches often underestimate real-world risks (Kappes, 2011). Unlike traditional models, multi-hazard assessment integrates multiple interacting natural hazards - such as landslide, flooding, debris flows, and soil erosion - within a common spatial and temporal framework (A. Shrestha et al., 2023). In monsoon-dominated hilly area, rainfall-induced hazards including landslide, flooding, and soil erosion, are among the most destructive processes, threatening infrastructure, ecosystems, and local economies (De Angeli et al., 2022). Climate change and severe precipitation occurrences have increased both the frequency and severity of these hazards, endangering public safety. Between 2019 and 2023, Nepal experienced an average of approximately 393 fatalities annually, while the global average was 494. By 2024, these figures rose sharply to over 750 fatalities in Nepal and 1,570 globally (K. Lamichhane et al., 2025; Wu et al., 2025).

Nepal, a seismically active country with steep terrain and diverse geology, is among the top 20 multi-hazard-prone countries globally. Its vulnerability ranks 20$^{th}$ in terms of multi-hazards, 4$^{th}$ for hazards connected to climate change, 11$^{th}$ for earthquakes, and 30$^{th}$ for floods (Guragain & Doneys, 2022; Khatakho et al., 2021), with more than 80 % of the population at risk (Rai et al., 2025). Most annual rainfall occurs in the June–September monsoon, driving floods, erosion, and the majority of landslide events. Nepal contributed nearly one-tenth of global landslide fatalities during 2004–2016, highlighting its disproportionate hazard burden (Froude & Petley, 2018). The country is also highly flood-prone, with 7,599 deaths and 6.1 million affected between 1954 and 2018, resulting 10.6 billion USD economic damages (B. R. Shrestha et al., 2020). Soil erosion in Nepal averages 25 t/ha/year (369 Mt

annually), far above the global average of 10 - 15 t/ha/year, causing significant land degradation, particularly in the Siwalik and Lesser Himalayas (S. K. Ghimire et al., 2013).

The Kankai River Basin in eastern Nepal exemplifies these hazards, affecting 231 villages along its banks (Nath & Hudait, 2024). The lower basin is prone to floods and bank erosion, while the upper basin is susceptible to landslides and debris flows. Monsoon-driven high discharge and sediment loads accelerate channel migration, sand deposition, and agricultural land loss, with documented erosion of 628.2 ha and 433.76 ha in different phases (Nath & Hudait, 2024; Silwal et al., 2020). The interplay between geomorphological characteristics and unregulated urban expansion further exacerbates these multi-hazard risks in the basin.

The assessment of infrastructure exposure to natural disasters in Nepal has been a growing concern, particularly after the 2015 Gorkha earthquake sequence (D. Gautam & Dong, 2018). Several quantitative and qualitative techniques have been applied for hazard susceptibility mapping, including heuristic analysis, multi-criteria decision making, weight of evidence (WoE), logistic regression, and fuzzy logic (Aksha, Resler, Juran, Jr, et al., 2020; Bhatta & Adhikari, 2024; Khatakho et al., 2021; Rai et al., 2025). Challenges persist due to small datasets, inadequate multi-temporal validation, and inconsistent weighting of human-induced variables such as roads and slope modifications (R. K. Dahal et al., 2006; Dhungana & Maharjan, 2023). Despite these advances, studies on cascading hazards remain limited, largely due to scarce and outdated data and statistical uncertainties (Acharya, 2018; Le et al., 2023). Efforts to reduce uncertainties in hazard modeling and minimize their damages have been ongoing. The rapid growth of artificial intelligence (AI) and machine learning (ML), combined with satellite imagery, public Earth observation data, and GIS–remote sensing (RS) integration, has greatly enhanced hazard prediction and mapping. Machine learning algorithms such as Random Forest (RF), Support Vector Machine (SVM), and Extreme Gradient Boosting (XG-Boost) have shown high efficacy in multiple hazards prediction in Nepal (S. Lamichhane et al., 2025; Pyakurel et al., 2023; S. Shrestha et al., 2023). This study aims to develop an integrated rainfall-induced cascading hazard model for the Kankai Basin, combining landslide, flood, and soil erosion risks using GIS, remote sensing, machine

learning, and field validation. The results will support the development of multi-hazard emergency preparedness and risk reduction.

## 1.2 Problem Statements

The Hindu Kush Himalayan region is one of the world's most dynamic and fragile mountain systems, characterized by complex geology, steep terrain, intense monsoonal rainfall, and rapid environmental change. Rainfall-induced hazards such as landslides, floods, and soil erosion are among the most destructive processes in these mountainous environments, posing severe threats to infrastructure, ecosystems, and local economies. Countries in this region, including Nepal, are highly seismically active and exposed to multiple hazards, with over 80 % of the population living under significant disaster risk (Khatakho et al., 2021; Rai et al., 2025). Sporadic earthquakes, climate change, and rapid land use change further intensify this vulnerability by destabilizing slopes and triggering secondary hazards, particularly Siwalik & Lesser Himalayan region. Importantly, these processes do not occur in isolation but are interconnected through complex hydrological and geomorphological interactions.

These cascading effects are already evident in the Kankai Basin. Upstream landslides and soil erosion significantly increase sediment loads, which in turn accelerate downstream river aggradation, reduce channel capacity, and intensify flood hazards. In Ilam District, recurrent landslides supply substantial sediment to river systems, affecting downstream infrastructure such as hydropower projects along the Mai Khola. Excessive sedimentation reduces reservoir storage, damages turbines, and threatens long-term project sustainability. Concurrently, channel siltation increases flood risk by reducing flow capacity, leading to bridge overtopping, infrastructure damage, and transport disruption during high-flow events. These interacting processes generate cascading and compound hazard effects, highlighting the need for integrated assessment approaches (D. Gautam et al., 2021). Despite increasing frequency and interconnectedness of these hazards, research in the Kankai Basin remains fragmented and largely single-hazard focused, particularly on landslides or floods in isolation. Moreover, the incorporation of infrastructure exposure, particularly roads and

buildings, into susceptibility assessments remains limited in the basin. This limit understanding of cumulative and interacting risks and hinders identification of critical zones, constraining effective mitigation, adaptation, and land-use planning.

To address these problems, this study develops an integrated framework for rainfall-induced multi-hazard mapping and infrastructure risk assessment (roads and buildings), promoting a shift from fragmented single-hazard approaches to integrated, system-based risk management in the Himalayan region.

### 1.3 Aim & Objectives

The Main objective of this study is to develop a multi-hazard exposure map integrating landslides, floods, and soil erosion in the Kankai Basin and assess associated risks to roads and buildings, thereby supporting improved disaster risk management in the region.

Specific objectives:

1. Analyze the spatial distribution and controlling factors of landslides, flooding, and soil erosion in the Kankai Basin.
2. Assess multi-hazard risk by integrating buildings, road infrastructure, and population vulnerability.
3. Provide scientific information to support disaster risk reduction, sustainable land-use planning, and hazard mitigation.

The following Questions will be addressed in this research:

1. What are the major environmental and geomorphological factors controlling rainfall - induced hazards in the Kankai ?
2. How does integrated exposure of buildings, road infrastructure, and population influence multi-hazard risk in the Kankai ?
3. How can multi-hazard mapping inform disaster risk reduction, sustainable land-use planning, and hazard mitigation ?

These objectives and questions are academically relevant, feasible, and aligned with the growing impacts of multi-hazards and the need for effective disaster risk management.

## 1.4 Scope of the Study

This study aims to assess rainfall-induced multi-hazard risk in the Kankai river Basin, located in Ilam and Jhapa districts of eastern Nepal. The study concentrates on three primary hazards landslides, floods, and soil erosion, which are strongly influenced by rainfall and exhibit significant spatial and process-based interlinkages within the basin. Hydrological modeling with DEM data delineated the basin, applying flow direction and accumulation algorithms. A geospatial framework integrating machine learning and Geographic Information Systems (GIS) is employed to evaluate hazard susceptibility. Multi-source datasets, including satellite imagery, DEM, rainfall data, and existing hazard inventory records, are utilized to generate spatial susceptibility maps. Key conditioning factors considered in the analysis include slope, curvature, drainage density, topographic indices, land use/land cover, and rainfall patterns. Spatial modeling techniques are applied to classify the basin into different susceptibility zones.

Although additional hazards such as debris flows and riverbank erosion are relevant in the study area, they are not modeled explicitly due to limited spatial data availability, their partial representation within landslide and flood processes, and the complexity of basin scale modeling. Nevertheless, their influence is implicitly incorporated within the adopted multi-hazard framework. The scope of this research is limited to multi-hazard risk assessment considering roads & building elements and spatial mapping within the basin and does not include detailed geotechnical investigations, real-time hazard forecasting, or structural mitigation design. Furthermore, the analysis is based on historical datasets. Given that rainfall is the principal triggering factor, future changes in rainfall intensity and variability under changing climatic conditions may alter hazard patterns, potentially expanding landslide-prone areas, increasing flood susceptibility in the Terai plains, and intensifying soil erosion processes. Despite these limitations, the study provides a systematic understanding of the spatial distribution and interaction of rainfall-induced hazards. Findings provide actionable insights for disaster risk reduction, land-use planning, watershed management, and safeguarding infrastructure by identifying high-risk zones and prioritizing mitigation strategies.

## 1.5 Limitations

Although the study offers contributions to both methodological and practical domains, it is subject to some limitations that introduce uncertainty in the results.

- Limited hydrometeorological, sediment, landslide, and flood data, especially in upstream areas.

- Low-resolution DEM (30 m) and reliance on Google Earth imagery introduce scale and cloud-related uncertainties.

- GIS-based model (AHP, Weighted Overlay) and empirical models (RUSLE) simplify processes and do not fully capture cascading hazards and their quantitative inter-relationships.

- Key dynamic drivers (seismicity, climate variability) are not incorporated. Assumptions of static land use, uniform soil properties, and stationary rainfall may not reflect real conditions.

- Uncertainty analysis is performed only for the integrated output, not for individual hazards.

## 1.6 Thesis Outline

This academic thesis provides a systematic process for an integrated multi-hazard risk modeling framework in the Kankai Basin using geospatial and machine learning techniques. The report follows a manuscript format with six chapters. Here's a brief overview of the content structure for each chapter.

**Chapter 1 -** introduces the general background, problem statement, aims & objectives, and scope of the research. It also presents the outline of the thesis.

**Chapter 2 -** Provides the detailed literature review of the state-of-art research in cascading hazard mapping and their assessment.

**Chapter 3** includes the description of study area and research material/data. Also, it includes descriptions of landslide, flood and soil erosion hazard conditioning factors and mapping.

**Chapter 4 -** detail explanation of an overall research methodological frameworks of the study along with the integration of multiple hazards.

**Chapter 5** - discusses on the major achievements and results of research, validations of model & comparison of results and necessary interpretations and general discussion of the findings.

**Chapter 6 -** presents conclusions and Recommendations including applicability of the study.

**Appendices** - **Appendix A** shows the Multi Hazard Events observed from field visit, **Appendix B** includes Photograph of Different Hazard taken during Field Visit, **Appendix C** details Landslide and Corresponding BSI - NDVI Time Series Analysis, **Appendix D** dipicts the certificate of conference paper, and **Appendix E** presents the plagiarism report.

# 2. LITERATURE REVIEW

## 2.1 Concept of Rainfall-Induced Cascading Hazards

In current research, the term multi-hazard refers to the integrated assessment of cascading natural hazards - landslides, floods, earthquakes, and forest fires, aimed at comprehensive risk reduction (Pourghasemi et al., 2020). In recent years, these natural disasters remain a major threat, claiming about 45,000 lives annually (representing around 0.1% of global deaths) with vast economic losses (Yigez et al., 2023). Nepal, a seismically active country with diverse geology, steep terrain, and intense monsoons, is highly vulnerable to earthquakes, landslides, and floods (Okamura et al., 2015).The vulnerability is highest in the Lesser Himalaya and Siwalik regions, underscoring the need for urgent mitigation measures (N. Paudyal et al., 2013). Furthermore, Nepal experiences recurrent seasonal hazards, with floods and landslides commonly occurring during each monsoon period. Large earthquakes occurring sporadically further intensify landslide frequency (Khatakho et al., 2021).The complex interactions among these hazards often lead to cascading and synergistic effects. Addressing and managing such complex processes requires an integrated/holistic approach that considers multiple hazards and their interrelationships (D. Gautam et al., 2021). Therefore, multi-hazard risk assessment serves as an effective tool for disaster risk reduction, identifying and mapping areas potentially exposed to combined hazard scenarios (Skilodimou et al., 2019).

Cascading hazard processes involve interconnected natural events where one hazard can trigger or amplify another (**Figure 2-1**), such as precipitation or earthquakes initiating landslides or glacial lake outburst floods (GLOFs). Key elements include terrain (DEMs), glacial lakes and their bathymetry, permafrost and glacier presence, vegetation cover, and human factors like population and infrastructure (Kirschbaum et al., 2019; S. Zhang et al., 2023). These factors can be analyzed using remote sensing, geospatial, and census data to assess slope stability, flood potential, avalanche risk, and societal exposure, providing a comprehensive understanding of how hazards propagate and interact in a cascading manner. Cascading hazards increase human risk by linking multiple events, where one hazard triggers or amplifies others, often leading to unexpected casualties, property loss, and

broader societal and environmental impacts. The **Figure 2-2** illustrates how a cascading hazard chain, starting from rainfall causing floods, debris flows, landslides, and debris dam formation - progressively transforms and amplifies impacts, ultimately threatening people. It shows the flow from hazard evaluation, decision-making, and emergency response to potential fatalities.

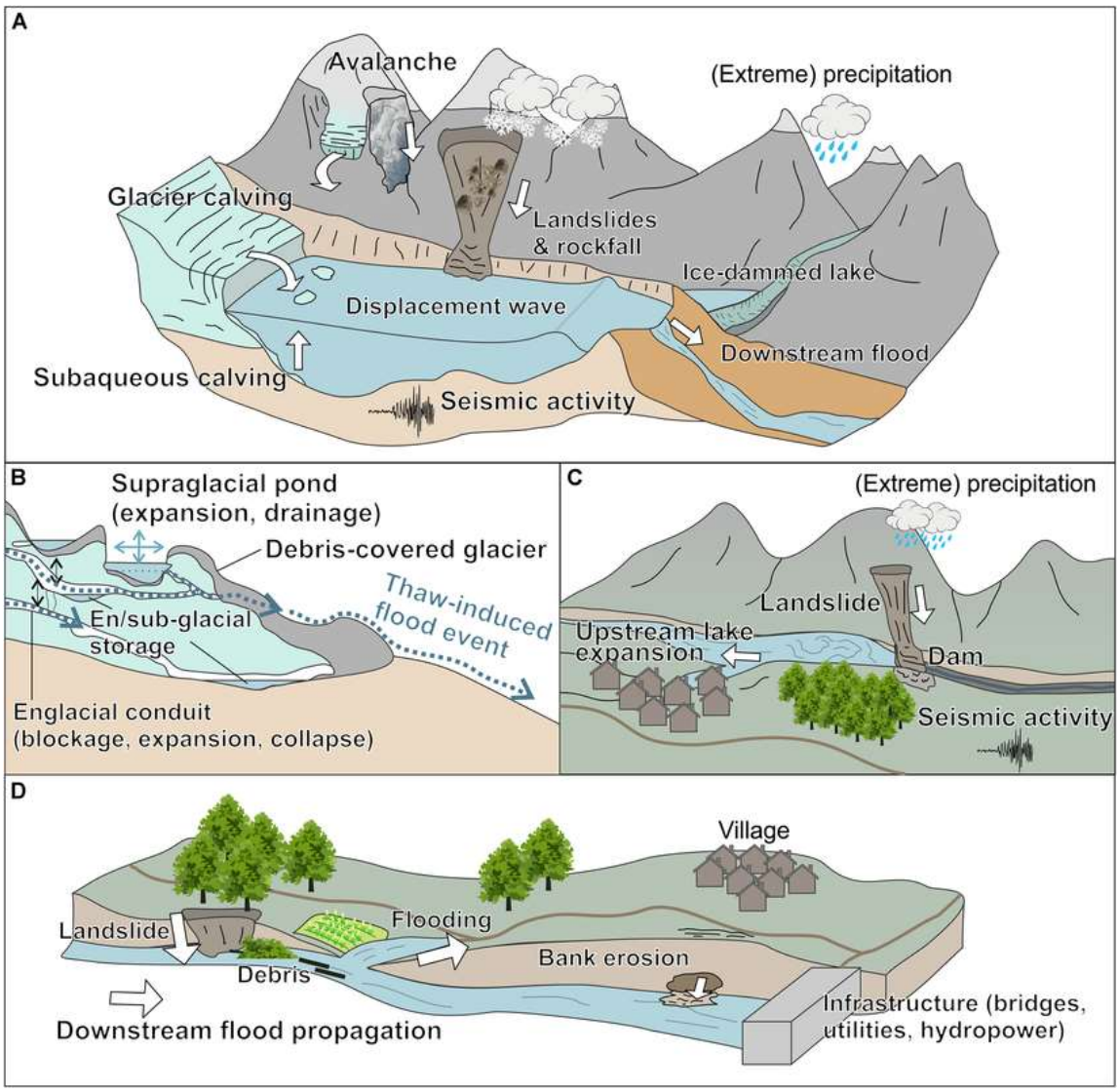


*Figure 2-1: Cascading hazard processes: (A) Proglacial lake outburst floods worsened by landslides, avalanches, or rockfalls triggered by rain or earthquakes. (B) Floods from debris-covered glaciers. (C) Landslides blocking rivers, causing upstream lake growth. (D) Failure of landslide dams, leading to downstream floods and debris impacting communities and infrastructure.*

[Source:(Kirschbaum et al., 2019)]

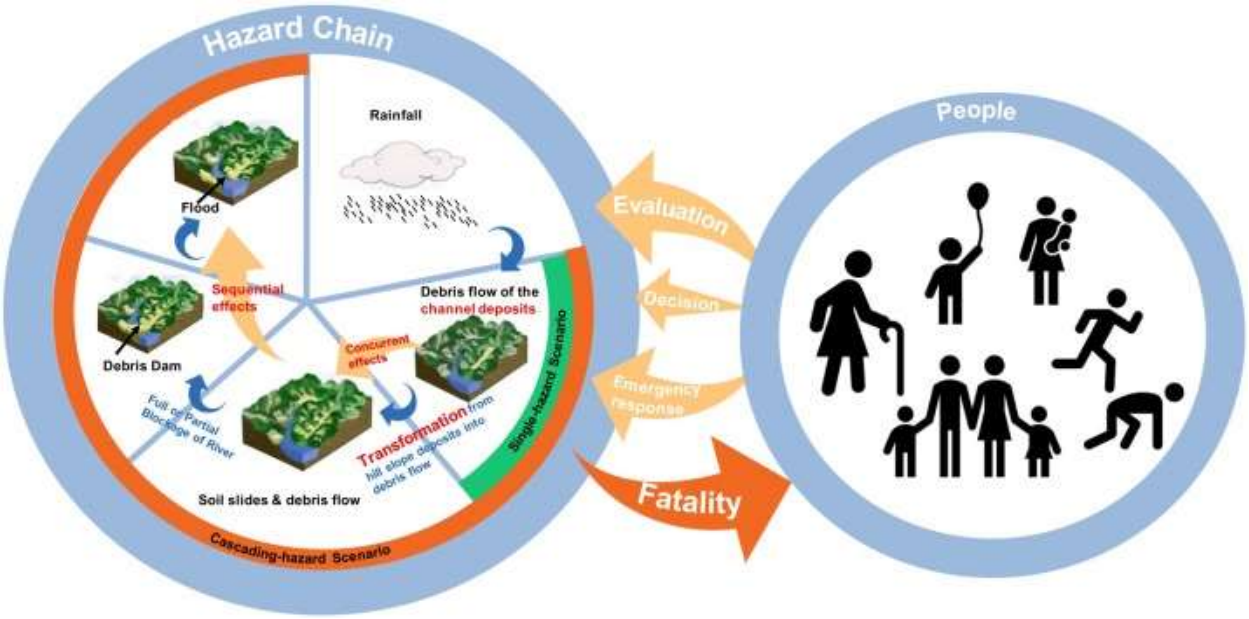


*Figure 2-2: A conceptual framework illustrating how cascading hazards amplify human risk.*

[Source: (S. Zhang et al., 2023)]

## 2.2 Landslide & its Spatial Modeling

In tectonically active mountain regions, landslides are among the most frequent and damaging hazards, involve the downward movement of soil, rock, debris, and earth under the gravity (Cruden, 1993; D. J. Varnes, 1978). Globally, landslides represent close to 10 % of natural disasters and rank among the top three in terms of mortality (Ahmed, 2015; Kanwal et al., 2016). Their occurrence, often triggered by rainfall, earthquakes, and anthropogenic activities such as mining and construction, poses substantial risks to infrastructure, ecosystems, and local economies (Carrara et al., 1995; Guzzetti et al., 2012; Reichenbach et al., 2018).

The global occurrence of landslides is increasing due to ongoing challenge of climate change, seismic activity, and human intervention in form of deforestation, agricultural activities, human settlement expansion, and poorly managed road construction (Kc et al., 2024; McAdoo et al., 2018; N. Paudyal et al., 2013; Rahman et al., 2022). Nepal, a seismically active country with diverse geology, steep terrain, and intense monsoons, is highly vulnerable to earthquakes and landslides (Okamura et al., 2015). The 2015 Gorkha earthquake starkly

highlighted this vulnerability, triggering nearly 20,000 landslides (McAdoo et al., 2018). The Nepal Disaster Report (2019) recorded approximately 3,729 landslides between 1971 – 2019 (McAdoo et al., 2018), resulting in significant loss of life, displacement, and infrastructure damage. Historically, Nepal accounts for 10% of global landslide occurrences (Froude & Petley, 2018), with an annual average of 78 fatalities recorded between 1978 – 2005 (McAdoo et al., 2018). Nearly 90% of these events occur during the monsoon season, peaking in July and August (B. R. Adhikari & Gautam, 2022). Vulnerability is highest in the Lesser Himalaya and Siwalik regions, underscoring the need for urgent mitigation measures (N. Paudyal et al., 2013).

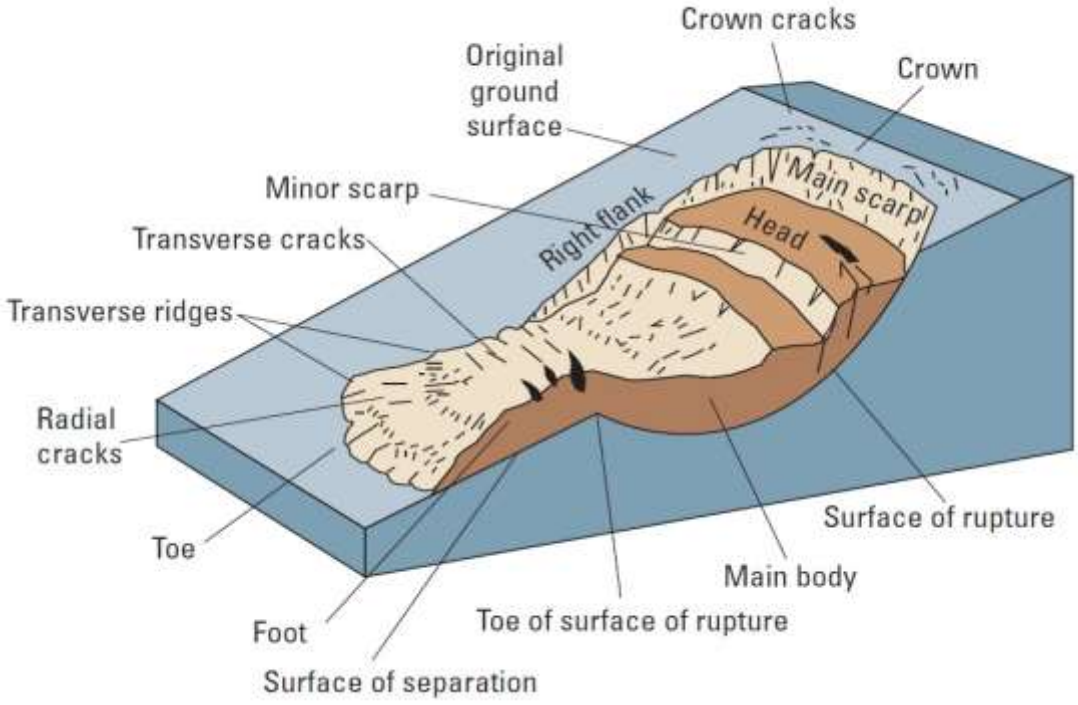


*Figure 2-3: A Schematic representation of a landslide, displaying commonly used terminology for identifying the elements of a landslide (Highland & Bobrowsky, 2008).*

A comprehensive analysis of landslide incorporates distinct components including the crown and head separated by a scarp; the main body characterized by its flanks; the foot, ending at a toe; and specific zones such as the depletion zone capturing the upper portion, and the deposition zone capturing the lower part of the landslide. (**Figure 2-3**) depicts a visual representation of a landslide, featuring commonly accepted terminology to describe

its various features. Landslides are categorized by the state of activity or movement - active, dormant or inactive (**Figure 2-4 A)** and by the kind of material - like rocks, dirt, debris, mud and movement like falling, tipping over, sliding, spreading, flowing (**Figure 2-4 B).** Further, Landslides are classified by depth/extent: shallow landslides affect surface soil and regolith, often triggered by rainfall or slope instability, while deep-seated landslides extend into bedrock and are larger, often caused by tectonics, earthquakes, or groundwater changes.

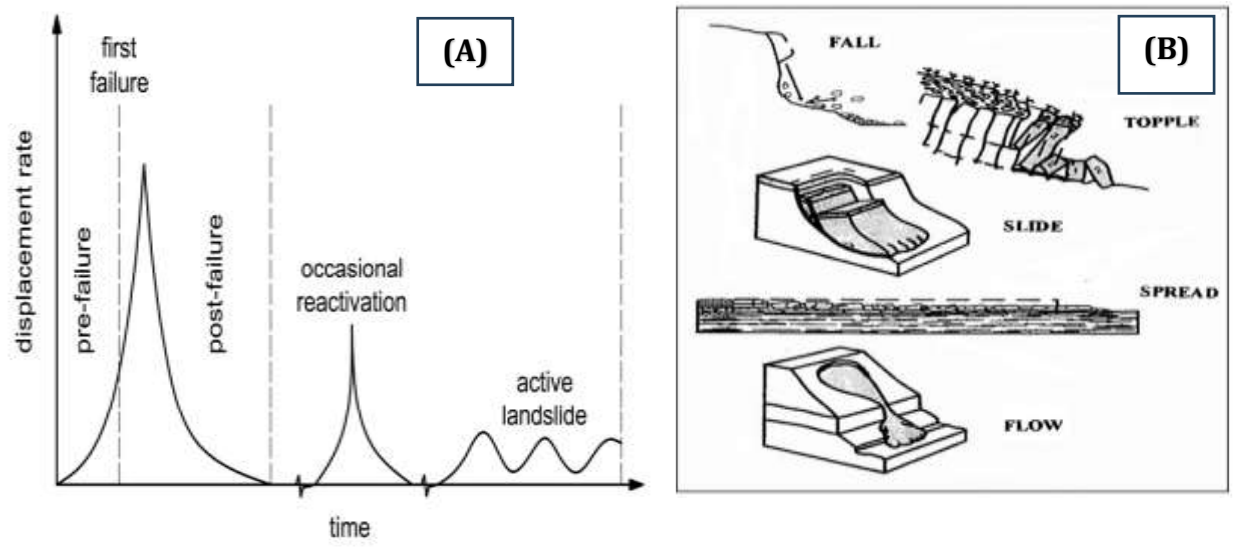


*Figure 2-4: Figure illustrating (A) Landslide process / activity stage and (B) types of movement*

[Source: (Leroueil et al., 1996), (Cruden and Varnes,1996)]

Landslides are complex events triggered when slope movements increase driving forces and reduce material strength, causing failure; a safety factor below 1 indicates instability (D. Varnes, 1978). The rainfall and earthquake are primary triggers responsible for frequent landslides throughout the world (Guzzetti et al., 2005). Globally, landslides are caused by Climatic and Hydrological factors (rainfall, river density, distance from river), geological (lithology, weathering, distance from faults etc.), Soil factors (soil types, texture, depth, drainage and hydraulic conductivity, permeability, porosity etc.), Geomorphological (altitude, relative relief, slope gradient, aspect, curvature, roughness index, TWI, SPI, STI, slope length etc.), physical and human causes (Land use/cover, road constructions etc.) (Highland & Bobrowsky, 2008). Cracks such as faults, cleavages, and similar features can

reduce the shear strength of the slope materials, impacting the overall stability of the slope. Some of the materials that form slopes are already weak due to presence of organic stuff and clays. Even hard materials like rocks can get weak due to processes like weathering and hydrology. When minerals in clays get wet, they can lose their cohesion. Rocks can also break into pieces because of freezing and thawing or temperature changes (Acharya, 2018). In overall, the landslide and slope failure process is related to shear resistance and stress of slope material.

Landslide assessment, key to geo-hazard management, identifies, categorizes, and maps landslides to support risk mitigation (D. J. Varnes, 1978). Landslide Susceptibility Mapping (LSM), the most widely used approach, predicts potential landslides based on topographical, hydrological, geological, and human factors (W. Chen et al., 2018; Le et al., 2023; Zhou et al., 2018). It helps identify vulnerable zones and guide disaster preparedness and land-use planning (Dai et al., 2002). Over the past few decades, several qualitative and quantitative methodologies have been employed worldwide for the prediction and assessment landslide susceptibility (Castellanos Abella & Van Westen, 2008; S. Lamichhane et al., 2025; Merghadi et al., 2020; Rahman et al., 2022; Singh et al., 2023; Sreelakshmi et al., 2022; Y. Wang et al., 2021). Similar efforts have been undertaken in the Nepal Himalaya region (Acharya, 2018; Adhikari & Gautam, 2022; B. K. Dahal & Dahal, 2017; R. K. Dahal et al., 2006, 2008; Hasegawa et al., 2009; Lamichhane et al., 2025; Manandhar et al., 2021; McAdoo et al., 2018; K. R. Paudyal et al., 2021; Phuyal et al., 2022; K. Pokhrel & Bhandari, 2019; Pyakurel et al., 2023; Raj Meena et al., 2021; Regmi et al., 2014; Sharma et al., 2025). However, validation is still a problem, particularly due to coexistence of multiple triggers (R. K. Dahal, 2014; R. K. Dahal et al., 2008; Hasegawa et al., 2009). Qualitative methods, such as Heuristic Analysis and Multi-Criteria Decision making, rely on expert judgments for spatial evaluation, while quantitative techniques, including weight of evidence (WoE), Frequency Ratio (FR), Fuzzy Neural Network (FNN), Logistic Regression (LR), and Fuzzy Logic (FL) statistically analyze relationships between causative factors and historical landslide events (Lin et al., 2021; Rahman et al., 2022; Sarkar & Kanungo, 2006; Shano et al., 2020; Y. Wang et al., 2021). Yet, no consensus exists regarding the optimal methodology across all environments, as predictive accuracy depends not only on data quality but also on appropriate model selection

(Acharya, 2018; Hammad Khaliq et al., 2023; Le et al., 2023; Sreelakshmi et al., 2022). Moreover, the dynamic nature of landslide triggers across temporal and spatial scales necessitates context-specific approaches (Jin et al., 2024; S. Lamichhane et al., 2025).

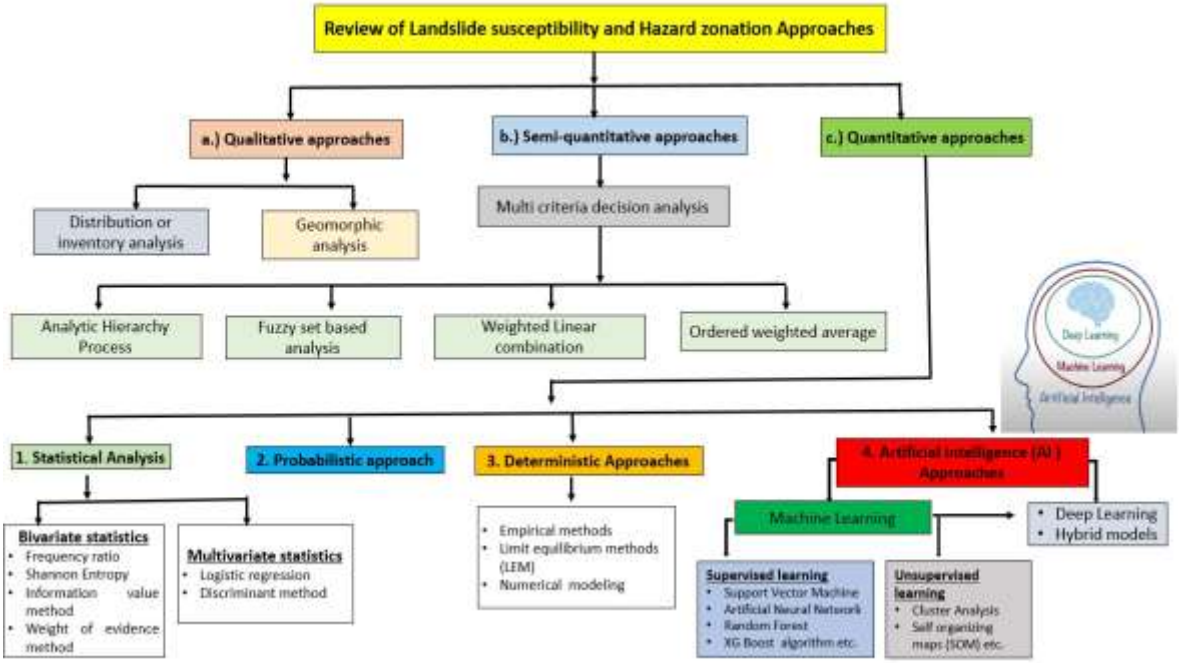


*Figure 2-5: Various approaches of landslide assessment and hazard zonation*

Efforts to reduce landslide uncertainties and minimize damages have been ongoing. With the applications of Machine Learning (ML) algorithms integrated with the geographic information systems (GIS) and remote sensing (RS), Landslide detection accuracy has significantly improved (Acharya, 2018; Sreelakshmi et al., 2022). Research conducted in recent times demonstrated the efficacy of Machine learning algorithms like Artificial Neural Network (ANN), Random Forest (RF), Support Vector Machine (SVM), Logistic Regression (LR) and Extreme Gradient Boosting (XG-Boost) for landslide prediction in Nepal's Himalayas region (Acharya, 2018; Chalise et al., 2022; T. H. K. Chen et al., 2024; Hammad Khaliq et al., 2023; S. Lamichhane et al., 2025; Pyakurel et al., 2023; S. Shrestha et al., 2023). (**Figure 2-5**) shows review of various methods of landslide hazard assessment. These approaches are based on the premise that locations with similar characteristics to past landslide sites are more likely to experience future landslides.

## 2.3 Flood & its Spatial Modeling

Floods are one of the most common and damaging natural hazards, resulting from excessive rainfall, river overflow, snowmelt, dam failure, or inadequate drainage systems. They result in considerable losses to human life, infrastructure, agricultural areas, and the environment (Kaya & Derin, 2023). Understanding the spatial distribution and dynamics of flooding is therefore essential for sustainable land-use planning and disaster management.

Nepal, particularly valley & Terai region susceptible to flooding due to its flat topography, heavy rainfall, and increasing human activities (Aryal et al., 2023). Its vulnerability ranks 30th in terms of floods (Guragain & Doneys, 2022; Khatakho et al., 2021). The occurrence and severity of floods are influenced by several physical and environmental factors, including rainfall intensity, topography, soil characteristics, land use cover, drainage density, and river morphology. Urban expansion, growth of impervious surfaces, and floodplain encroachment have disrupted natural hydrology, increasing surface runoff, reducing groundwater recharge, and raising flood risk. Several major flood events, including those in 1954, 1981, 1993, 2002, and 2008, have caused substantial damage to agriculture, human settlements, and infrastructure in Nepal (K. Lamichhane et al., 2025). Recent extreme rainfall events, such as the September 2024 rainfall in central Nepal, further highlight the increasing flood risk. These events caused widespread landslides, infrastructure damage, and economic losses, demonstrating the urgent need for comprehensive flood analysis, improved urban planning, and effective disaster risk management strategies.

Spatial flood modeling involves using geospatial methods and analytical tools to simulate and map flood extent, depth, and likelihood across a landscape. These models integrate hydrological, hydraulic, and GIS approaches to analyze the interaction between rainfall, surface runoff, river flow, and terrain characteristics. Hydrological models estimate flood volumes by simulating rainfall–runoff processes, whereas hydraulic models such as HEC-RAS and MIKE FLOOD simulate water flow and floodplain behavior (Nunes Correia et al., 1998). Various approaches have been used in previous studies, with the most common being multi-criteria decision-making (MCDM), physically based hydrological models, statistical

techniques, and soft computing methods (Kaya & Derin, 2023). These methods vary in data needs, reliance on expert input, computational demand, and implementation complexity.

**Physically based hydrological models** simulate the physical processes of water movement within a watershed, including runoff generation, flow routing, and floodplain inundation (Vieux et al., 2004). Although highly effective for detailed flood simulation, these models require extensive field data, high computational resources, and considerable cost, limiting their applicability for large-scale analyses. **Multi-criteria decision-making (MCDM) methods** are widely used in flood susceptibility assessment due to their simplicity and ability to integrate multiple factors simultaneously (Samanta et al., 2016). Techniques such as the AHP, Analytic Network Process, Decision-Making Trial and Evaluation Laboratory (DEMATEL), and Weighted Linear Combination allow researchers to assign weights to flood conditioning factors and evaluate flood-prone areas. However, these methods often rely heavily on expert judgment, which may introduce subjectivity into the results.

**Statistical methods** are commonly used to analyze the relationship between flood occurrences and flood-conditioning factors using mathematical models. These methods include bivariate and multivariate statistical analysis (Shafapour Tehrany et al., 2019). Techniques such as the Frequency Ratio (FR) and Logistic Regression (LR) are frequently applied to evaluate the influence of individual factors on flood occurrence. While statistical methods have demonstrated good predictive performance, they typically assume linear relationships, which may not adequately represent the nonlinear behavior of flood processes.

In recent years, soft computing methods like **data-driven and machine learning approaches** have gained popularity in flood susceptibility modeling due to their ability to handle uncertainty and nonlinear relationships. These approaches include artificial neural networks (ANN), support vector machines (SVM), decision trees (DT), random forest (RF), fuzzy logic, and genetic algorithms. In addition, metaheuristic optimization techniques such as particle swarm optimization (PSO), grey wolf optimization (GWO), and bat algorithms are commonly applied to improve model performance (Aldiansyah & Wardani, 2023; Youssef et

al., 2022). Recent studies increasingly use hybrid models that combine statistical, machine learning, and optimization methods to enhance prediction accuracy. These integrated approaches are effective in handling the complexity and uncertainty of flood susceptibility mapping.

### 2.4 Soil Erosion & its Spatial Modeling

Soil erosion is the removal and movement of the topsoil from one place to another, mainly driven by water, wind, or ice. In water-induced erosion (**Figure 2-6**), the initial stage is raindrop splash, where falling raindrops detach and displace soil particles during erosive rainfall (X. Zhu et al., 2023). The raindrop impact loosens soil particles, which are then carried away by surface runoff, forming rills, gullies, or sheet erosion. Wind erosion takes place in dry, unvegetated soils when strong winds detach and carry fine particles over long distances (S. K. Ghimire et al., 2013). Soil erosion rates are controlled by factors including rainfall intensity, infiltration capacity, runoff volume, soil texture, vegetation cover, and slope length (Borrelli et al., 2021; Fernández et al., 2023).

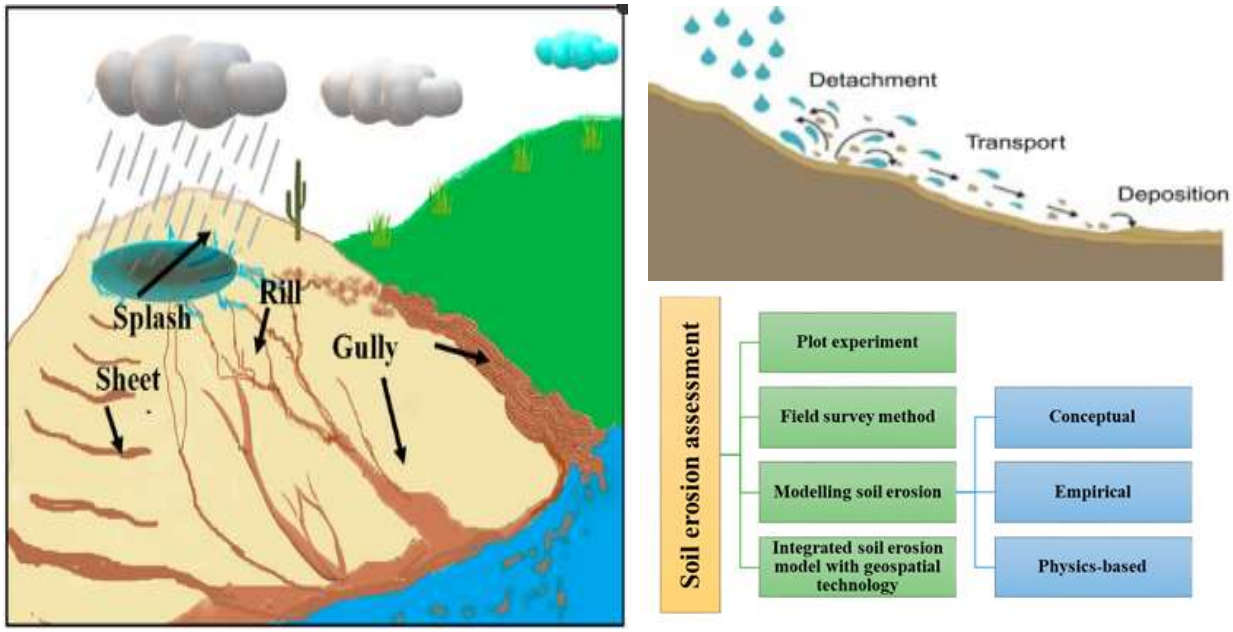


*Figure 2-6: Soil erosion process/types by water and Assessment methods*

[source:(Senanayake et al., 2020)]

In addition, anthropogenic activities, such as deforestation, overgrazing, and construction, can significantly increase erosion risk. Weak soil structure, high clay or silt content, and sparse vegetation further exacerbate soil susceptibility to detachment. Understanding the processes and controlling factors of soil erosion is essential for selecting effective monitoring methods and putting into practice of sustainable land management strategies.

Soil erosion is recognized as a major global environmental and agricultural concern, leading to land degradation, declining agricultural productivity, and ecosystem disruption (Senanayake et al., 2020). The erosion threatens ecosystems and agricultural sustainability globally. In South Asia, land degradation driven by erosion costs the region an estimated US$10 billion annually, equivalent to 2% of its GDP and 7% of agricultural productivity (Mandal & Kumari, 2020). Nepal, situated in the central Himalayas, is a mountainous country characterized by tectonically active geology. The Siwalik (Churia) and Lesser Himalaya regions are particularly prone to severe erosion. Dynamic geological processes—including the ongoing subduction of the Indian Plate beneath the Eurasian Plate, uplifting at ~2 cm/year (Okamura et al., 2015), steep slopes, and loose sedimentary formations such as sandstone, shale, and conglomerates—combined with monsoon-driven rainfall intensified by climate change, make these regions among the most erosion-prone landscapes on Earth (Bastola et al., 2019; McAdoo et al., 2018). (Koirala et al., 2019; B. Raya, 2023b; Siwakoti, 2000) reports Nepal's severe soil erosion, averaging 25 tons/ha/year, totaling 369 metric tons annually with the middle mountains experience the highest erosion (38.4 tons/ha/year), driven by heavy rainfall, runoff, land degradation, and poor conservation practices. The erosion rates of Siwalik Zone far exceed global averages (10 - 15 Mg/ha/yr), driven by monsoons, weak sedimentary geology, and unsustainable land use (R. Dahal, 2020; S. K. Ghimire et al., 2013).

Soil erosion hazard assessment involves evaluating the susceptibility of land to erosion and predicting potential soil loss. Throughout the years, various approaches have been developed, broadly categorized into qualitative, empirical, physics-based, conceptual, and hybrid or GIS-integrated methods (Karydas et al., 2014; Senanayake et al., 2020). **Qualitative and semi-quantitative approaches** rely on expert judgment, observational

data, and scoring or ranking systems to assess erosion risk. Methods such as the Weight of Overlay approach, AHP, and factor-based ranking are commonly used to combine multiple controlling factors, including slope, land use, soil type, and rainfall.

**Empirical models** like RUSLE, USLE, and process-based tools (WEPP, EUROSEM) dominate erosion prediction, yet face limitations in cross-scale adaptability, high-resolution parameterization, and validation (Borrelli et al., 2021; Epple et al., 2022). RUSLE remains widely applied (17.1% of studies), leveraging factors such as rainfall erosivity (*R*), soil erodibility (*K*), slope (LS), cover (*C*), and conservation practices (*P*) (Fernández et al., 2023). However, global syntheses reveal critical gaps: underrepresentation of wind/tillage erosion, regional disparities (e.g., Central Asia, Africa), and inconsistent validation (Borrelli et al., 2021). Also, the Global Applications of Soil Erosion Modelling Tracker (GASEMT) found only 58% of studies doing any validation, with most not being calibrated to data of the region studied, limiting their practical usefulness.

**Physics-based models** simulate the soil erosion underlying physical processes, including runoff, infiltration, sediment transport, water balance, and vegetation dynamics. Models such as the Water Erosion Prediction Project (WEPP) predict soil loss at multiple spatial and temporal scales but require large amounts of data and processing power. **Conceptual models** integrate features of empirical and physics-based approaches, providing a framework to simulate erosion and sediment transport in watersheds with limited process detail. Examples include Agricultural Non-Point Source Pollution Model (AGNPS) and Soil and Water Assessment Tool (SWAT). **Hybrid and GIS-based approaches** have emerged in recent decades, combining models with geospatial techniques such as GIS, remote sensing, and GPS (Fernández et al., 2023).These approaches allow spatially explicit mapping of erosion-prone areas and scenario-based simulations, integrating advanced tools such as artificial neural networks (ANN), geographically weighted regression (GWR), and multi-criteria decision-making methods for improved prediction and hazard assessment.

## 2.5 Interactions Between Landslides, Floods, and Soil Erosion

Landslides, floods, and soil erosion are closely interconnected hazards, often influencing each other in cascading or simultaneous events. Understanding these interactions is essential for multi-hazard assessments, where the combined effects of these processes are considered rather than evaluating each hazard separately. Such integrated approaches provide better guidance for disaster risk management, land-use planning, and environmental conservation, particularly in vulnerable regions like the Nepal Himalayas.

Traditional hazard assessments often focus on a single hazard, ignoring the interactions and cascading effects among multiple hazards (Simone, 2011). However, recent research emphasizes the importance of integrated multi-hazard approaches, which consider the co-occurrence and sequential nature of events, enabling a more comprehensive understanding of risk (Khatakho et al., 2021; Skilodimou et al., 2019). Over the past decade, several qualitative and quantitative frameworks have been employed globally to predict and assess multi-hazard scenarios (Chauhan et al., 2025; Gentile et al., 2022; Lombardo et al., 2020; N. M. Raya et al., 2024; Rusk et al., 2022; J. Wang et al., 2021; Zou et al., 2022).

Similar efforts have been undertaken in the Nepal Himalaya region (Aksha, Resler, Juran, Jr, et al., 2020; Bhatta & Adhikari, 2024; D. Gautam et al., 2021; M. Ghimire, 2023; Jimee et al., 2019; Khatakho et al., 2021; Rai et al., 2025; Tandan et al., 2025; Thompson et al., 2024). However, validation is still a problem, particularly due to coexistence of multiple triggers (Khatakho et al., 2021; Rai et al., 2025). Moreover, the dynamic nature of triggers across temporal and spatial scales necessitates context-specific approaches (Jin et al., 2024; S. Lamichhane et al., 2025). Several methodological frameworks have been developed to assess multi-hazard risks. One common approach involves the integration of Geographic Information Systems (GIS) and remote sensing techniques to map individual hazard susceptibilities and overlay them to produce a combined hazard map. Statistical and machine learning methods such as Random Forest, Support Vector Machine, and Boosted Regression Tree, are increasingly applied to model hazard susceptibility and analyze relationships between hazards and their predictors (Javidan et al., 2024). Another approach focuses on probabilistic and scenario-based modeling, which evaluates the likelihood of hazard

occurrence and their potential cascading effects (Batikh et al., 2026). In mountainous regions such as the Himalaya, landslides can block rivers and trigger flooding, while floods can accelerate riverbank erosion and slope instability. Understanding these interactions is essential for accurate risk assessment. Multi-hazard mapping provides decision-makers with a robust tool for prioritizing interventions, allocating resources, and planning mitigation strategies.

### 2.6 GIS, Remote Sensing, & Machine Learning in Multi-Hazard Assessment

The combination of the worldwide web, satellite images, public earth observation (EO), and rapid growth of artificial intelligence (AI) has significantly has profoundly improved studies on natural hazards by enabling more precise prediction (Sreelakshmi et al., 2022). Further, Machine Learning (ML) algorithms integrated with the geographic information systems (GIS) and remote sensing (RS) significantly improved the success rates of hazard prediction (Herrera, 2016). ML techniques offer most advanced solution by enabling the analysis of complex, and heterogeneous datasets. Research conducted in recent times demonstrated the efficacy of Machine learning algorithms like Artificial Neural Network (ANN), Random Forest (RF), Support Vector Machine (SVM), Logistic Regression (LR) and Extreme Gradient Boosting (XG-Boost) for global multi-hazard risk modeling (Chauhan et al., 2025; Ferrario et al., 2025; Nachappa et al., 2020; Pourghasemi et al., 2020; T. Zhang et al., 2023). Collectively, these studies demonstrated integration of ML with GIS and RS provides a robust framework for multi-hazard risk assessment.

### 2.7 Review of Existing Literatures Relevance to Nepal and Kankai Basin

Nepal's predominantly hilly and mountainous terrain, comprising approximately 80 % of the country, renders it highly susceptible to multi-hazard risks (MHR), including earthquakes, forest fires, landslides, floods, and soil erosion (B. Raya, 2023a; Vaidya et al., 2022). Hazard interactions, such as rainfall or earthquake induced landslides, and floods exacerbated by deforestation and land-use change, often amplify the exposure and vulnerability of communities. Historical records indicate that the Eastern Nepal has experienced frequent

landslides, floods, glacier lake outburst floods (GLOFs), and droughts, which have resulted in infrastructure damages and disruption of livelihoods (A. B. Shrestha et al., 2010; J. Zhang et al., 2016). Landslide analysis revealed 6,877 events over 23 years, predominantly shallow, rainfall-induced failures concentrated in the Lesser Himalaya, driven by steep slopes and fragile geology (J. Zhang et al., 2016). GLOF simulations in the Sun Koshi indicate peak flows of ~7,900 $m^3/s$, threatening ~950 ha of land and infrastructure with potential economic losses of ~$197 million (A. B. Shrestha et al., 2010). Climate change has increased the intensity and frequency of hydro-meteorological hazards, necessitating adaptive agricultural practices, improved flood management, and integrated watershed planning (Hussain et al., 2018; S. Lamichhane et al., 2021). Trans-boundary governance across China, Nepal, and India adds complexity to disaster risk management in Koshi, as upstream interventions can significantly affect downstream populations (Wahid et al., 2016). Over the past decade, an increasing number of studies have focused on understanding these hazards individually and in combination, as well as developing risk assessment methodologies to inform disaster preparedness and climate adaptation planning.

Early studies in urban and regional contexts laid the groundwork for multi-hazard assessment in Nepal. (Rimal et al., 2015) assessed the impacts of rapid urbanization and LULC transitions in Pokhara Valley between 1990 and 2013. Using remote sensing and GIS, particularly Landsat imagery, the study quantified significant built-up area expansion (from 24.03 $km^2$ to 54.20 $km^2$), which contributed to increased exposure to multiple hazards, including floods, landslides, fires, sinkholes, and earthquakes. This work provided one of the first comprehensive multi-hazard risk maps for the valley, highlighting the link between urban growth and hazard vulnerability.

Infrastructure-focused assessments have also emphasized multi-hazard impacts. (R. Adhikari et al., 2019) examined highway bridges along the East-West Highway, integrating post-disaster field surveys and literature review to evaluate flood and earthquake vulnerability. The study combined an extensive literature review with post-disaster field assessments of 50 bridges affected by the 2017 flood events to evaluate structural damage and serviceability. Based on empirical observations, the authors developed a systematic

guideline for post-flood and post-earthquake damage assessment and vulnerability grading of highway bridges. The findings indicate that repeated exposure to natural hazards significantly accelerates structural deterioration, reducing long-term performance and resilience. By integrating multi-hazard risk perspectives into infrastructure evaluation, the study provides a practical and actionable framework for resilient bridge design, maintenance planning, and sustainable infrastructure management in hazard-prone regions like Nepal. Similarly, (Aksha, Resler, Juran, & Carstensen, 2020) conducted a comprehensive geospatial assessment of MHR in Dharan by integrating physical hazard analysis with social vulnerability evaluation. The study employed statistical techniques and the AHP to generate hazard maps for floods, earthquakes, and landslides, while the Social Vulnerability was used to assess population susceptibility. Their composite multi-hazard risk maps highlighted high-risk zones along river corridors and low-risk hill areas, providing a practical approach for data-scarce urban settings.

At broader scales, (D. Gautam et al., 2021) conducted local-level multi-hazard zonation in Nepal using historical hazard records of over 27,482 events across 16 natural hazard types. Weighted scoring and normalization techniques allowed the identification of high-risk regions in southeastern and south-central Nepal. As one of the first fine-scale local multi-hazard zonation efforts in Nepal, the study provides an important decision-support tool for provincial and federal planning, enabling prioritized disaster risk reduction and response strategies. Concurrently, (S. Lamichhane et al., 2021), (Khatakho et al., 2021) and (A. Shrestha et al., 2023) investigated cascading hazards and integrated multi-hazard risk in transboundary, urban and rural contexts, respectively. By combining geophysical, hydro meteorological, and socio-economic data within multidisciplinary and GIS-based frameworks, the studies revealed how interactions among hazards amplify overall risk and vulnerability. Their findings underscore the importance of integrating cascading and compounding effects into comprehensive disaster risk assessment and land-use planning frameworks.

High-resolution susceptibility mapping and machine learning approaches have recently enhanced multi-hazard research. (Rusk et al., 2022) applied Maximum Entropy (Maxent)

machine learning approach across the Hindu Kush Himalaya (HKH), integrating floods, landslides, and wildfire susceptibility with population exposure to identify multi-hazard hotspots in foothill regions. The findings revealed almost half of the HKH population lives in areas with high exposure to multiple hazards, with warm, low-altitude foothill regions emerging as significant multi-hazard hotspots. The study further underscores the rapid urban expansion and migration trends are increasingly concentrated in these vulnerable areas, potentially intensifying future risk. (M. Ghimire, 2023) evaluated multi-disaster risk in the Birgunj - Simara Urban Corridor using geospatial analysis of floods, earthquakes, windstorms, and fires combined with stakeholder consultations. The study found that flood risk is intensified by rapid land-use change, floodplain encroachment, and inadequate drainage infrastructure, while socioeconomic factors such as poverty and limited disaster preparedness further increase vulnerability. The study highlights the need to integrate risk-sensitive land-use planning, resilient infrastructure, and community-based early warning systems to promote disaster-resilient urban development.

Similarly, (Bhatta & Adhikari, 2024) and (Tandan et al., 2025) employed GIS, remote sensing, and AHP-based multi-criteria analysis to generate ward-level multi-hazard risk maps in the Rapti Valley and Gulmidarbar Rural Municipality, respectively. By integrating multiple hazards with physical, social, and economic vulnerability indicators, the studies generated detailed ward-level multi-hazard risk maps that identify spatial variations in risk and highlight the most vulnerable areas. Their findings demonstrate the effectiveness of combining hazard and vulnerability layers within a geospatial framework to support land-use planning, evidence-based disaster risk reduction, and policy formulation. These studies emphasize the growing importance of localized multi-hazard assessment approaches in improving preparedness and resilience in hazard-prone regions.

(Rai et al., 2025) conducted a GIS-based multi-hazard risk assessment for Waling Municipality by integrating flood, landslide, forest fire, earthquake, and debris flow susceptibility with ward-level vulnerability using the Analytic Hierarchy Process (AHP). (Pathak et al., 2026) developed an integrated GIS-based multi-hazard assessment framework for the Marin Watershed by combining MaxEnt modeling, RUSLE, flood analysis,

and multi-temporal land-use data. The study identified 27.3% of the watershed as highly susceptible to landslides, 24.4% to forest fires, 18.3% to flooding, and 32.9% to severe soil erosion, demonstrating the effectiveness of integrated modeling and multi-criteria analysis for prioritizing hazard mitigation and supporting climate-resilient watershed management. Community-centered and data-scarce frameworks have also been developed. (Thompson et al., 2024) produced a Kathmandu Valley database of multi-hazards interrelationships, combining literature, media, and stakeholder knowledge to capture 83 hazard interactions. (Niraula et al., 2026) further examined community resilience in the Narayani Basin by using a mixed-methods approach including in-depth interviews and focus group discussions and integrating the Community Capitals Framework (CCF) with the Disaster Resilience of Place (DROP), revealed how deficits in social, economic, infrastructural, institutional, and environmental dimensions amplify cascading vulnerabilities, emphasizing the need for people-centered, multi-hazard resilience planning.

Research specific to the Kankai River Basin has evolved from hazard-focused mapping to integrated hydrological and climate-impact assessments. (Karki, 2011) conducted one of the earliest GIS-based flood hazard studies, producing 25 and 50 - year return period flood maps and highlighted increasing vulnerability of agricultural land and settlements due to climate variability. (D. K. Gautam & Dulal, 2013) determined threshold runoff values for operational flood hazard early warning systems in major Nepalese rivers including Kankai, using HEC-RAS and DEM-based inundation modeling, while (Kayastha, 2012) applied fuzzy logic for LSM in the Garuwa sub-basin. By integrating eight causative factors and testing fuzzy operators, the study demonstrated that the fuzzy gamma operator ($\gamma = 0.70$) yielded the highest prediction accuracy, contributing to methodological advancement in probabilistic landslide mapping. Hydrological modeling studies later enhanced basin-scale understanding. (Silwal et al., 2020) and (Karna et al., 2021) focused on climate-driven hydrological changes and HEC-HMS runoff modeling, whereas (Aryal et al., 2023) analyzed spatio-temporal streamflow variability across major rivers, including Kankai. More recently, flood risk modeling has become more detailed and localized. (Pudasaini et al., 2022) developed 1D HEC-RAS floodplain models for Kankai Municipalities, highlighting localized flood risk. Climate - hydropower nexus research has also emerged. (Poudel et al., 2025)

projected climate-driven changes in streamflow and hydropower generation using CMIP6-SWAT models, revealing both potential increases in water availability and inter-annual variability challenges. Collectively, these studies highlight a clear trajectory in Nepalese multi-hazard research: from hazard identification and flood/landslide mapping, toward integrated, climate-informed, and community-centered frameworks. However, most studies still consider hazards individually or focus on two-way interactions (e.g., rainfall–landslide or earthquake–landslide). Comprehensive models that integrate rainfall-induced cascading hazards, including landslides, floods, and soil erosion, remain limited.

### 2.8 Research Gaps

Despite considerable advancements in hazard assessment and multi-hazard risk analysis in Nepal, several critical research gaps remain, particularly in the context of rainfall-induced cascading hazards in the Kankai Basin. Most previous studies have predominantly focused on single-hazard assessments, such as landslides (Kayastha et al., 2012; Rusk et al., 2022), floods (Karki, 2011; Pudasaini et al., 2022) or soil erosion (Silwal et al., 2020), with limited attention to their interactions and cascading effects within a watershed system. Consequently, understanding of how slope instability, sediment mobilization, and downstream flooding interact under extreme rainfall events remains incomplete.

Another significant gap lies in the integration of modeling approaches. While machine learning techniques, such as SVM, have been effectively applied for landslide and flood prediction (Rai et al., 2025), and empirical models like RUSLE has been widely applied for estimating soil loss (Silwal et al., 2020), few studies have combined these methods into a unified, multi-hazard framework. Similarly, qualitative soil erosion mapping via weighted overlay techniques has seldom been integrated with quantitative RUSLE outputs to provide a comprehensive view of hazard-prone areas. Data limitations also constrain hazard modeling in the region. Many studies operate under data-scarce conditions, particularly at the watershed scale, limiting the resolution and accuracy of hazard and vulnerability maps (Aksha, Resler, Juran, & Carstensen, 2020; Thompson et al., 2024). Moreover, the majority of research emphasizes hazard exposure and susceptibility, often overlooking community-

focused vulnerability and resilience dimensions, which are critical for translating hazard assessments into actionable disaster risk reduction and adaptation strategies (Niraula et al., 2026). Furthermore, while multi-hazard and cascading hazard frameworks have been applied in some regions of Nepal (Khatakho et al., 2021; S. Lamichhane et al., 2021), they remain limited in spatial scope, temporal resolution, and methodological integration. Specifically, in the Kankai Basin, there is a lack of comprehensive studies linking rainfall-induced landslides, soil erosion, and flood susceptibility, despite the high exposure of communities and infrastructure to these hazards.

Addressing these gaps is crucial for developing a holistic, comprehensive cascading hazard assessment framework for the Kankai Basin, enabling hotspot identification, climate-resilient watershed management, and effective disaster risk reduction planning. This study aims to fill these gaps by combining SVM-based flood and landslide susceptibility prediction, weighted overlay and RUSLE-based soil erosion modeling, and integrated multi-hazard mapping within a watershed-scale GIS framework.

# 3 STUDY AREA AND DATA

## 3.1 Study Area

### *3.1.1 Location, Topography & Climate*

The Kankai River watershed, as shown in (**Figure 3-1)**, is situated in the Koshi province of Nepal. Geographically, the basin extends between 26°41'N – 27°07'N Latitude and 87°44'E – 88°09'E Longitude. Kankai River, the basin's principal river, originates along the Ilam - Panchthar district border. The River is primarily fed by its main tributaries, the Mai Khola and Puwa Khola. It originates from the confluence of the Mai Khola and Deb Mai Khola rivers, draining an area of about 1,284 km$^2$ with elevations ranging from 62 m to 3,598 m above mean sea level (Dhakal, 2020; Pudasaini et al., 2022). The river enters India from the south and eventually merges with the Mahananda River in Bihar.

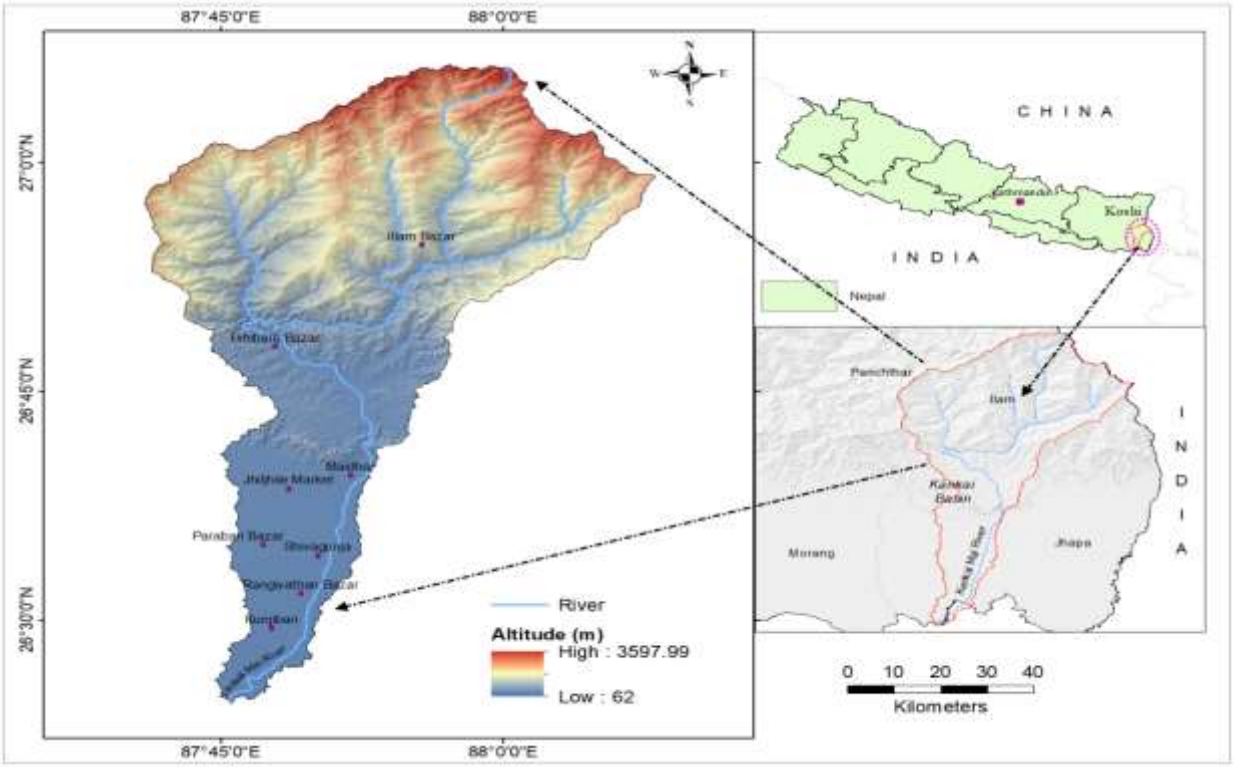


*Figure 3-1: Location of Study Area showing Topographical Features*

The basin exhibits highly varied topography, characterized by deeply incised V-shaped valleys, narrow ridgelines, and convex–concave slope profiles. The valley morphology is

generally wider in the headwater regions and progressively narrows downstream. The upper portion lies in a hilly region characterized by steep terrain, while the lower portion extends into flat plains with gentle slopes. Although Nepal generally experiences a monsoon - dominated climate, Kankai watershed demonstrates two distinct climatic zones due to its significant altitudinal variation (Pudasaini et al., 2022). The upper basin, located in the hills, experiences subtropical to temperate climatic conditions, whereas the lower basin, situated in the plains, has a tropical climate. Snowfall does not occur within the watershed. In the upper hilly region, the average winter temperature is around 12°C, increasing to approximately 27°C during summer. In contrast, the lower plains experience winter temperatures ranging from 7°C to 23°C, while summer temperatures range from 24°C to 35°C, occasionally exceeding 37°C (Silwal et al., 2020). The Basin has ~75% RH (75–85% class), vapour pressure around 20–23.79, and sunshine duration ~80% for most months dropping below 50% during monsoon (Karki, 2011; Silwal et al., 2023).

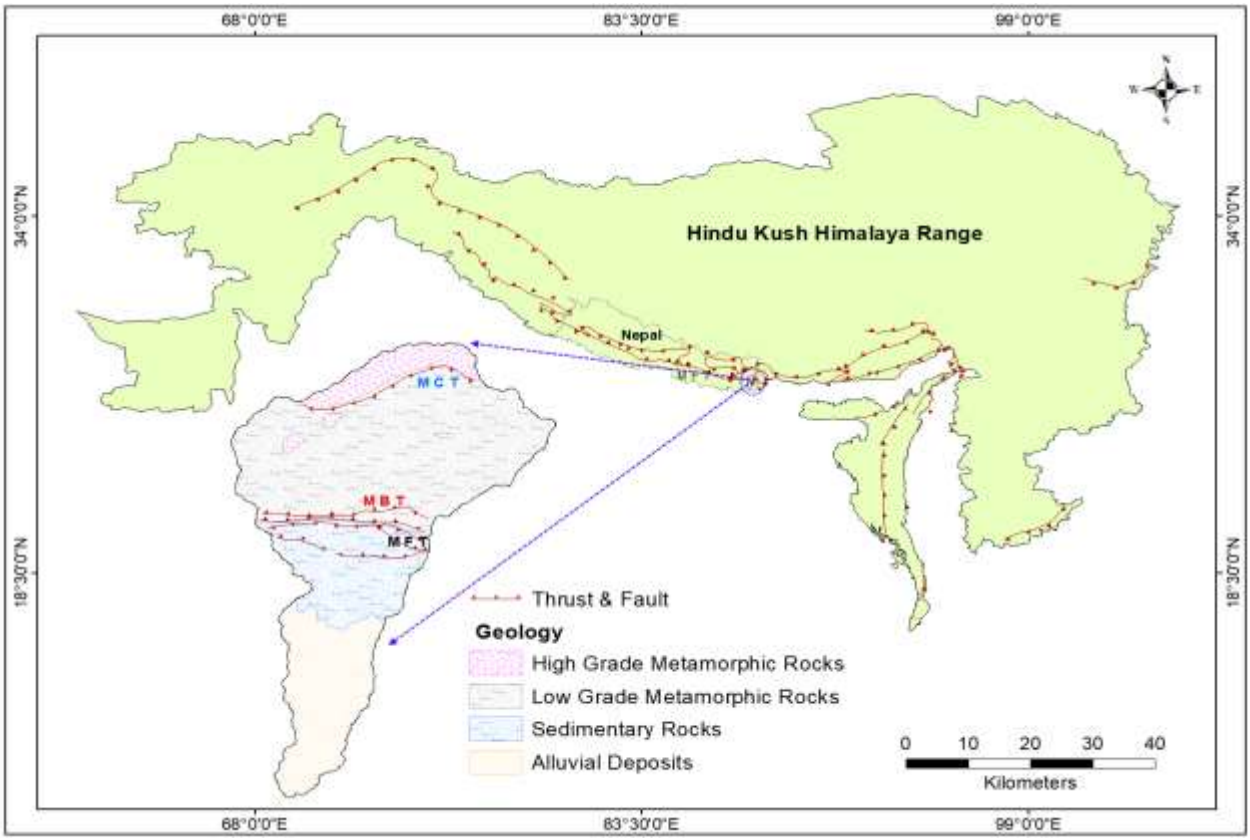


*Figure 3-2: Geological setting and major Seismotectonic feature of the of Study Area*

*3.1.2 Geological Setting & Seismology*

The Kankai Basin is located within the tectonically active Hindu Kush Himalaya of eastern Nepal (**Figure 3-2**) and characterized by a braided channel pattern, frequently inundates extensive downstream floodplain areas during high flood events (Nath & Hudait, 2024; Pudasaini et al., 2022). The basin extends across major Himalayan lithotectonic zones, comprising high-grade metamorphic rocks in the northern upstream region, low-grade metamorphic rocks in the central part, and sedimentary formations with extensive alluvial deposits in the southern downstream plains. The higher elevations are dominated by gneiss, schist, and migmatites, while the middle sections consist mainly of phyllite, slate, quartzite, and schist (Kayastha, 2012). Toward the Terai region, unconsolidated alluvial sediments such as sand, silt, clay, and gravel prevail. This lithological and topographic variation contributes to high erosion rates, sediment transport, and geomorphic instability within the basin (Aryal et al., 2023; Ulak, 1970).

The seismo tectonic framework of the Kankai Basin is controlled by the ongoing convergence (~20 mm/yr) between the Indian Plate and the Eurasian Plate, which drives the uplift and deformation of the Himalaya (Ader et al., 2012). The basin is influenced by major east - west trending thrust systems, including the MBT and MFT. These tectonic structures accommodate crustal shortening and are associated with frequent seismic activity, making the region highly earthquake-prone. The interaction between active tectonics, fragile geological formations, steep terrain, and intense monsoonal rainfall enhances slope instability, sediment production, and downstream flooding, thereby increasing the overall hazard vulnerability of the basin.

## 3.2 Data Collection and Sources

The data consists of combined quantitative and qualitative type with both primary and secondary sources**.**

**1. Primary Data:** Primary data consist of ground-truth information on natural hazard hotspots (landslides and floods), collected through field studies (GPS surveys, transect walks, direct observations, and photographic evidence) and Google Earth digitization.

**2. Secondary Data:** Secondary data were obtained from multiple reliable sources, including government agencies and international databases. These datasets include Digital Elevation Model (DEM), climatic records, rainfall, satellite imagery, geological and soil maps, infrastructure data, and hazard inventory data, which are used for spatial analysis and multi-hazard assessment. **Table 3-1** below gives the details of each data types.

*Table 3-1: An overview of the secondary datasets and their sources*

| S.N | Data | Source | Format | Use |
|---|---|---|---|---|
| 1 | DEM | ASTER Dem | Raster, 30 m | Geo-morphological & Topographic features |
| 2 | Rainfall (25 years) | Department of Hydrology & Meteorology (DHM) | Time-series | Precipitation & rainfall erosivity Analysis |
| 3 | Geology | Department of Mines & Geology (DMG), 1994 | Vector | Lithological classification |
| 4 | Soil Types | SoTer Nepal, FAO (2004) | Vector | Soil classification & Soil erodibility characterization |
| 5 | Landsat – 8 / 9 images | USGS / NASA / GEE | Raster | NDVI Analysis |
| 6 | Sentinel - 1 SAR & sentinel- 2 images | Copernicus / ESA | Raster | Flood Inventory, Soil moisture and LULC mapping |
| 7 | Infrastructure Maps (roads, settlements) | Open Street Map, Google earth and department of survey | Vector | Infrastructure overlay with erosion risk |

| | | | | |
|---|---|---|---|---|
| 8 | Landslide & Flood Inventory data | Google earth digitization, Sentinel-1, Google Earth Engine (GEE) | Vector: point or polygon | Landslide and flood mapping |

*3.2.1 Landslide and Flood Inventory*

A landslide and flood inventory is a systematic record of past landslide and flood events in a study area. It includes information about their location, date, type, magnitude, cause, and impact (Feizbahr et al., 2025; Stumpf & Kerle, 2011). Such inventories serve as fundamental datasets for spatial modelling of hazards. risk assessment and early warning systems. The inventory mapping methodology is contingent upon the scale of analysis and intended application, represented as points or polygons (Moosavi et al., 2014). Medium to large-scale inventories typically integrate data from diverse sources, such as scholarly literature, technical reports, field surveys, analysis of historical documents and aerial photos.

The multi-temporal landslide inventory **(Figure 3-3A),** comprising 842 polygons, is considered reasonably robust as it was derived from high-resolution Google Earth imagery and supported by field verification and GPS-based spatial validation. Its reliability is further enhanced through temporal validation **(Algorithm 1)** using NDVI and Basic soil index (BSI) time-series analysis (Wen & Teo, 2022) and change detection techniques. However, the approach is subject to inherent uncertainties and methodological limitations. Factors such as temporal inconsistencies, cloud contamination, seasonal vegetation variability, and positional inaccuracies may affect the accuracy of landslide detection, and some small or vegetation-obscured events may remain unrecorded. Additionally, limited systematic ground-truthing constrains comprehensive validation, suggesting that the mapped landslides and model outputs should be interpreted as reflective rather than conclusive.

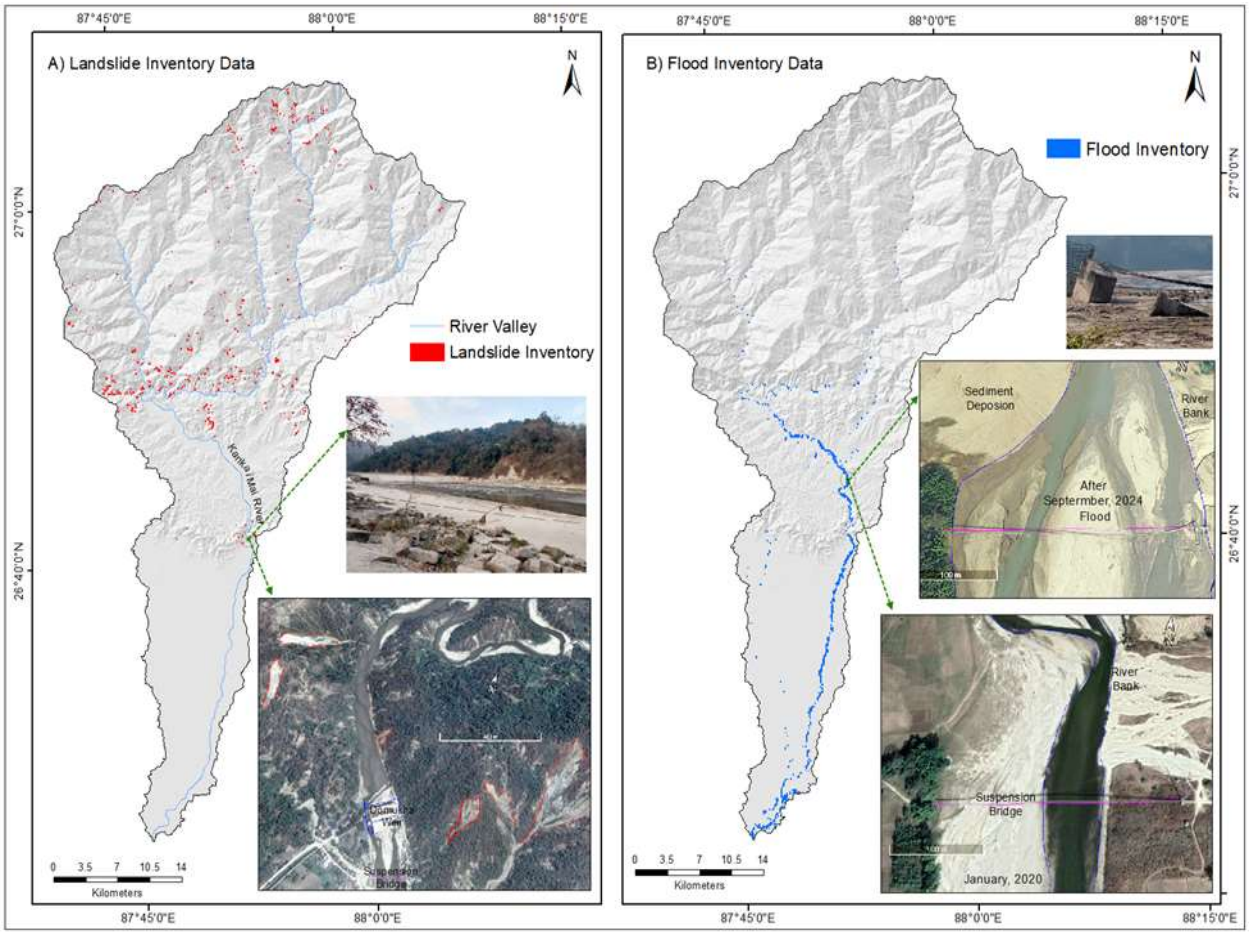


*Figure 3-3: Map showing (A) Landslide Inventory and (B) Flood Inventory Datasets*

Moreover, the susceptibility model primarily relies on static conditioning factors including geomorphology, topography, geology, and hydrology but does not explicitly incorporate dynamic temporal drivers such as land use and rainfall variability, flood frequency, and progressive erosion processes that significantly influence slope instability. The model is also sensitive to factor classification and weighting, where minor variations can lead to notable changes in susceptibility patterns due to the nonlinear nature of landslide processes. Therefore, the resulting susceptibility maps should be regarded as probabilistic representations of hazard conditions under defined assumptions rather than absolute predictions, emphasizing the need for cautious interpretation and application. A flood inventory consisting of 2148 pixels (30 m resolution) is compiled by detecting and recording areas affected by flooding over time **(Figure 3-3A).**

*Algorithm 1: BSI and NDVI time-series analysis using Sentinel-2*

1. Load Digitized Landslide inventory and Sentinel-2 image collection (2018 – 2025) with Cloud percentage < 5%
2. Apply cloud masking and Remove cloud and cirrus pixels using QA60 band
3. Compute spectral indices for each image

   NDVI = (NIR - RED) / (NIR + RED)

   BSI = ((SWIR + RED) - (NIR + BLUE)) / ((SWIR + RED) + (NIR + BLUE))

   where,

   NIR (near-infrared) corresponds to Band 8 (B8).

   RED band corresponds to Band 4 (B4)

   BLUE band corresponds to Band2 (B2)

   SWIR (shortwave infrared) corresponds to Band 11 (B11).
4. Generate monthly composite images for each year
5. Compute mean NDVI and BSI for each landslide polygon
6. Combine all results.

*Algorithm 2: Sentinel-1 Image for Flood Inventory mapping in GEE (Feizbahr et al., 2025)*

1. Choose the closest images for each rainy season (June -September).
2. Ensuring at least 15 consecutive dry days, choose the images for dry period (January – April) corresponding to the wet period
3. Apply a VV polarization (< −13.05 dB) water mask and perform speckle filtering
4. Define water layers for wet and dry conditions
5. Combine every generated image for every year from 2018 to 2025
6. Keep only water pixels recurring for ≥ 3 years to ensure reliability and reduce noise

Satellite images, specifically Sentinel-1 SAR data (2018 – 2025), are collected for wet and dry seasons. Flooded areas are identified where wet-season backscatter drops below a threshold but dry-season water is excluded, and permanent water bodies are masked (**Algorithm 2**). Yearly flood maps are summed to calculate flood frequency, and areas flooded multiple times

are mapped to produce the flood inventory, providing a record of recurrent flood-prone zones.

### *3.2.2 Landslide and Flood Causative Factors*

The spatial assessment of landslide and Flood susceptibility relies on various causative factors that represent key spatial datasets. Based on previous studies (Acharya, 2018; Bhatta & Adhikari, 2024; Chauhan et al., 2025; Feizbahr et al., 2025; Khatakho et al., 2021; Rahmati et al., 2019; Youssef et al., 2022), this study considered 13 conditioning factors for landslide and 17 conditioning factors for flood susceptibility. These conditioning factors were compiled from multiple standardized sources (**Table 3-1 & 3-2**).

*Table 3-2: Data layer & causative factors for spatial assessment different hazards*

| **Datasets** | **Landslide Causing Factor** | **Flood Causing Factor** | **Erosion Causing Factor** |
|---|---|---|---|
| Rainfall | ✓ | ✓ | - |
| Slope | ✓ | ✓ | ✓ |
| Aspects | ✓ | ✓ | - |
| Curvature | ✓ | ✓ | ✓ |
| Elevation | ✓ | ✓ | - |
| NDVI | ✓ | ✓ | - |
| LULC | ✓ | ✓ | - |
| Topographic Wetness Index | ✓ | ✓ | ✓ |
| Sediment Transport Index | - | ✓ | ✓ |
| Stream Power Index | - | ✓ | ✓ |
| Lithology / Geology | ✓ | ✓ | - |
| Soil Types | ✓ | ✓ | - |
| Fault Proximity | ✓ | - | - |

| | | | |
|---|---|---|---|
| Road Proximity | ✓ | - | - |
| River & Streams Proximity | ✓ | ✓ | - |
| Soil Moisture | - | ✓ | - |
| Drainage Density | - | ✓ | ✓ |
| Land Surface Temperature | - | ✓ | - |
| Depression Area | - | ✓ | - |

Topographic parameters (Elevation, Slope, Aspect, Curvature, Drainage Density, depression region) and Hydrological Indices (sediment transport index, Topographic Wetness Index, stream power index) were derived from a 30 m resolution ASTER DEM. Geological and structural data, including fault lines, were digitized from the 1: 1,000,000 - scale national geological map published by the Department of Mines and Geology (DMG) in 1994. Soil data were sourced from the 1:50,000-scale Soil and Terrain Database (SOTER), jointly compiled by the Food and Agriculture Organization (FAO) – 2004, and the Survey Department of Nepal in 2004. Land cover characteristics were defined using the NDVI and LULC classification, computed from Landsat - 8 and Sentinel imagery processed in Google Earth Engine (GEE). Precipitation data, representing mean annual rainfall, were generated from a 25-year record provided by the Department of Hydrology and Meteorology (DHM), Nepal. Soil moisture was estimated from Sentinel - 1 VV and VH backscatter coefficients using an empirical linear model which relates radar backscatter intensity to soil moisture conditions. Land Surface Temperature (LST) was calculated from Landsat - 8 and 9 imagery in GEE, with clouds masked and thermal band converted to °C.

To ensure consistency and comparability, all conditioning factors were standardized to a common system of spatial reference (WGS 1984 UTM Zone 45N) and resampled to a resolution of 30 m, which matches the scale of analysis adopted in this study. This harmonization process ensured that different conditioning factors originating from different sources with varying native resolutions, were aligned to a consistent grid framework. Maintaining a uniform spatial resolution is critical in susceptibility mapping, as mismatched resolutions can introduce spatial inaccuracies, distort relationships between variables, and

bias model outputs. For instance, coarser-resolution datasets may generalize terrain or hydrological features, while finer-resolution data may capture localized variability, leading to inconsistencies when overlaid in a GIS environment. By resampling all datasets to 30 m resolution, this study minimized such discrepancies and ensured that each conditioning factor contributed equally and reliably to the susceptibility analysis.

**Topographical Factors:**

Topographical factors including DEM derivatives (Elevation, Slope, Aspects, Curvature, TWI) and proximity to rivers & streams considered in this study are shown in (**Figure 3-4).** Slope angle is known to be the most significant parameter of landslide and flood occurrence, as it directly governs the gravitational stresses acting upon inherent strength characteristics, such as internal friction and cohesion (Acharya, 2018; Pyakurel et al., 2023; Sharma et al., 2025). Slopes exceeding 5° are generally more vulnerable to failure, while low-gradient and flat terrains tend to experience higher flood susceptibility (Khatakho et al., 2021). The spatial distribution of slope gradients across the study area is presented in (**Figure 3-4 A)**.

Elevation, while its direct role is debated (Kavzoglu et al., 2014), serves as a proxy for precipitation patterns and vegetation distribution affecting slope stability (Ngo et al., 2021; Rahmati et al., 2019). Higher elevation zones are particularly prone to slope failures due to increased steepness and geomorphological instability (Pyakurel et al., 2023). It also influences flooding by controlling runoff flow direction, moisture distribution, temperature, wind patterns, and flood extent and depth (Khatakho et al., 2021). Topographic analysis revealed a significant elevation gradient, with values ranging from 62 m to 3,598 m above mean sea level (masl) within the study area (**Figure 3-4 B**). Slope aspect is a significant hazard conditioning factor, influencing instability through its control on discontinuity orientation, solar radiation, wind exposure, and rainfall patterns (Pokhrel & Bhandari, 2019; Pyakurel et al., 2023). North-facing slopes receive lower solar radiation, resulting in cooler conditions and greater soil moisture retention compared to south-facing slopes (Khatakho et al., 2021). (**Figure 3-4 C)** presents a thematic map of aspects across the study area.

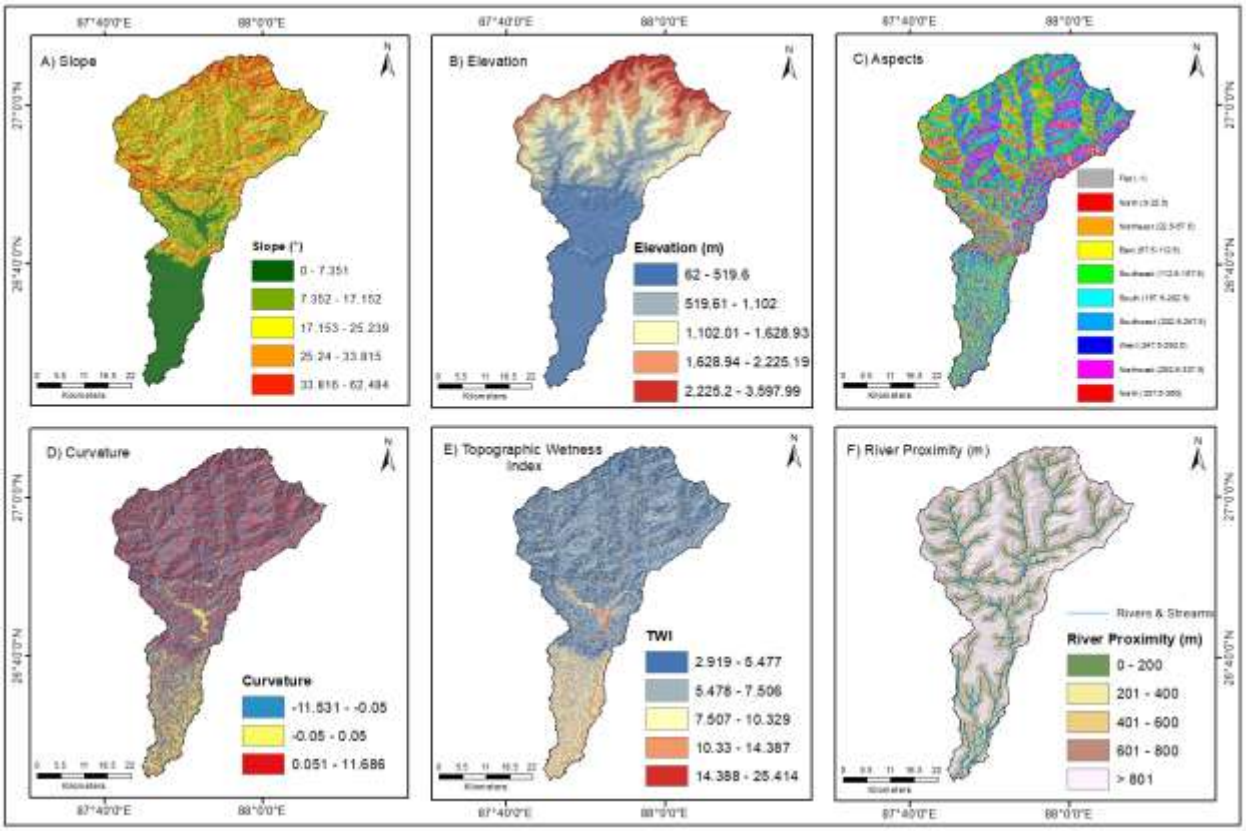


*Figure 3-4: Topographical factors: (A) Elevation, (B) Slope, (C) Aspects, (D) Curvature, (E) TWI and (F) Proximity to Rivers and Streams.*

Curvature (**Figure 3-4 D**), describing the direction of a slope (concavity or convexity), alters the balance of gravitational stresses, thereby influencing the likelihood of mass movement (Acharya, 2018; Khatakho et al., 2021; Pyakurel et al., 2023). Convex slopes typically disperse runoff more evenly, whereas concave slopes tend to accumulate water at the base, increasing hydrostatic pressure and potential instability (Pyakurel et al., 2023). The TWI, calculated from the DEM (**Figure 3-4 E**), quantifies potential soil moisture accumulation to assess pore-pressure-related slope instability (Acharya, 2018; Moazzam et al., 2020). High TWI values pinpoint hydrological conditions conducive to slope failure. TWI is mathematically expressed as (**Eq 3.1**):

$$\mathrm{TWI} = \ln \frac{\alpha}{\tan \beta} \quad \ldots\ldots (3.1)$$

where, $\alpha$ represents the specific catchment area (local upslope drainage area per unit contour length) and tan $\beta$ denotes the tangent of local slope gradient.

Proximity to stream networks significantly elevates landslide risk by saturating soils, reducing shear strength, and accelerating bank erosion (Dai et al., 2002), as mapped in (**Figure 3-4 F)**.

**Geological and Soil Factors:**

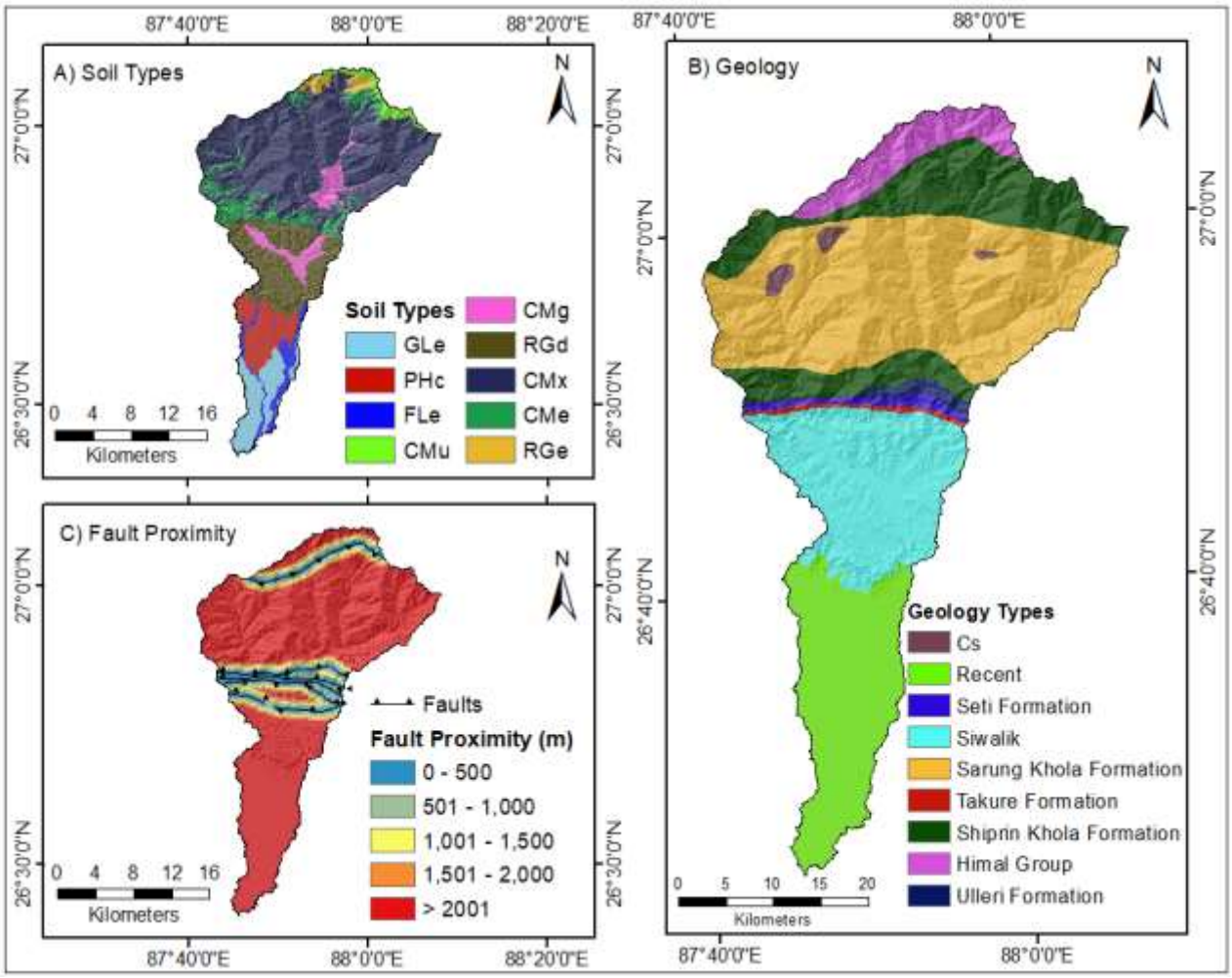


*Figure 3-5: Geological and soil factors: (A) Dominant soil types (GLe: , PHc: , FLe: , CMu: Humic cambisols, CMg: Gleyic cambisols, CMx: Chromic cambisols, RGd: Dystric Regosols, CMe: Eutric Cambisols, RGe: Eutric Regosols), (B) Geology (Cs: Calc-Silicate rocks), and (C) Proximity to faults*

Geological and Pedological characteristics - including lithology, soil type, and proximity to faults considered in this study are shown in (**Figure 3-5).** Fracturing and tectonic stress concentration near faults degrade rock and soil structures within fault zones, which compromises slope integrity and facilitates groundwater infiltration, ultimately leading to slope deformation and failure (Ngo et al., 2021). Landslide potential is strongly influenced by the hydrological properties and shear strength of soil (ADPC, 2010). Using the Soil and Terrain (SOTER) Database, eight dominant soil types were identified (**Figure 3-5A**), each exhibiting distinct geotechnical characteristics affecting landslide potential. The geological framework forms the material basis for slope stability, where lithological properties such as strength and permeability directly govern slope instability (Rahmati et al., 2019). Geological formations (**Figure 3-5B**) derived from a national geological map (DMG, 1994), represent a diverse lithological assemblage, including alluvial deposits of recent formation, sedimentary rocks (sandstone, mudstone) of the Siwalik formation, and various metamorphic rocks (phyllites and schists) of the Himal group (Acharya, 2018). Further, the study area is traversed by major active fault systems (**Figure 3-5C**), including the Main MCT, MBT and MFT, contributing regional seismic activity (R. K. Dahal, 2014; Tiwari & Paudyal, 2023).

**Hydrological and Climatic Factor:**

Hydrological and climatic factors, specifically rainfall and drainage density, play a critical role in slope instability and flooding (Khatakho et al., 2021; Pyakurel et al., 2023). Rainfall intensity and duration significantly influence landslide and flood occurrence, with Prolonged heavy rainfall is a key trigger of landslides, as it raises pore-water pressure, reduces soil shear strength, and destabilizes slopes (Hong et al., 2006; Lin et al., 2021). In addition to directly saturating the soil, intense rainfall contributes to surface runoff, leading river flooding exacerbating risk through bank undercutting and soil saturation (Dai et al., 2002). Precipitation data for this study comprised a 24-year record (2000 – 2024) obtained from six stations maintained by DHM, Nepal. The spatial distribution of rainfall stations and mean annual rainfall, indicating zones of heightened hydrological susceptibility is presented in (**Figure 3-6)**.

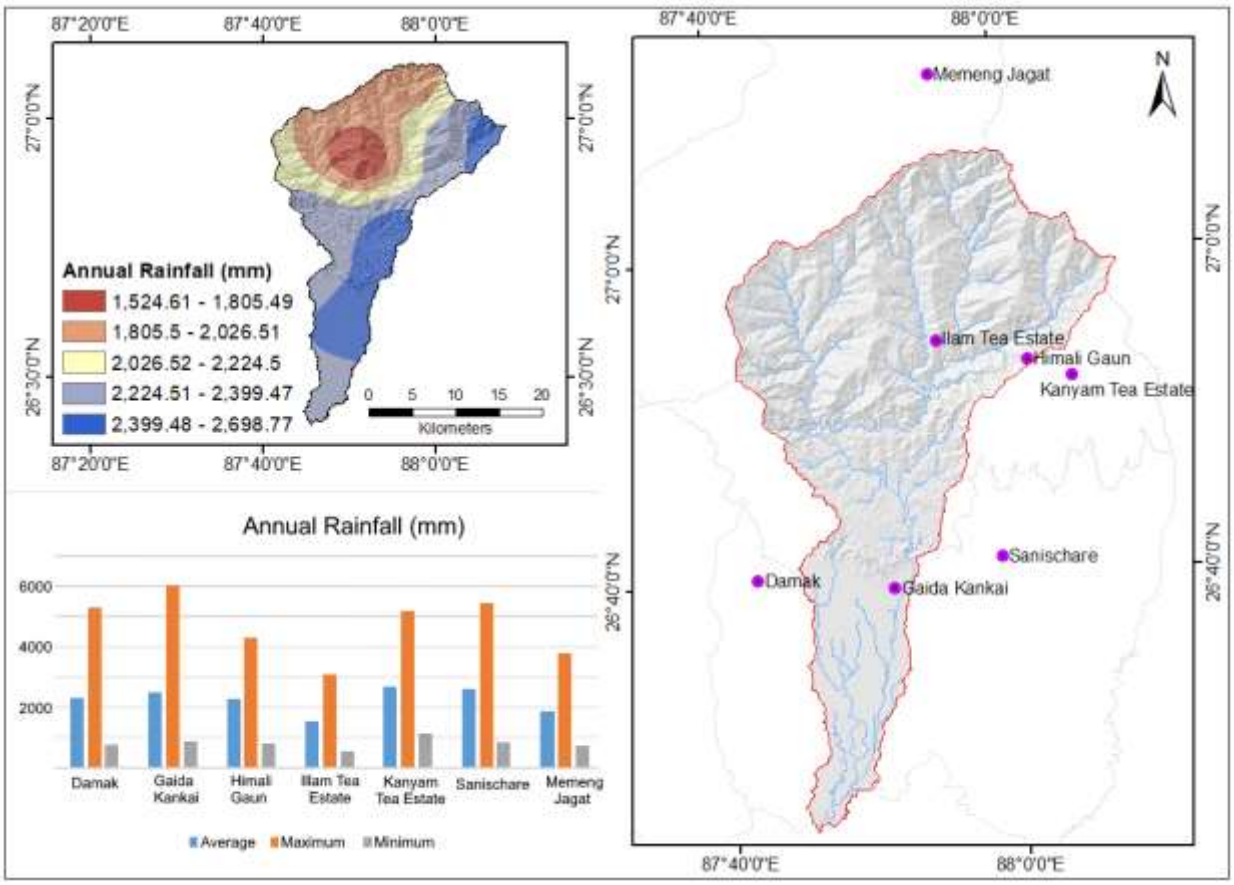


*Figure 3-6: The spatial distribution of rainfall stations and mean annual rainfall*

**Anthropogenic and Environmental Factors:**

Human activities, particularly settlement, road construction and land use changes, are significant drivers of landslide & flood occurrence (Chauhan et al., 2025; Luu et al., 2023). In this study, the influence of anthropogenic activities on landslide & flood susceptibility evaluated through three primary factors (**Figure 3-7**): proximity to roads, NDVI, and LULC.

Unregulated local road construction elevates landslide susceptibility through significant slope alterations (Kavzoglu et al., 2014). Roads, buildings, and pavements prevent infiltration of rainwater into the soil, leading more surface runoff and higher peak flows in rivers and drainage systems (Khatakho et al., 2021). The NDVI, quantifies live green vegetation density and serves as a key indicator for landslide susceptibility analysis (Niraj et al., 2023). Higher NDVI values ( > 0.36) indicate dense vegetation that reinforces slopes, while lower values (0 - 0.1) denote bare ground with reduced stability, and negative values

typically represent water bodies (Doan et al., 2023). Conversions to agriculture and improper grading practices elevate landslide risk by reducing root reinforcement and weakening slope integrity (Niraj et al., 2020).

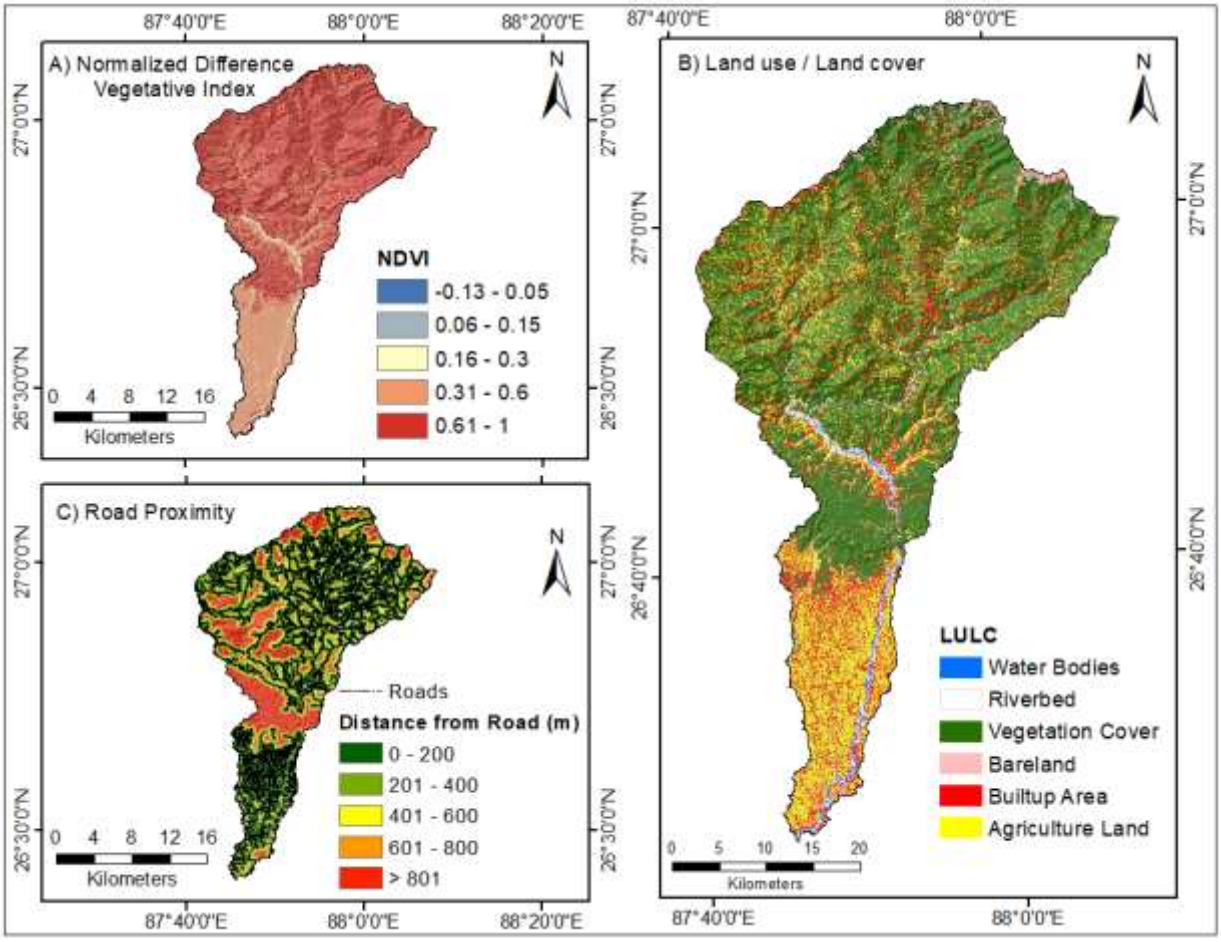


*Figure 3-7: Anthropogenic factors: (A) NDVI, (B) LULC, and (C) Proximity to roads*

**Hydrological Indices and Terrain factors:**

Integration of hydrologic indices and terrain characteristics in a GIS environment allows the characterization of sediment transport, erosion potential, and areas prone to flood-induced soil degradation (Bannari et al., 2017). Several hydrological indices (**Figure 3-8**) have been developed to quantify these processes. The Sediment Transport Index (STI), based on Moore and Wilson's unit stream power theory (**Eq 3.2**), calculates spatially distributed sediment transport capacity and improves landscape-level erosion assessment by considering flow convergence and divergence (Bannari et al., 2017; Moore & Wilson, 1992). Higher STI values

indicate regions where runoff can carry significant sediment, contributing to channel aggradation and localized flooding.

$$STI = [(m+1) (A_s / 22.13)^{m} (\sin \beta / 0.0896)^{n}] \quad \text{(3.2)}$$

where, $A_s$ = flow accumulation * cell size, β = slope in radian, m = 0.4 and n = 1.3.

Land Surface Temperature (LST) influences evaporation rates and soil moisture retention; warmer areas may experience reduced infiltration, increasing surface runoff during rainfall events (Demissie et al., 2024). LST was extracted from Landsat 8 and 9 Collection 2 Level-2 data using Google Earth Engine (GEE). Thermal Band 10 digital numbers were converted to top-of-atmosphere radiance and then to brightness temperature (Kelvin) using the inverse Planck function. Annual and mean LST maps for 2015–2025 were produced by averaging the derived temperature values. Soil Moisture directly affects infiltration capacity, with wetter soils being less able to absorb additional rainfall, thereby increasing flood potential (Cenci et al., 2017). Soil moisture was estimated using Sentinel-1 SAR GRD imagery (VV and VH polarization) processed in Google Earth Engine for the year 2025. Empirical equations were applied to derive soil moisture (SM) from SAR backscatter values (**Eq 3.3**). The processed images were averaged to generate a mean soil moisture map**.**

$$SM = (66.68699279 + VH \times 1.335902794 + VV \times 1.522517177) \quad \text{(3.3)}$$

where, VH = Vertical transmit – Horizontal receive polarization backscatter coefficient (dB) and VV = Vertical transmit – Vertical receive polarization backscatter coefficient (dB).

Drainage density refers to the total stream length per unit area, where higher values indicate a more developed drainage network with faster runoff response, which can lead to flash flooding downstream (Ahmad et al., 2019). Depression Areas identify low-lying zones that naturally accumulate water, acting as potential flood-prone regions during heavy precipitation (Feizbahr et al., 2025). In GIS-based terrain analysis, depression areas are commonly identified using a DEM (**Eq 3.4**). The resulting raster highlights areas where water is likely to accumulate, thereby indicating potential flood-prone locations.

Depression areas = Filled DEM − Original DEM …… (3.4)

Finally, Stream Power Index is a semi-empirical hydrological index (**Eq 3.5**) that reflects the erosive force of flowing water. It is widely applied to estimate sediment transport rates in basin hydrology and to assess areas with higher runoff energy that may contribute to flood hazard (Ahmad et al., 2019; Bannari et al., 2017).

SPI = [ln(($A_s$ + 0.001).((% slope /100) + 0.001))] …… (3.5)

where, ln = Napierian logarithm & $A_s$ is the flow accumulation * cell size

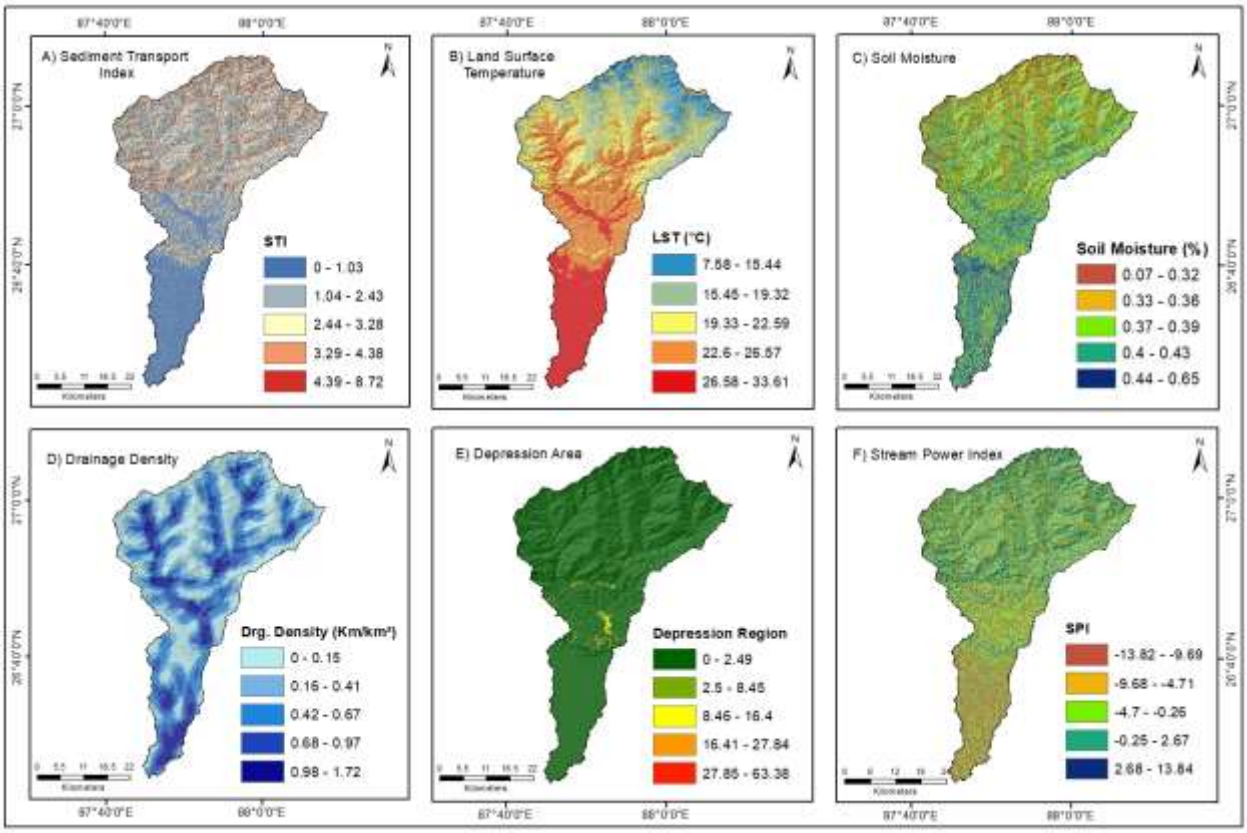


*Figure 3-8: Hydrological Indices and Terrain factors: (A) Sediment Transport Index, (B) Land Surface Temperature, (C) Soil Moisture, (D) Drainage Density, (E) Depression Area, and (F) Stream Power Index*

*3.2.3 Soil Erosion Predictors*

Soil erosion, primarily driven by water, leads to the loss of fertile topsoil, nutrient depletion, and reduced agricultural productivity (Borrelli et al., 2021; Majhi et al., 2021). Biophysical factors such as soil properties, climate, vegetation, and terrain characteristics (slope, aspect, length) interact to control the intensity and pattern of erosion. Soil erosion models apply mathematical formulations to simulate detachment, transport, and deposition of soil, incorporating terrain, soil, land use, and climate factors. They are necessary tools for predicting soil loss and identifying erosion-prone areas for effective land use planning and management (P.U. et al., 2017). Soil erosion assessment methods are either qualitative - identifying erosion-prone areas using terrain and hydrological factors in GIS, or quantitative - quantifies average annual soil loss (Jahun et al., 2015).

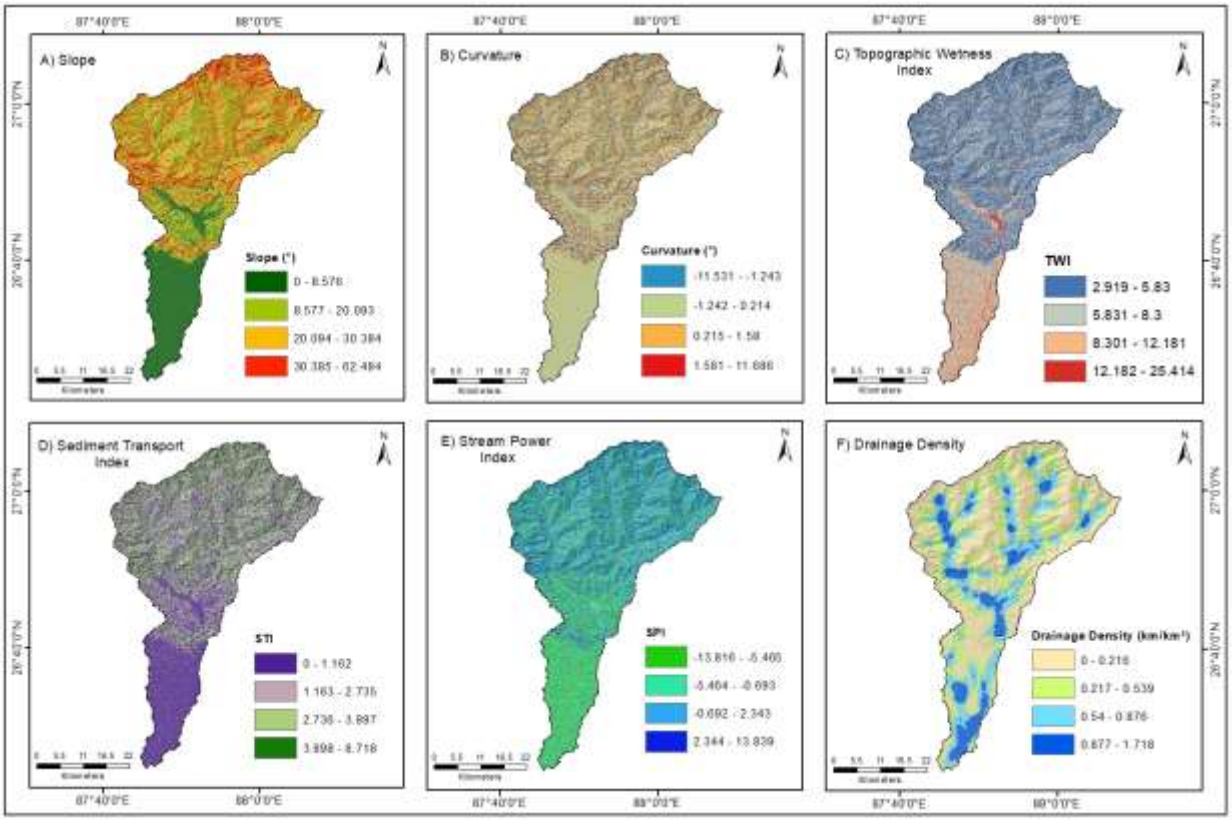


*Figure 3-9: Topographic Factors and Hydrological Indices for Qualitative Soil Erosion Assessment: (A) Slope, (B) Curvature, (C) Topographic Wetness Index, (D) Sediment Transport Index, (E) Stream Power Index, and (F) Drainage Density*

In this study, six key factors - Slope, Curvature, TWI, STI, SPI, and Drainage Density were used to qualitatively assess soil erosion potential, particularly riverbank erosion by employing the weight of overlay method (**Figure 3-9**). The integration of DEM derived morphometric parameters and hydrological indices in a GIS environment has been proven effective for identifying erosion-prone zones and understanding spatial distribution of land degradation (Ahmad et al., 2019). These indices represent the combined influence of terrain morphology and hydrological processes controlling erosion and sediment transport. Further, the RUSLE model employed for quantitative estimation of average annual soil loss using five key parameters - rainfall erosivity (R), soil erodibility (K), slope length and steepness (LS), land cover management (C), and conservation practice (P) factor (**Figure 3-10 to 3-14**). The integration of qualitative terrain analysis and RUSLE model within a GIS environment provides a comprehensive approach for assessing soil erosion risk.

**Rainfall Erosivity Factor:**

Rainfall is a fundamental prerequisite for the occurrence of water-driven soil erosion. The R-factor represents rainfall erosivity, computed as the annual sum of storm EI values and averaged over long-term records (≥ 20 years) to reflect recurring patterns (Jahun et al., 2015; P.U. et al., 2017). Here, EI represents the product of a storm's total energy (E, MJ $ha^{-1}$) and its maximum 30 - minute intensity ($I_{30}$, mm $h^{-1}$), called the storm erosivity index ($EI_{30}$) (Wischmeier & Smith, 1978).

Rainfall erosivity quantifies the impact of raindrops and reflects the amount and intensity of runoff generated by rainfall and its unit is expressed in MJ mm $ha^{-1}$ $h^{-1}$ $yr^{-1}$ (Koirala et al., 2019). Calculation of R-factor needs recording of precipitation at short time intervals ($I_{30\ min}$) for a period of several years which makes its complex in data sparse country like Nepal. Many literatures have proposed several linear and non-linear empirical equations based on the rainfall intensity, or monthly and annual rainfall to estimate the rainfall erosivity across different regions and scales (Ghosal & Das Bhattacharya, 2020; Majhi et al., 2021). For this research, rainfall erosivity was derived using the empirical equation (**Eq 3.6**) developed by **Babu et al. (2004)**, based on annual rainfall, which is commonly applied in India and the

Nepal Himalaya (Koirala et al., 2019).The R factor is computed with 25 years average annual rainfall data from 6 rain gauge stations within and around the basin (**Figure 3-7 & 3-11**).

$R = 81.5 + 0.38\ P$ …… (3.6)

where, R = Rainfall Erosivity Factor (MJ mm $ha^{-1}$ $h^{-1}$ $yr^{-1}$), P = Mean Annual Rainfall (mm)

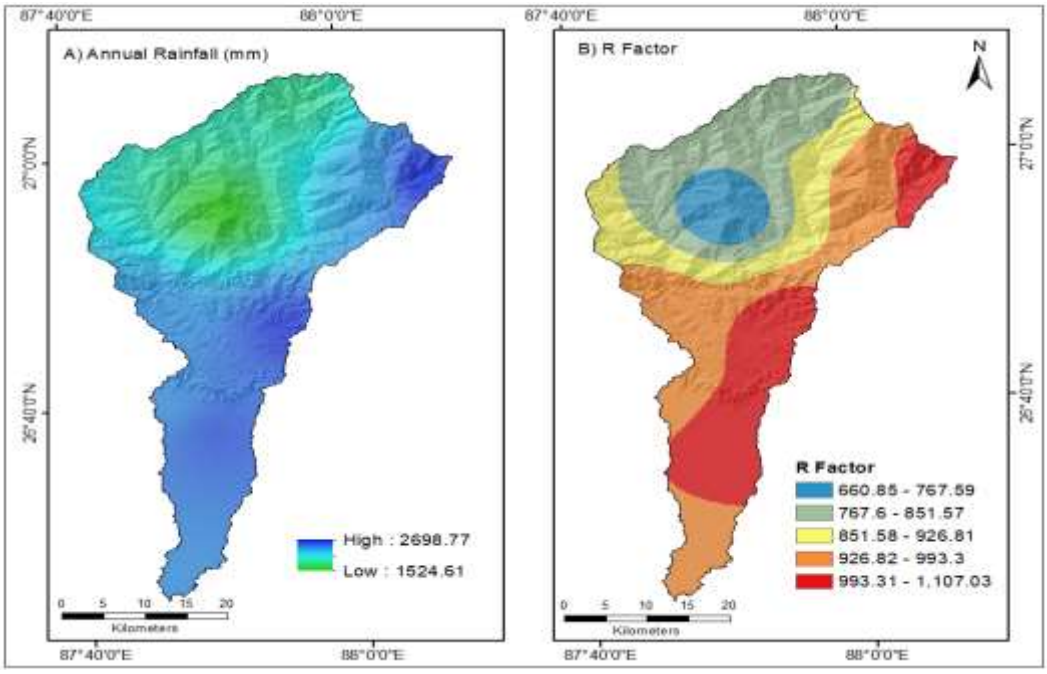


*Figure 3-10: Rainfall Erosivity Factor map for RUSLE soil Loss model*

**Soil Erodibility Factor:**

Soil erodibility reflects an intrinsic vulnerability of soil to water erosion and is a key parameter in soil loss estimation and conservation planning. The K-factor depends on soil physical and chemical properties, including grain size distribution, permeability, organic matter content, and soil structure. Soils with low silt content generally exhibit lower erodibility, regardless of sand or clay fractions (Koirala et al., 2019). Various algorithms exist to calculate K based on regional soil characteristics and study requirements (Luvai et al., 2022; Uddin et al., 2016). For a given soil, the erodibility factor is defined as the erosion rate per unit erosion index under standard plot conditions (22.13 m length and 9 % slope). It represents the rate of soil loss per unit of rainfall erosivity (Wischmeier & Smith, 1978). The

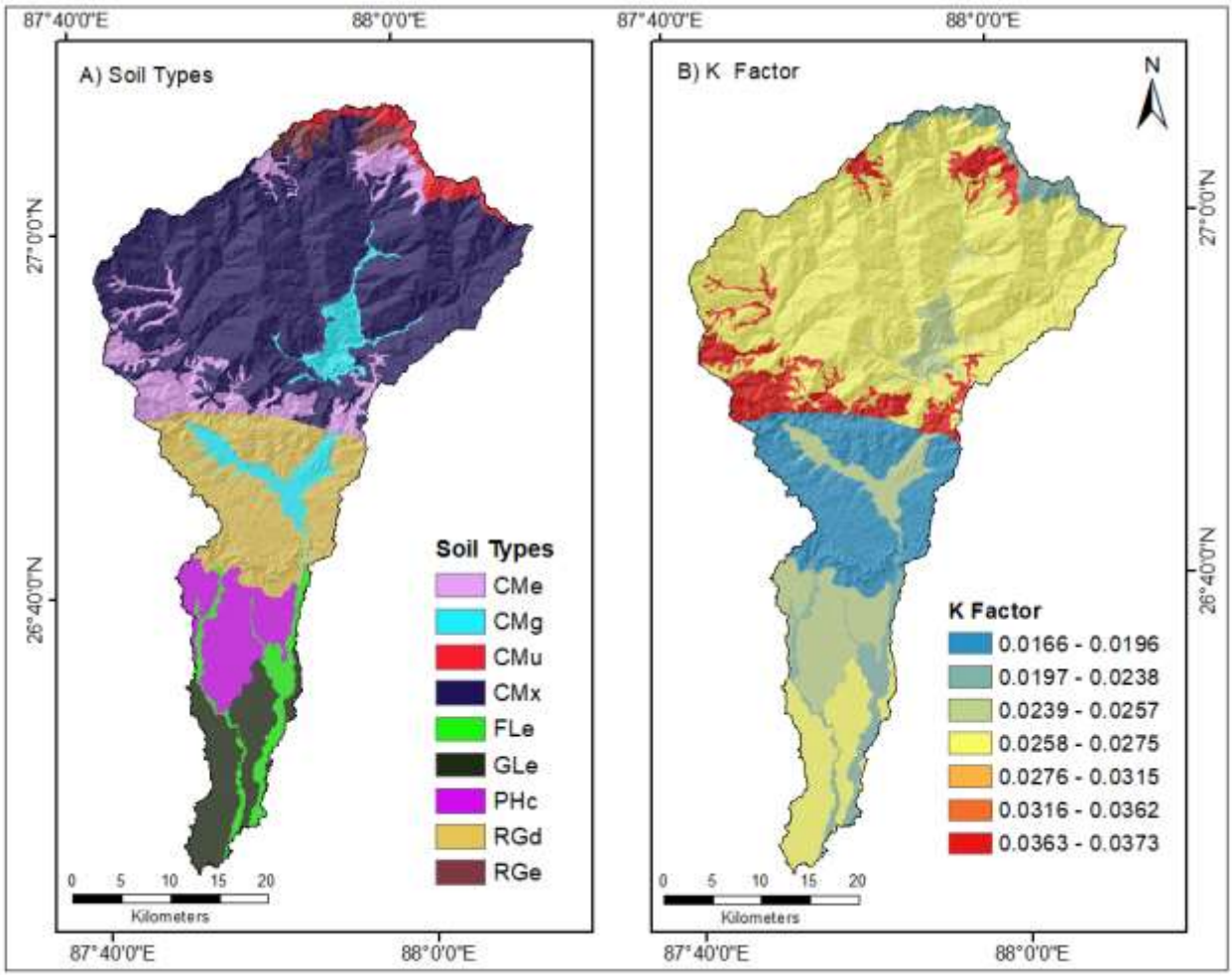


*Figure 3-11: Soil Erodibility Factor map for RUSLE soil Loss model*

soil erodibility was estimated using the alternative equation (**Eq 3.7**) provided by (Sharply & William, 1990) due to the lack of permeability and soil structure data required by the original equation provided by (Wischmeier & Smith, 1978).

$$K = \left[0.2 + 0.3 \times \exp\left[-0.0256 \times SN \left\{1 - \left(\frac{SI}{100}\right)\right\}\right]\right] \times \left(\frac{SI}{CL+SI}\right)^{0.3} \times \left[1 - \frac{0.25C}{C + \exp(3.72 - 2.95\,C)}\right] \times \left[1 - \frac{0.7\,SN_1}{SN_1 + \exp(-5.51 + 22.9SN_1)}\right] \times \frac{1}{7.59} \quad \ldots\ldots (3.7)$$

where, K is soil erodibility in t. ha. h. $MJ^{-1}$ .$mm^{-1}$ .$ha^{-1}$, SN is % Sand content, SI is % Silt content, CL is % Clay content, C is % Organic Carbon content and $SN_1 = \left(1 - \frac{SN}{100}\right)$

The soil parameters - sand %, silt %, clay %, and organic carbon % were obtained from the Digital Soil Map of the World (2007) produced by FAO - UNESCO at a 1: 5,000,000 scale (https://www.fao.org/soils-portal/data-hub/soil-maps-and-databases/faounesco-soil-map-of-the-world/en/).

**Slope Length & Steepness Factor:**

The LS factor expresses how slope length (L) and slope gradient (S) together affect soil erosion. It reflects the role of terrain in controlling runoff speed and erosion risk, with longer and steeper slopes typically leading to higher soil loss (Majhi et al., 2021). In GIS-based RUSLE applications, LS-factor is commonly derived from DEM data using flow accumulation and slope to capture topographic effects on erosion.

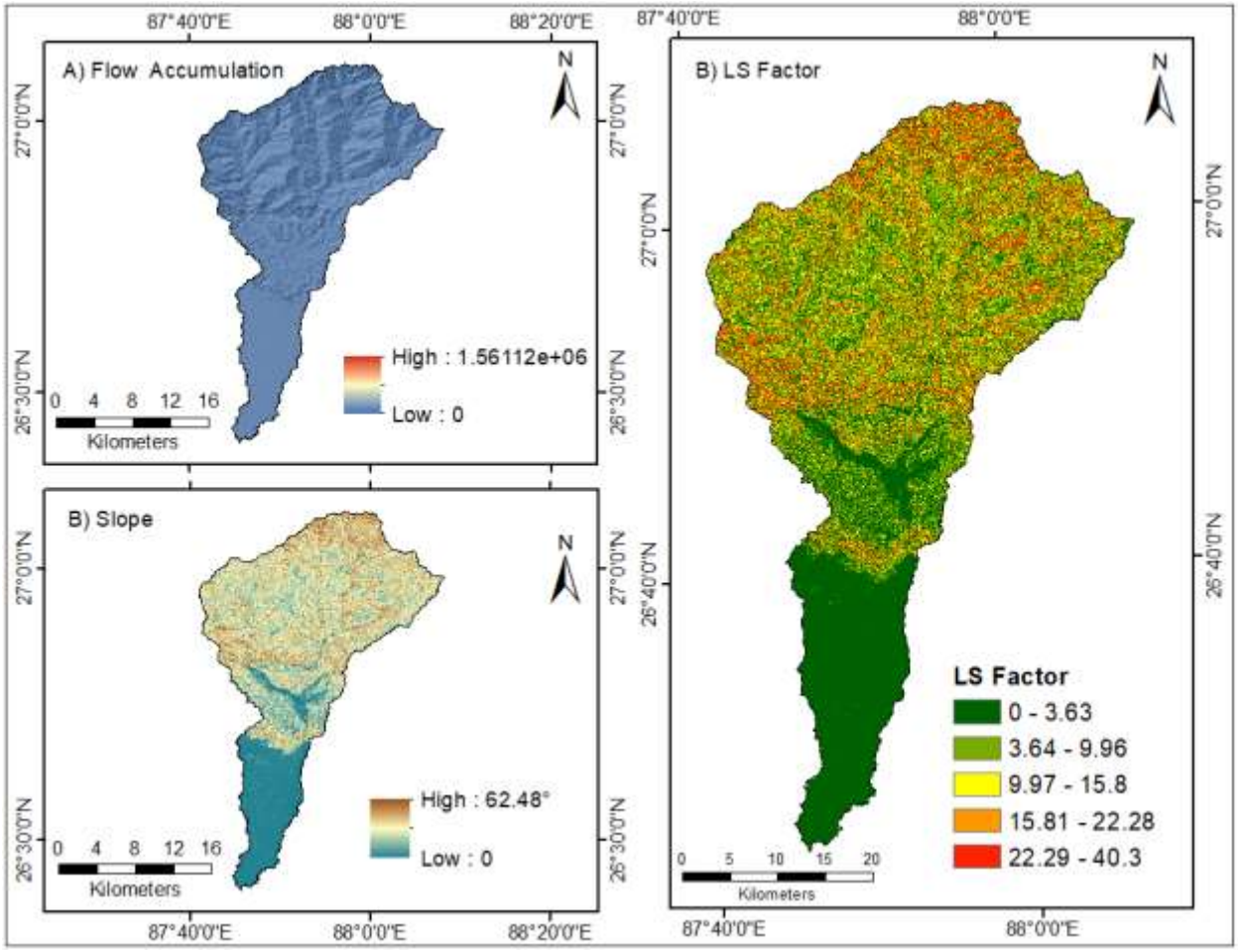


*Figure 3-12: Length of Slope and Steepness Factor map for RUSLE soil Loss model*

The following relation given by (Moore & Wilson, 1992) is used to estimate the LS-factor for this study.

$$\boldsymbol{LS} = \left(\frac{\boldsymbol{As}}{\boldsymbol{22.13}}\right)^{\mathbf{m}} \times \left(\frac{\sin\,\boldsymbol{\theta}}{\boldsymbol{0.0896}}\right)^{\mathbf{1.3}} \quad \text{..... (3.8)}$$

where, $A_s$ = unit contributing area (flow accumulation × cell size), $\theta$ = slope angle and m = 0.4 – 0.6

**Cover Management Factor:**

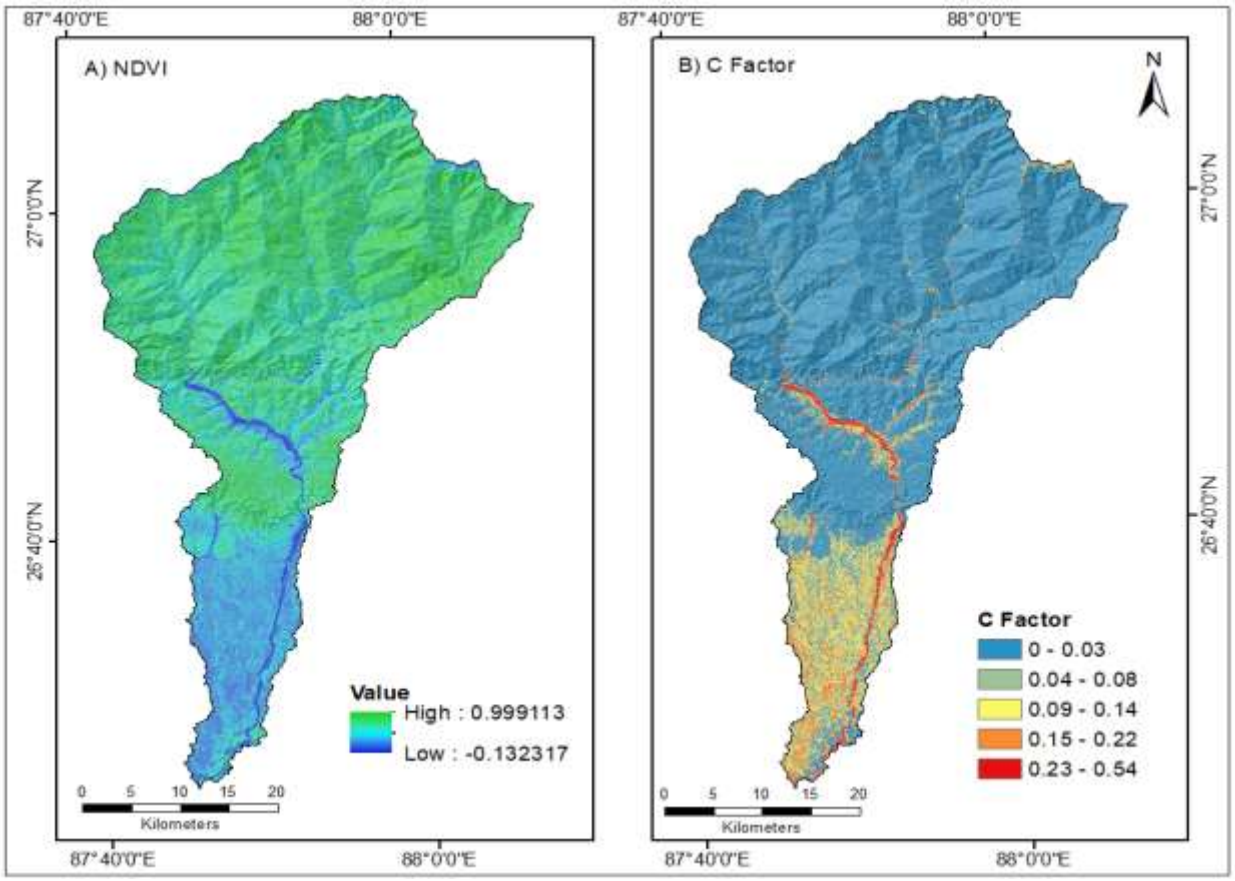


*Figure 3-13: Cover Management Factor map for RUSLE soil Loss model*

The C-factor describes the effect of vegetation cover and land management practice on soil erosion. It is defined as the ratio of soil loss under specific cover conditions to that from bare

soil, with values ranging from 0 to 1 depending on land cover type. Vegetation reduces erosion by intercepting rainfall, dissipating raindrop energy, and increasing infiltration, thereby protecting the soil surface. Previous studies (Ghosal & Das Bhattacharya, 2020; Koirala et al., 2019; Majhi et al., 2021) have reported typical ranges of C factor values based on LULC classes. Generally, forests and shrubland range around 0.001 - 0.03, grassland 0.1, agricultural land ranges from 0.2 to 0.4, sand beaches 1, and barren land ranges from 0.4 to 0.5, indicating higher susceptibility to soil erosion. In contrast, water bodies, snow/glacier, and built-up areas generally have values close to 0.

In many recent studies, however, the C factor is also estimated using NDVI to represent spatial variation in vegetation cover more accurately (Tian et al., 2021). Therefore, in this study we used equation **(Eq 3.9)** developed by (De Jong, 1994) based on NDVI (Luvai et al., 2022).

$$C = 0.431 - 0.805 \times NDVI \quad \text{..... (3.9)}$$

**Support Practice Factor:**

The P-factor represents the influence of conservation practices on the rate of erosion in cultivated lands. Common practices include contouring, cropping, and terracing, which help reduce soil loss (Wischmeier & Smith, 1978). The P-value ranges from 0 to 1, where 0 indicates effective soil conservation measures and values near 1 reflect absence of erosion control practices (Haregeweyn et al., 2017; Olorunfemi et al., 2020).

*Table 3-3: Adopted value of P factor based on different land use*

| SN | LULC class | P-Factor |
|---|---|---|
| 1 | Water Body | 1.0 |
| 2 | Forests | 0.5 |
| 3 | Croplands | 0.4 |
| 4 | Built-up | 0.9 |
| 5 | Bare Land | 0.8 |
| 6 | Riverbed and sand | 0.8 |

Since the study area spans a river valley with a gradient from flat Terai plains to steep hills, exhibiting high elevation differences, the P factor was applied based on LULC as per previous study (Haregeweyn et al., 2017; Majhi et al., 2021; Tian et al., 2021) to account for varying erosion control practices across different land cover types (**Table 3-3**).

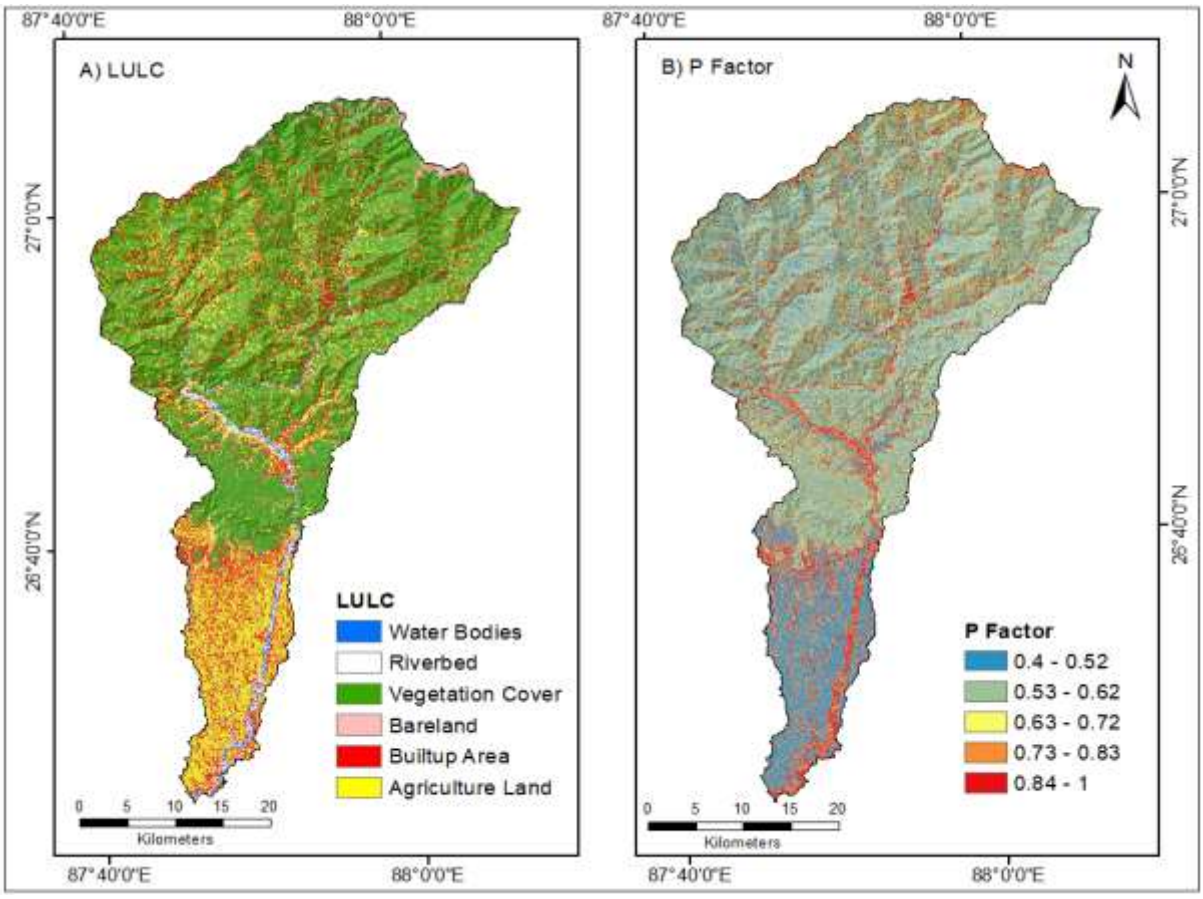


*Figure 3-14: Support Practice Factor map for RUSLE soil Loss model*

### 3.3 Data Sampling and Preparation

Balanced datasets of landslide and flood occurrences, along with non-occurrence samples, are critical for reliable machine learning–based hazard susceptibility modeling, though the selection of non-landslide locations is inherently subjective (Merghadi et al., 2020; A. X. Zhu et al., 2019). In this study, hazard present and absent samples were generated using a pixel-based sampling approach, where hazard-absent locations were randomly selected from stable terrain with a minimum 500 m buffer from known landslide sites. The dataset was

labeled for binary classification (1 = hazard presence, 0 = absence) and processed within an integrated GIS - Python environment, including extraction of values for predictors.

The final dataset was randomly partitioned into two subsets, with 70 % used for training and 30 % reserved for testing. The significance of conditioning factors was assessed using factor screening techniques, including correlation analysis (Pearson) and multicollinearity testing via Variance Inflation Factor (VIF). Multicollinearity (strong correlation) among predictors can compromise stability and interpretability of the model (Merghadi et al., 2020; Thapa et al., 2023). For a given predictor $X_i$, VIF is calculated as:

$$VIF_i = \frac{1}{1-R_i^2} \quad \text{(3.10)}$$

where, $R_i^2$ is the determination coefficient obtained by regressing $X_i$ against all other predictors.

A VIF of ≤ 1 indicates no multicollinearity, values < 5 are acceptable, and values above 10 signify severe multicollinearity requiring corrective action such as removing variables or using Principal Component Analysis (Merghadi et al., 2020).

# 4 Methodology

## 4.1 Research Approach

This study adopted an integrated multi-hazard modeling framework to analyze rainfall-induced cascading hazards: landslides, floods, and soil erosion, in the Kankai Basin, Nepal, using geospatial and machine learning techniques. Landslide and flood susceptibility maps were generated using the SVM model, which was selected due to its excellent performance with limited high-dimensional geospatial data, its ability to model complex non-linear relationships among conditioning factors through kernel functions, and its robust generalization capability that enhances prediction accuracy and lessens overfitting. Compared to other machine learning models, SVM performs effectively with smaller datasets, requires less computational effort, and provides stable classification results for binary problems like hazard presence and absence.

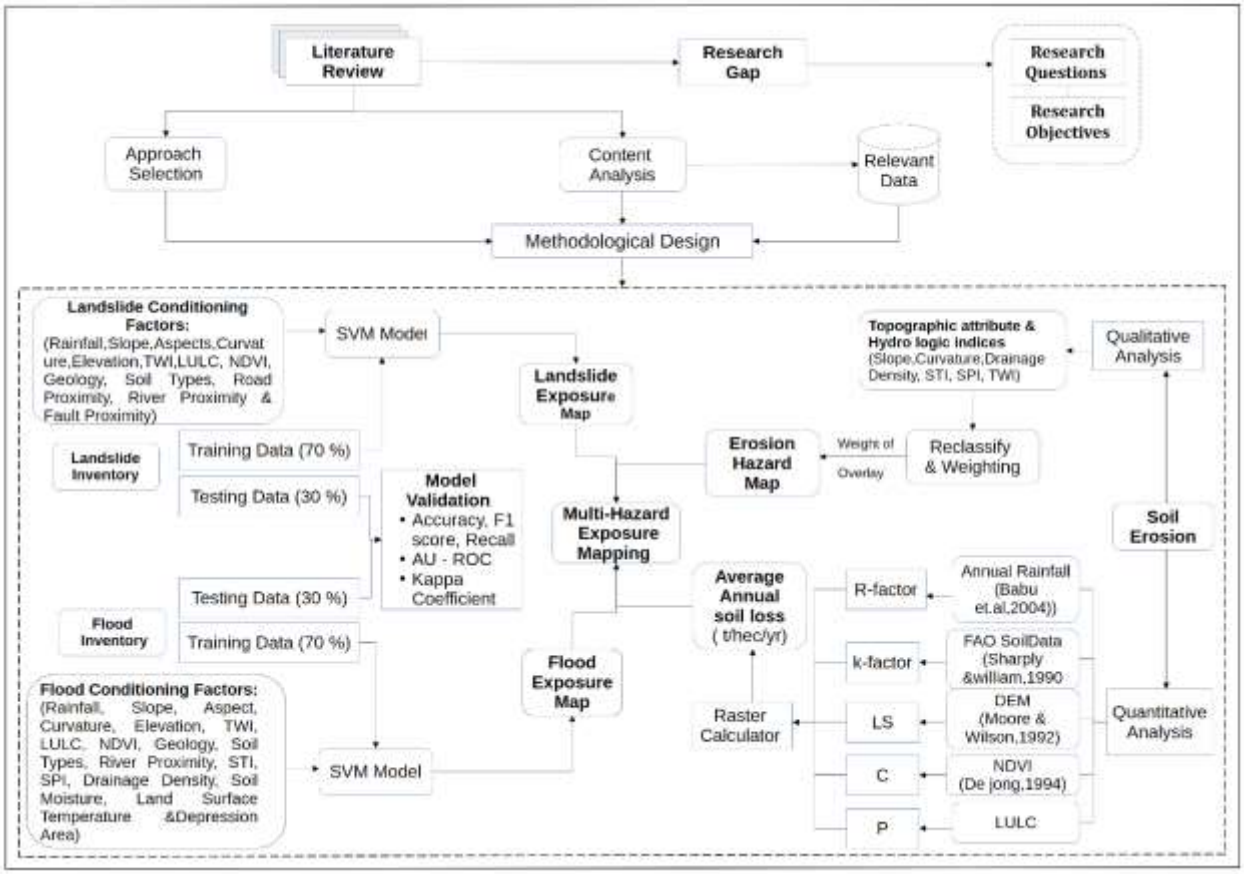


*Figure 4-1: Methodological Framework of the Study*

Landslide inventories and historical flood locations were compiled from field surveys, satellite imagery, and secondary sources, while relevant conditioning factors including elevation, slope, aspects, curvature, land use land cover, rainfall, distance from river, soil type, and drainage density, were derived from Digital Elevation Model (DEM) and other spatial datasets using GIS and remote sensing techniques. Presence and absence samples were then extracted and used to train and validate the SVM model. Soil erosion was assessed using both qualitative and quantitative GIS-based approaches. Erosion hotspot areas, particularly along riverbanks, were first identified using a Weighted Overlay Method by integrating slope, rainfall, soil type, land cover, and proximity to streams. Quantitative estimation of annual average soil loss was then carried out using the Revised Universal Soil Loss Equation (RUSLE) model through its R, K, LS, C, and P factors. RUSLE was selected due to its suitability for large-scale basin analysis, low data requirements, and wide application in Himalayan regions, whereas more complex models such as WEPP were not feasible due to data limitations. Although RUSLE estimates long-term average soil loss and does not explicitly simulate extreme rainfall events, the rainfall erosivity factor partially reflects rainfall intensity, while peak storm-related erosion may still be underestimated. Finally, soil erosion risk outputs were integrated with landslide and flood susceptibility results using a weighted overlay approach, with Weights were first assigned using AHP and then tested with Monte Carlo simulations to reduce uncertainty. The methodological framework is presented in **(Figure 4-1)**.

### 4.2 Landslide and Flood Susceptibility Modeling : Support Vector Machine

Support Vector Machine is a widely adopted supervised learning method for binary classification problem. It aims to determine an optimal separating hyperplane in an n-dimensional feature space that serves as the decision boundary between classes. The fundamental objective of SVM is to maximize the margin between the closest data points of each class (called support vectors), thereby enhancing the model's generalization capability and classification performance (Lee et al., 2017; Singh et al., 2023). It is based on two key ideas: identifying an optimal linear boundary for classification and using kernel functions to map nonlinearly separable data into a higher-dimensional space where linear separation

becomes feasible (Acharya, 2018; Lee et al., 2017). SVM addresses complex classification problems by transforming input features into a higher-dimensional feature space through kernel functions, where it determines an optimal hyperplane that maximizes the margin between classes.

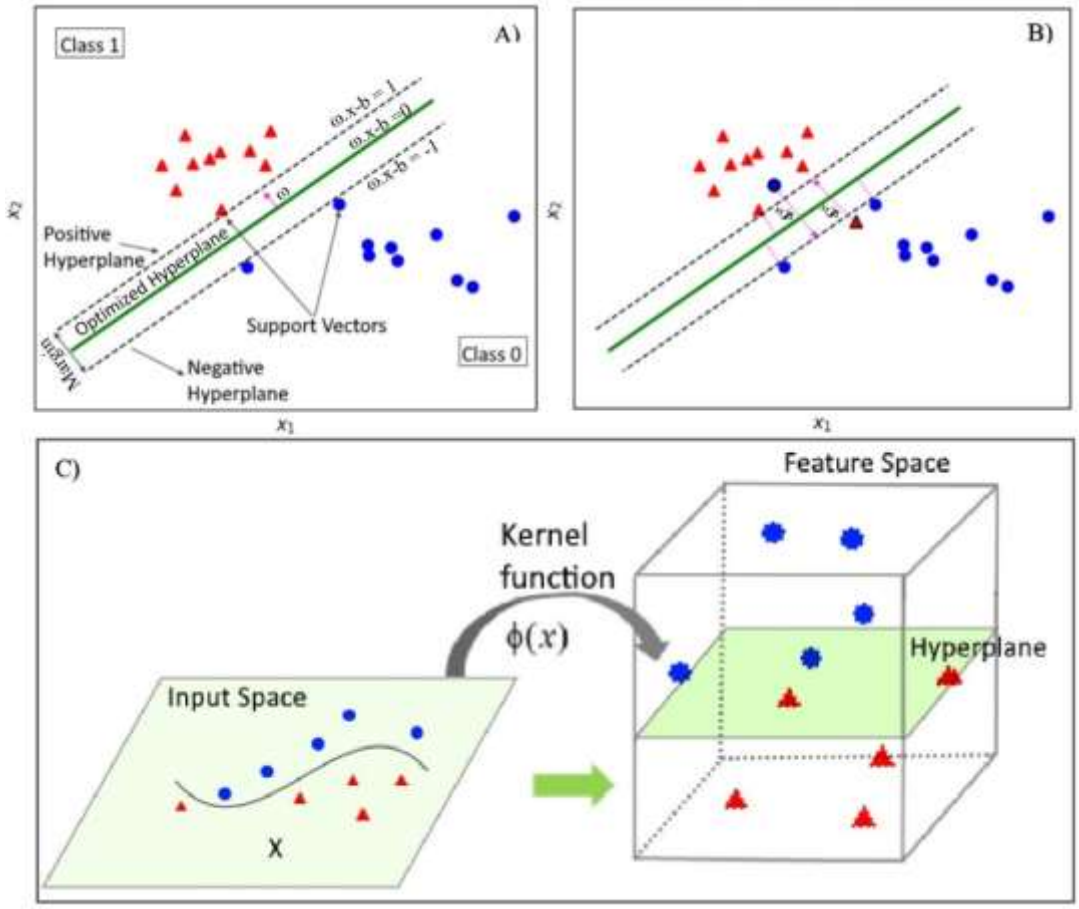


*Figure 4-2: A) Different elements of support vector machine model. B) ) non - separable case and slack variables ξi (Lee et al., 2017). C) Concept of transformation of input space to high dimensional feature space (Dou et al., 2019), where, Φ is a mapping function*.

For linearly separable training data ($x_i$), SVM determines the hyperplane that maximizes the separation margin between the two classes (**Figure 4-2 A**), which is defined as:

$$\frac{1}{2} \| \omega \|^2 \quad \text{..... (4.1)}$$

Subjected to the constraints:

$$z_i\big((\omega \cdot x_i) + b\big) \geq 1 \quad \ldots\ldots (4.2)$$

where, $||\omega||$ is the weight vector, b is a shift of the decision boundary from the origin, $x_i$ represent the input features and (.) denotes the scalar product.

The cost function can be defined using the Lagrangian multiplier ($\lambda_i$) as:

$$L = \frac{1}{2} \| \omega \|^2 - \sum_{i=1}^{n} \lambda_i \big(z_i\big((\omega \cdot x_i) + b\big) - 1\big) \quad \ldots\ldots (4.3)$$

The solution of **(Eq 4.3)** is obtained via a dual minimization process with respect to 'ω' and 'b'. For non-linearly separable data (**Figure 4-2 B**), the slack variable $\xi_i$ introduced to reformulate **(Eq 4.2)** (Lee et al., 2017).

$$z_i\big((\omega \cdot x_i) + b\big) \geq 1 - \xi_i \quad \ldots\ldots (4.4)$$

$$L = \frac{1}{2} \| \omega \|^2 - C \sum_{i=1}^{n} \xi_i \quad \ldots\ldots (4.5)$$

where, C is introduced to control misclassification errors. Furthermore, a kernel function used to handle non-linear decision boundaries (**Figure 4-2 C**), which computes the dot product of transformed data $\Phi(x)$ in a higher-dimensional feature space (Cortes & Vapnik, 1995).

$$K(x_i , z_j) = \Phi(x_i) \cdot \Phi(z_j) \quad \ldots\ldots (4.6)$$

## 4.3 Soil Erosion Modeling

*4.3.1 Qualitative Erosion Modeling: Weight of Overlay Method*

A qualitative assessment of soil erosion was conducted to delineate areas prone to erosion based on terrain and hydrological characteristics derived from a DEM and associated thematic datasets (Ahmad et al., 2019). The analysis aimed to identify zones with relatively higher susceptibility to soil erosion, particularly riverbank erosion, using the Weighted Overlay Method within a GIS environment. This approach emphasizes relative spatial

susceptibility instead of absolute soil loss estimation, making it appropriate for regional-scale studies and data-scarce environments.

Six key geomorphological and hydrological factors; slope, curvature, TWI, STI, SPI, and drainage density were used to evaluate erosion susceptibility. A 30 m resolution DEM served as the primary dataset for deriving topographic and hydrological parameters. The DEM was preprocessed using a sink-filling procedure to ensure hydrological consistency, followed by the generation of flow direction and flow accumulation grids using the D8 algorithm. These outputs were subsequently used to derive drainage networks and compute hydrological indices associated with erosion processes. SPI, STI, and TWI were calculated through raster-based spatial analysis to represent runoff erosive power, soil moisture accumulation potential, and sediment transport capacity, respectively (Bannari et al., 2017), while slope, curvature, and drainage density were derived to characterize the geomorphological controls influencing soil erosion susceptibility.

All derived indices and thematic layers were reclassified into four ordinal erosion susceptibility classes. These layers were then integrated using a weighted linear combination approach (**Eq 4.7**) to generate a spatially distributed erosion susceptibility map. The resulting map was normalized and reclassified into different erosion hazard zones representing from low to very high. This qualitative approach offers a spatial framework for identifying erosion hotspots, guiding soil conservation priorities, and supporting sustainable watershed management.

$$QSE = \sum_{i=1}^{n} w_i r_i \qquad (4.7)$$

where, QSE = Qualitative soil erosion index, $w_i$ = weight assigned to the $i^{th}$ factor and $r_i$ = reclassified score of the $i^{th}$ factor and n = no. of features considered for erosion analysis.

*4.3.2 Quantitative Erosion Modeling: RUSLE Soil Loss Model*

The Revised Universal Soil Loss Equation (RUSLE) estimates rill erosion based on soil properties, climate, topography, and land use factors. Raindrop impact and surface runoff cause inter-rill erosion (Renard et al., 1991). The model integrates five factors: slope length-gradient (LS), rainfall erosivity (R), soil erodibility (K), cover-management (C), and support practices (P) to estimate annual average soil loss. These spatial and temporal variables depend on external drivers. The average annual soil loss (A) at a given location is estimated in ton/hectare/year using the RUSLE model **Eq 4.8** (Avand et al., 2023):

$$A = R \times K \times LS \times C \times P \quad \text{..... (4.8)}$$

where, R = rainfall erosivity expressed in (MJ mm $ha^{-1}$ $h^{-1}$ $yr^{-1}$); K = soil erodibility expressed in (t. ha. h. $MJ^{-1}$. $mm^{-1}$ . $ha^{-1}$); LS is the slope length and gradient; C is the cover management practice; and P is the conservation support or erosion control practices.

## 4.4 Model Evaluation and Performance Analysis

Evaluating ML model's performance is essential to ensure their reliability and predictive accuracy. Common evaluation methods include Kappa statistics, Receiver Operating Characteristic (ROC) curves and confusion matrices. These techniques provide quantitative measures of model performance, helping to distinguish between correct predictions and misclassifications.

A confusion matrix summarizes prediction results by comparing model outputs against reference data. It consists of four key elements: True Positives (Cases correctly predicted as occurrence), True Negatives (Cases correctly predicted as non-occurrence), False Positives (Non- occurrence incorrectly classified as occurrence) and False Negatives (occurrence missed by the model). From these values, statistical measures were obtained (**Eq 4.9**) (Acharya, 2018; Singh et al., 2024). The model deemed to be excellent if these values are close to 1– 0.9, good if < 0.9 – 0.8, medium if < 0.8– 0.7, sufficient if < 0.7– 0.6, not acceptable if < 0.5 (Hammad Khaliq et al., 2023).

$$\begin{cases} \text{Accuracy} = \frac{\text{TP+TN}}{\text{TP+FP+TN+FN}} \\ \text{Precision} = \frac{\text{TP}}{\text{TP+FP}} \\ \text{Recall} = \frac{\text{TP}}{\text{TP+FN}} \\ \text{F1} - \text{Score} = 2 \times \frac{\text{precision} \times \text{Recall}}{\text{Precision+Recall}} \\ \text{Sensitivity} = \frac{\text{TP}}{\text{TP+FN}} \\ \text{Specificity} = \frac{\text{TN}}{\text{TN+FP}} \end{cases} \quad \text{......} \quad (4.9)$$

where, TP =true positive, FP = false positive, TN = true negative, FN = false negative

The Area under the Receiver operating curve (AU-ROC) curve measures model discrimination ability by plotting the 'Sensitivity' against the '1 – Specificity'. The AUC quantifies overall performance with a value > 0.7 indicating validity of the model (Acharya, 2018; Z. Chen et al., 2019).

Kappa statistics (k) measures agreement between model predictions and ground truth (**Eq 4.10**), adjusting for chance agreement (Acharya, 2018).

$$\kappa = \frac{P_O - P_e}{1 - P_e} \quad \text{......} \quad (4.10)$$

where, $P_O = \frac{TP+TN}{n}$ (observed agreement) and $P_e = \frac{(TN+FN)(TN+FP)+(FP+TP)(FN+TP)}{n^2}$ (expected random agreement).

Kappa values between 0.61 and 0.81 indicate substantial agreement, whereas values above 0.81 reflect almost perfect reliability (Landis & Koch, 1977). Further, the results validated with field survey data.

## 4.5 Integrating Landslide, Flood and Soil Erosion for Multi Hazard Assessment

Cascading hazards occur when multiple natural hazards interact either simultaneously or sequentially, resulting in amplified impacts compared to individual events. In this study, landslide, flood, and soil erosion susceptibility maps were integrated to evaluate cascading hazard conditions within the study area. Individual susceptibility maps were initially

generated using appropriate modeling techniques and subsequently standardized into raster format with consistent spatial resolution, projection, and extent to ensure comparability and integration. To standardize the datasets, each susceptibility map was reclassified into four categories: low, moderate, high, and very high using the Natural Breaks (Jenks) classification method in GIS environment, assigning ordinal values from 1 to 4 (with higher values indicate greater susceptibility). Several integration approaches exist; however, the weighted overlay method was adopted due to its simplicity and widespread application in multiple hazard assessments (Chauhan et al., 2025; Skilodimou et al., 2019). The relative importance of each hazard (weight) was determined using AHP algorithm given by Thomas L. Saaty, 1977, and the Multi-Hazard Index (MHI) was derived using a weighted linear combination of the three hazard layers **(Eq 4.11)**.

$$\text{MHI} = \sum_{i=1}^{n} w_i H_i \quad \text{……………………………………………} \quad (4.11)$$

where, $n$ represents the number of hazards considered, $H_i$denotes the susceptibility value of hazard $i$, and $W_i$ represents the corresponding weight.

Further it is important to assess the robustness of the initial weights of different hazard determined using AHP through sensitivity analysis by testing alternative scenarios, such as equal weighting or hazard-dominant conditions, as variations in weighting schemes can influence the spatial distribution of multi-hazard hotspots. While some high-risk zones may remain consistent indicating model reliability others may shift depending on the relative emphasis assigned to each hazard. **Algorithm 3** describes how to combine multiple hazard layers into a single, uncertainty-aware risk measure using a Monte Carlo approach. It starts by loading spatial datasets for soil erosion (S), flood hazard (F), and landslide susceptibility (L), then assigns baseline weights ($W_S$, $W_F$, $W_L$) derived from AHP. Instead of keeping these weights fixed, the method introduces uncertainty by randomly perturbing them within a defined range (± 20 %) for a large number of simulations (n). In each iteration, the weights are normalized to sum to one and used to compute a Multi-Hazard Index (MHI) as a weighted sum of the three hazards. The algorithm accumulates the MHI values and their squares to later compute statistics such as the mean and standard deviation, and it also counts how often MHI exceeds a chosen threshold. After all simulations, it produces outputs including

the average hazard level, variability, and a probability map showing how likely each location is to exceed the threshold. Overall, the approach provides a more robust and realistic assessment of hazard by explicitly accounting for uncertainty in the weighting of different risk factors.

*Algorithm 3 – Multi - Hazard Integration using Monte Carlo Simulation*

1. Load raster datasets of individual hazards: Soil erosion (S), Flood hazard (F) and Landslide susceptibility (L)
2. Define base weights: $W_S$, $W_F$, $W_L$
3. Set Monte Carlo parameters: Number of simulations (n) and Uncertainty range (± 20 %)
4. Initialize accumulation variable: Sum_MHI = 0, Sum_MHI$^2$ = 0, Count_exceedance = 0
5. For i = 1 to n simulations, randomly perturb weights within uncertainty range and Normalize weights so that $W_S + W_F + W_L = 1$ and Compute Multi-Hazard Index: MHI = $(W_S \times S) + (W_F \times F) + (W_L \times L)$
6. Update accumulators: Sum_MHI = Sum_MHI + MHI, Sum_MHI$^2$ = Sum_MHI$^2$ + MHI$^2$ and If MHI > threshold → Count_exceedance = Count_exceedance + 1
7. Compute final outputs:
    - Mean MHI = Sum_MHI / n
    - Standard deviation = sqrt ((Sum_MHI$^2$ / n) − (Mean MHI) $^2$)
    - Variance = Standard deviation / mean
    - Probability map = Count exceedance / n

Moreover, the current approach assumes independence among hazards and does not explicitly account for their interactions. In reality, cascading processes such as landslides blocking river channels and triggering downstream flooding, or soil erosion contributing to slope instability and increasing landslide susceptibility, are common in mountainous environments. The omission of such interactions may lead to underestimation of risk in

certain areas; therefore, incorporating hazard interdependencies in future studies would enhance the accuracy and realism of multi-hazard assessments.

### 4.6 Multi Hazard Vulnerability and Risk Assessment

Assessing vulnerability requires consideration of material, community, and economic aspects (Rahman et al., 2022; Ram & Gupta, 2022; Sharma et al., 2025; Wang et al., 2021). The vulnerability assessment mainly focuses on the disaster-bearing system, including exposed elements such as people, property, resources, and the environment (Wang et al., 2021). It is typically quantified on a scale ranging from 0 (no loss) to 1 (complete loss). Based on multi-dimensional vulnerability frameworks (Ram & Gupta, 2022; Wang et al., 2021), this study constructs a multi hazard vulnerability assessment from physical and community perspectives. Physical vulnerability (PV) quantified through exposure of key infrastructures - roads (transport accessibility), buildings (property concentration). Community vulnerability (CV) considers ward wise population density in the Basin, reflecting societal exposure and potential for human loss. Considering the two components equally important, each weighed 0.5; vulnerability (V) of the disaster-bearing body can be expressed as:

$$V = PV + CV \quad (4.12)$$

Risk (R) refers to the expected loss of life, property, and socio-economic activities due to hazard events within a given area and time period (Sharma et al., 2025). Quantitatively, it is expressed as:

$$R = H \times V \quad (4.13)$$

where, 'H' captures the probability and intensity of hazard events and 'V' quantifies the exposure and susceptibility of elements at risk.

### 4.7 Tools and Software

This study utilized two main categories of software: (1) ArcGIS software (10.8 v) for spatial data preparation, analysis, and visualization, and (2) Jupyter Notebook platform with Python (3.10 v) for data processing and machine learning implementation.

Various Python libraries employed include:

- NumPy: numerical computing, data manipulation, and linear algebra operations
- Pandas: handling and analyzing tabular datasets and matrices
- Rasterio: reading and processing geospatial raster data
- Scikit-learn: A machine learning library used for classification, regression, model training, and performance evaluation.
- Geopandas: handling vector data inform of shapefile
- These tools collectively supported spatial analysis, data preprocessing, and predictive modeling for hazard assessment.

# 5 Results & Discussion

## 5.1 Landslide Susceptibility Assessment

### *5.1.1 Landslide Susceptibility Zonation*

The Support Vector Classification (SVC) model was trained using the prepared training dataset. Model hyperparameters were optimized using a grid search approach coupled with 5-fold cross-validation to ensure robust and reliable parameter selection. The optimized parameters included a penalty parameter C = 10, a kernel coefficient gamma = 1, and the radial basis function (RBF) as the best-performing kernel (**Table 5-1**). This optimized setup enhanced the model's capability to effectively capture complex non-linear relationships between conditioning factors and landslide occurrence.

*Table 5-1: Hyperparameter Optimization for SVM model*

| **Hyperparameters** | **Optimized Hyperparameters** | **Significance** |
|---|---|---|
| 'C': [0.01, 0.1, 1, 10, 100] | C = 10 | Regularization |
| 'gamma': [0.1, 0.25, 0.5, 0.75, 1] | gamma = 1 | Kernel coefficient |
| 'kernel': ['poly', 'rbf', 'sigmoid'] | Kernel = rbf | |

The trained model then applied to predict the probability of landslide occurrence for each pixel within study area and the probability values used as a susceptibility index to generate the landslide susceptibility map (LSM) within a GIS environment. The resulting map was further classified into four categories representing varying levels of susceptibility, from very low to very high. This classification was performed using the natural breaks method in GIS, and the spatial distribution of landslide susceptibility was visualized using a color gradient, where green tones denote areas of very low susceptibility and dark red represents zones of very high susceptibility (**Figure 5-1**).

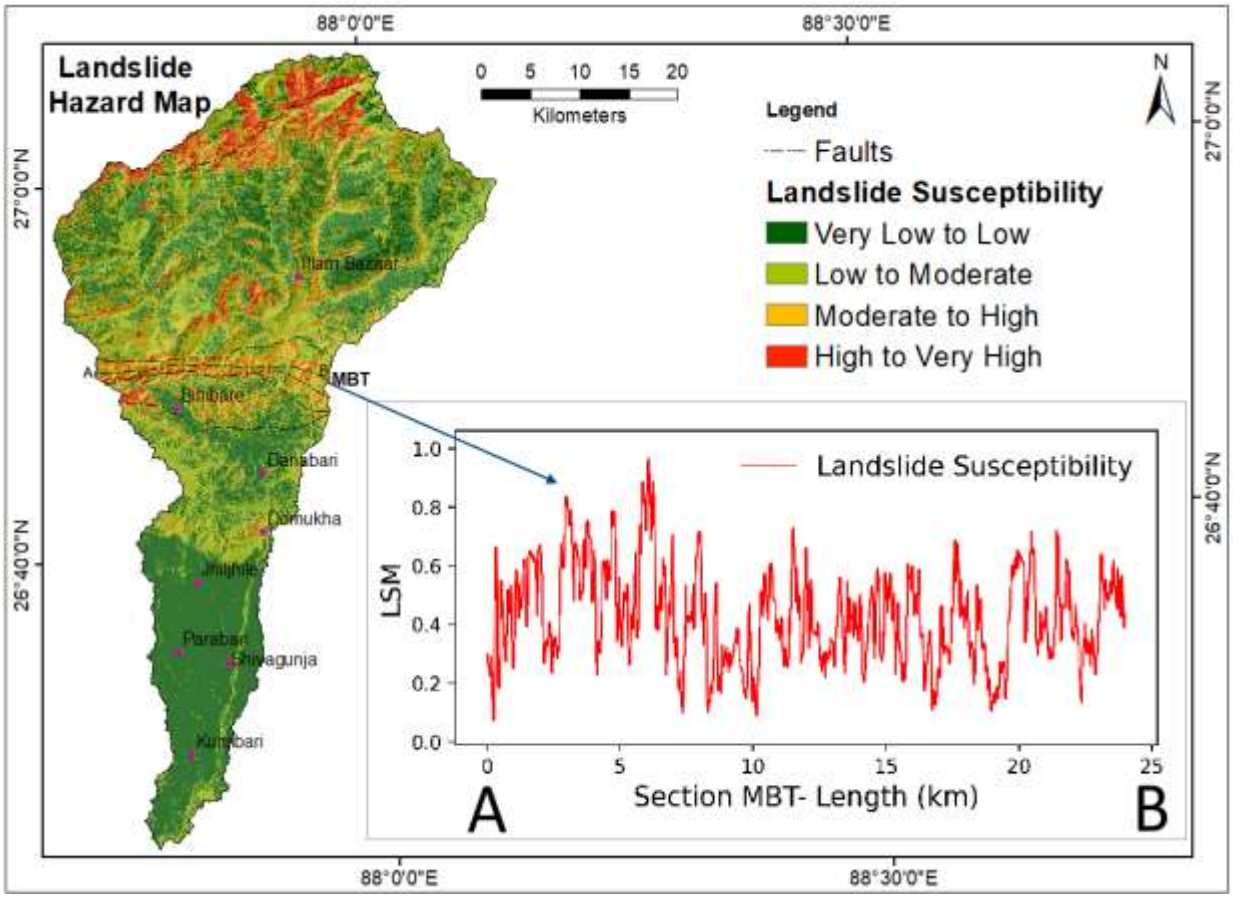


*Figure 5-1: Landslide susceptibility map of kankai basin*

The distribution of landslide susceptibility pattern revealed that 3.75 % of the study area falls within high to very high risk, while 7.60 % is categorized as moderate to high and 24.96 % as low to moderate susceptibility. A majority of the basin area (63.69 %), particularly in the flat, alluvial southern Terai basin, is classified within the very low landslide potential zone. Higher susceptibility zones are mainly concentrated in steep mountainous areas, especially along drainage channels and hill road corridors. In contrast, lower susceptibility areas are predominantly located in valley floors and relatively flat terrain. This distribution suggests that the northern part of the Basin, with its steep rugged landscape, complex geology, dense drainage and road networks, is more vulnerable to landslides. In addition, areas along the Main Boundary Thrust (MBT) are particularly susceptible (**Figure 5-1**) due to geological instability, steep slopes, and intense rainfall, which collectively enhance slope failure potential.

*5.1.2 Contribution of Landslide Conditioning Factors*

Multicollinearity among the landslide conditioning variables incorporated in the susceptibility model was assessed using Variance Inflation Factor (VIF) analysis as shown in **Figure 5-2**.

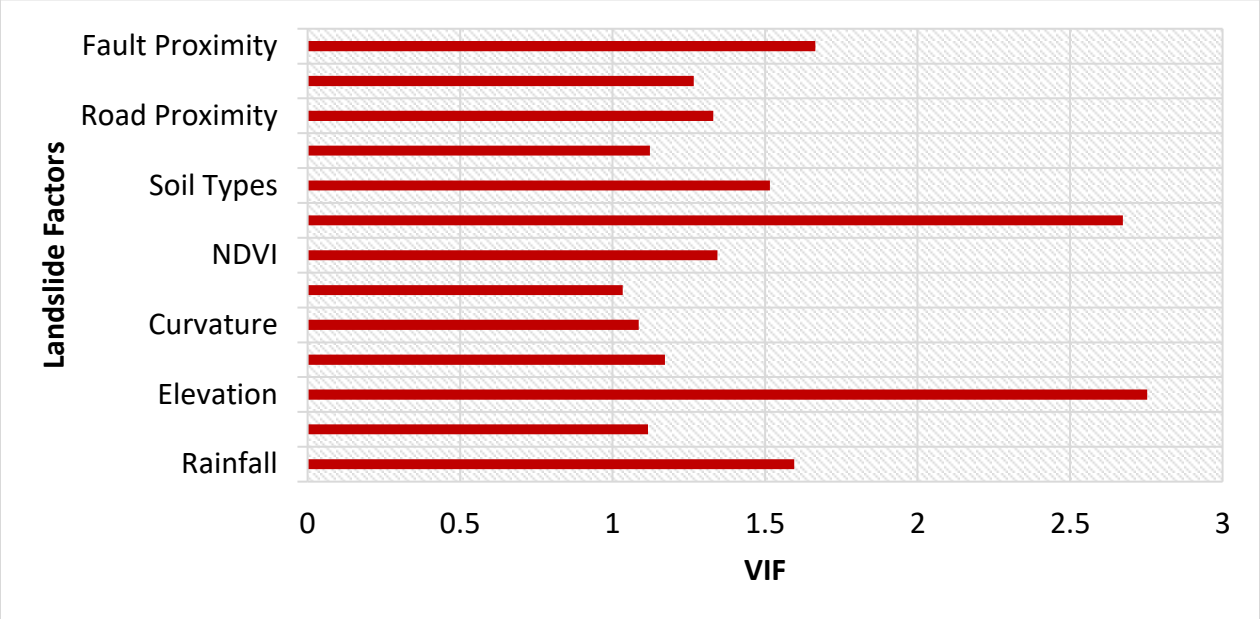


*Figure 5-2: Variance Inflation Factor for landslide predictors*

Multicollinearity can reduce model effectiveness by increasing the variance of regression coefficients and compromising the reliability of variable importances. The VIF analysis reveals that all predictor variables have values well below the commonly accepted threshold of 5, indicating the absence of serious multicollinearity among the selected factors. Elevation and geology exhibit comparatively higher VIF values than the other variables, suggesting a moderate level of association with related topographic and environmental parameters. However, these values remain within acceptable limits and therefore do not compromise model stability.

Other variables, including rainfall, soil type, NDVI, slope, and river proximity, demonstrate moderate VIF values, reflecting some degree of interdependence, which is typical in environmental and terrain-based analyses. In contrast, factors such as fault proximity, Land Use Land Cover (LULC), Curvature, and Topographic Wetness Index (TWI) having VIF values

around 1, indicating minimal correlation with other predictors. This suggests the selected variables provide largely independent information and strengthen the overall robustness of the model.

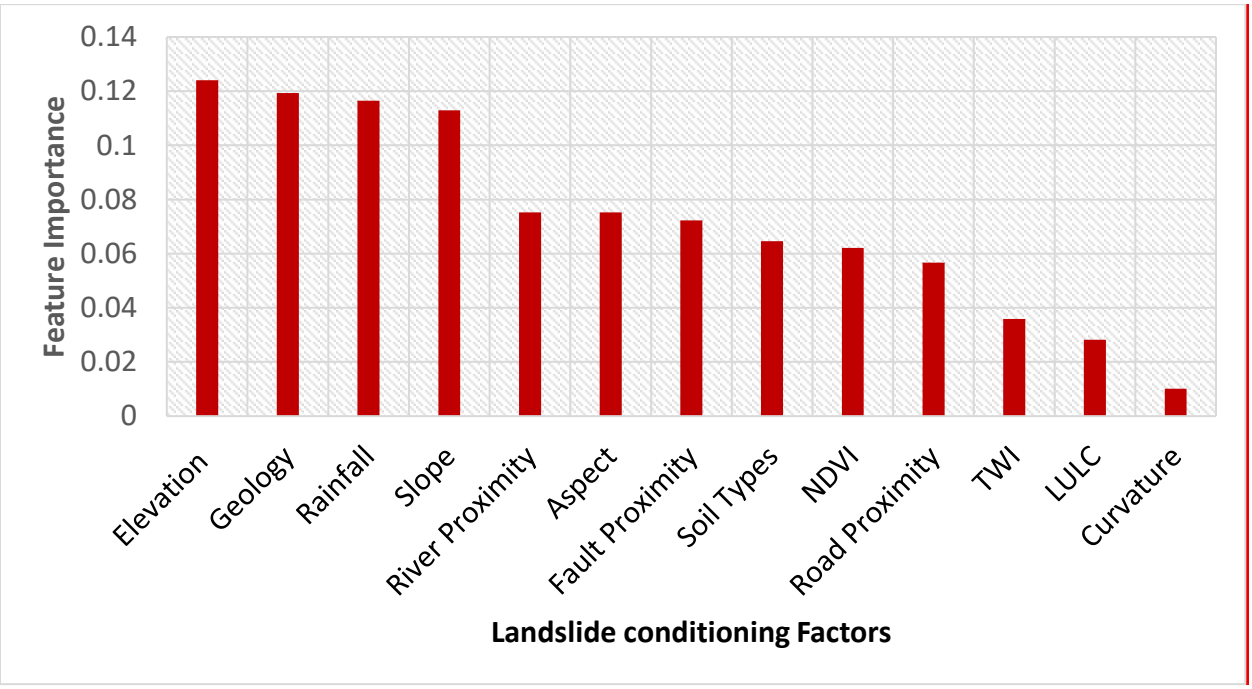


*Figure 5-3: Permutation feature importance for landslide predictors*

Overall, the VIF analysis verifies that the chosen landslide conditioning factors are statistically independent and appropriate for incorporation into the model. The absence of significant multi collinearity enhances the consistency and robustness of the model results and ensures that each variable contributes meaningfully to the prediction of landslide susceptibility.

The permutation feature importance analysis **(Figure 5-3)** was used to evaluate the relative contribution of landslide conditioning factors in the susceptibility model. The results indicate that elevation is the most influential variable, with the highest importance value, suggesting topography strongly controls landslide occurrence in the area. Geology, rainfall, and slope are also highly significant factors, Moderate importance is observed for river proximity, NDVI, road proximity, aspect, fault proximity, and soil types, also contribute to landslide susceptibility. In contrast, Topographic Wetness Index (TWI), Land Use Land Cover

(LULC), and Curvature show relatively low importance values, suggesting a limited influence on the model prediction. Overall, the results highlight that topographic, geological, and climate-related factors play a dominant role in controlling landslide occurrence, while land cover and terrain curvature have comparatively smaller contributions in the region.

### *5.1.3 Validation of Landslide Susceptibility Model*

The performance of the model was assessed using the Area Under the Receiver Operating Characteristic curve (AU–ROC), Kappa statistics, and a confusion matrix within a Python environment using the Scikit-learn library. The ROC curve is a widely used evaluation tool that illustrates the relationship between the true positive and the false positive data. In this context, a true positive refers to locations where the model correctly identifies the presence of landslides in areas that are actually landslide-prone, while a false positive occurs when the model incorrectly classifies a stable area as susceptible to landslides. The AUC value, ranging from 0 to 1, provides an overall measure of model performance, where values above 0.5 indicate that the model performs better than random prediction and model validity. A higher AUC reflects greater predictive accuracy and stronger classification capability.

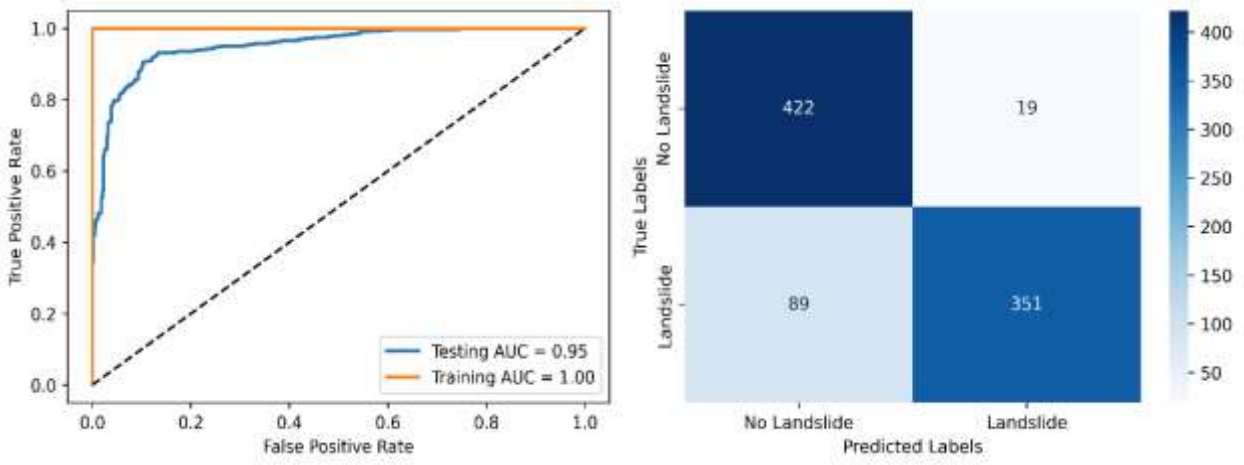


*Figure 5-4: Receiver Operating Characteristics curve and confusion matrix for SVM model for landslide susceptibility*

*Table 5-2: Classification report of SVM model for landslide*

| Class | precision | recall | f1-score | SVM Accuracy | Cohen's Kappa Score |
|---|---|---|---|---|---|
| 0 | 0.83 | 0.96 | 0.89 | 0.877 | 0.755 |
| 1 | 0.95 | 0.80 | 0.87 | | |

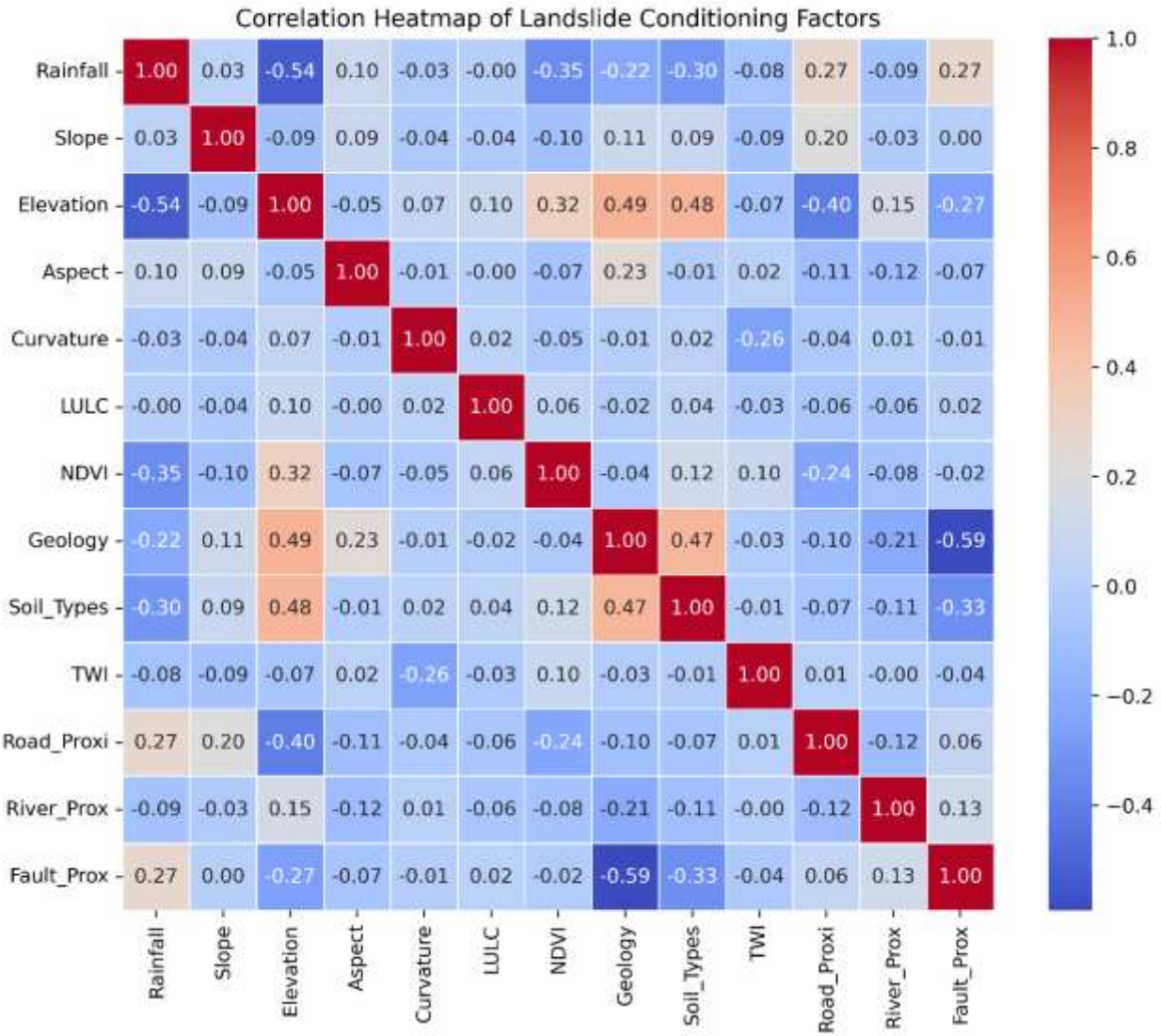


*Figure 5-5: Correlation Heatmap for Landslide Conditioning Factors*

In this study, the landslide susceptibility model achieved an AUC value of 95 % **(Table 5-2)**, indicating excellent predictive performance and a high level of reliability in distinguishing

between landslide-prone and non–landslide-prone areas. **(Figure 5-4)** presents the receiver operating characteristics curve along with confusion matrix of the model. The confusion matrix revealed a high number of true negatives (422) and true positives (351), indicating that the model performs well in correctly identifying both stable and landslide-prone areas. However, the presence of false negatives (89) suggests that a portion of actual landslide-prone locations were not detected by the model, which is a commonly observed limitation in landslide susceptibility assessments. On the other hand, the low number of false positives (19) indicates that the model rarely classifies stable areas as susceptible to landslides, reflecting good classification precision.

Overall, the SVM model achieved an accuracy of 0.877, indicating a high proportion of correctly classified instances. In addition, the Cohen's Kappa score of 0.755 suggests substantial agreement between the predicted and observed classes, confirming that the model performs reliably beyond chance level classification. Further, the correlation heat map of landslide factors illustrates strength and direction of relationships among the variables used in the landslide susceptibility model (**Figure 5-5).** The correlation values range from -1 to +1, where positive values indicate a direct relationship between variables and negative values represent an inverse relationship. Overall, the heat map suggests that the conditioning factors are largely independent of one another, with only a few showing moderate levels of correlation. This indicates that there is minimal redundancy among the selected variables, making them appropriate for inclusion in the landslide susceptibility modeling without significantly affecting model reliability.

## 5.2 Flood Susceptibility Assessment

### *5.2.1 Flood Susceptibility Zonation*

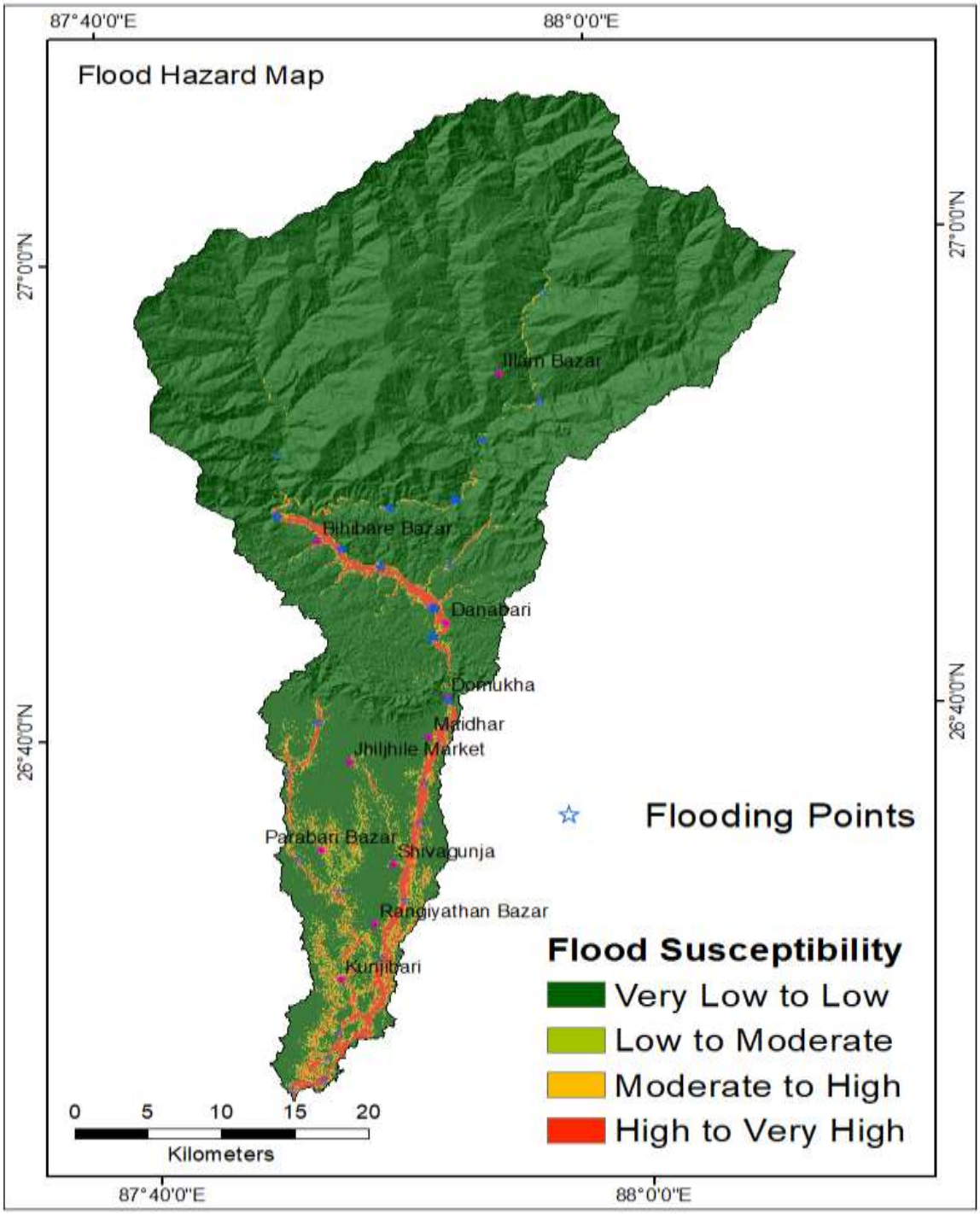


*Figure 5-6: Flood susceptibility map of Kankai Basin*

The Support Vector Classification (SVC) model was trained for flood hazard using the prepared training dataset, and it was then applied to estimate the probability of flood occurrence for each pixel. These probability values were used as a susceptibility index to generate the flood susceptibility map (FSM) within a GIS environment. The resulting map was further classified into four categories representing varying levels of susceptibility, from very low to very high. This classification was performed using the natural breaks method in GIS, and the spatial distribution of Flood susceptibility was visualized using a color gradient, where green tones denote areas of very low susceptibility and dark red represents zones of very high susceptibility (**Figure 5-6**).

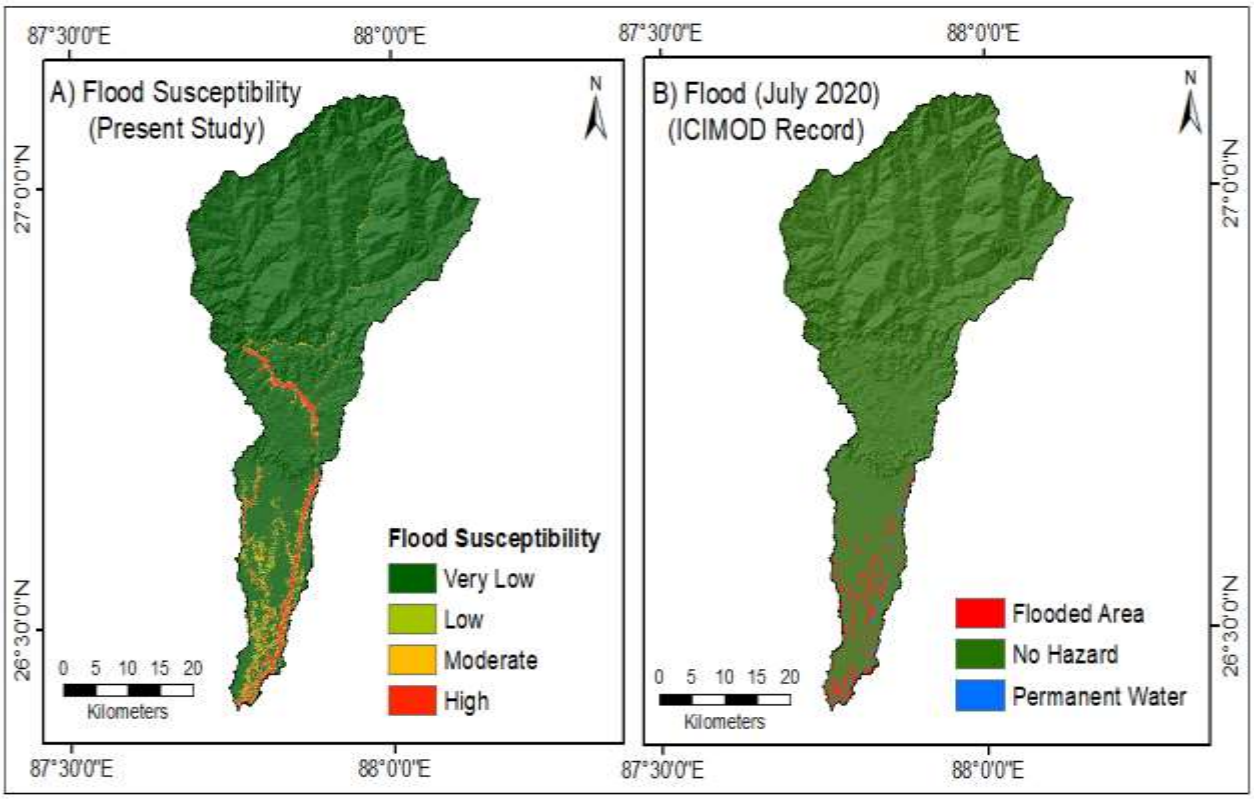


*Figure 5-7: A) Flood susceptibility map of Kankai Basin, B) Flood, July 2020 ICIMOD Record in Kankai Basin*

The flood susceptibility analysis reveals that 2.76 % of the study area is classified as high to very high risk, while 1.59 % falls under the moderate to high category and 2.48 % under low to moderate susceptibility. The majority of the basin (93.17 %), particularly the upper

catchment, exhibits very low to low flood susceptibility, mainly due to its steep mountainous terrain and efficient surface drainage.

Conversely, zones with higher flood susceptibility are mainly located in the southern Terai plain and along river networks, where, flat topography and extensive agricultural land increase exposure to inundation. This pattern clearly shows that the downstream lowland areas are considerably more vulnerable to flooding compared to the upstream hilly regions. The flood extent data from July 2020 (ICIMOD record) shown in **Figure 5-7 B** further supports this observation, confirming that the southern Terai region experiences more frequent flood events.

### *5.2.2 Influence of Flood Conditioning Factors*

Multicollinearity among the flood predictors incorporated in the susceptibility model was assessed using Variance Inflation Factor (VIF) analysis as shown in **Figure 5-8**.

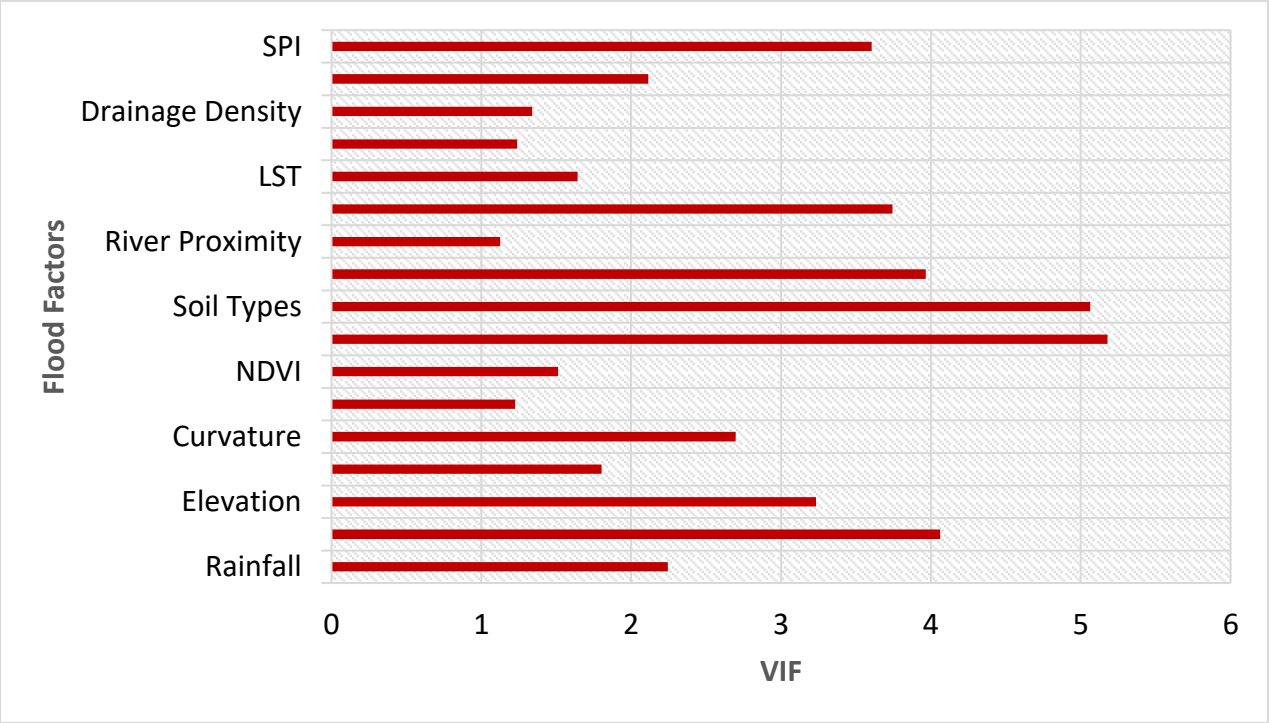


*Figure 5-8: Variance Inflation Factor for Flood Predictors*

Multi collinearity can negatively affect model performance by inflating the variance of regression coefficients and reducing the reliability of variable importance. The VIF analysis reveals that all predictor variables have values well below the commonly accepted threshold of 5, indicating the absence of serious multicollinearity among the selected factors. Among the variables, soil type and geology exhibit relatively higher VIF values compared to the other factors, indicating a moderate level of correlation with other variables. However, their values remain within the acceptable range, suggesting that their inclusion does not adversely affect the stability of the model. Other factors such as TWI, elevation, slope, show moderate VIF values, indicating a limited degree of correlation with other predictors. This is expected in environmental studies where certain terrain and climatic variables are naturally interrelated. In contrast, river proximity, land use land cover (LULC), and soil moisture display VIF values around 1, indicating very weak correlation with the other predictors. This suggests that these variables are largely independent and provide distinct information to the model without introducing redundancy. Overall, the VIF analysis confirms that the selected flood conditioning factors are statistically independent and suitable for inclusion in the susceptibility model. No significant multicollinearity enhances the robustness and consistency of the model and ensures that each variable contributes flood susceptibility.

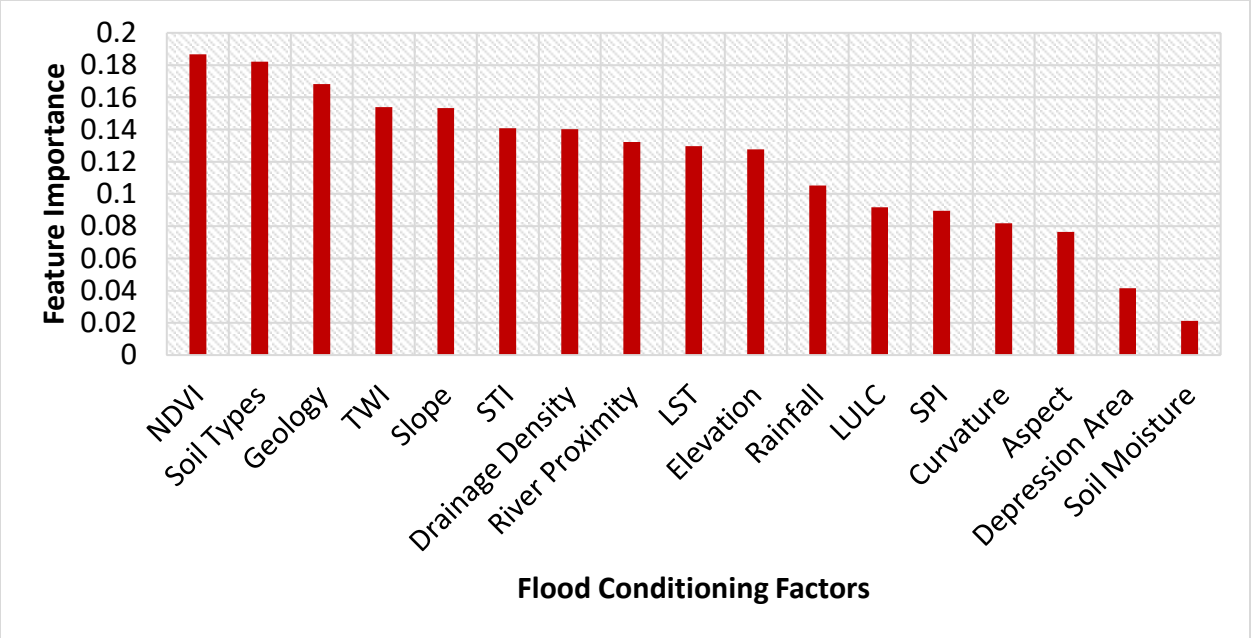


*Figure 5-9: Permutation Feature Importance for flood predictors*

The permutation feature importance analysis (**Figure 5-9**) was applied to assess the relative influence of flood predictors. The results show that NDVI is the most dominant predictor, exhibiting the highest importance value and indicating a strong control on flood occurrence in the study area. Soil type, geology, Topographic Wetness Index (TWI), and slope also emerge as highly significant variables contributing to flood susceptibility. In addition, moderate importance is observed for Land Use Land Cover (LULC), Stream Power Index (SPI), curvature, and aspect, which also play supporting roles in explaining flood distribution patterns. Overall, the results indicate that NDVI, soil type, geology, and rainfall-related factors are the key drivers influencing flood occurrence in the study area. In contrast, soil moisture shows a relatively lesser contribution to flood susceptibility.

### *5.2.3 Validation of Flood Susceptibility Model*

The performance of the model was assessed using the Area Under the Receiver Operating Characteristic curve (AU–ROC), Kappa statistics, and a confusion matrix within a Python environment using the Scikit-learn library. The ROC curve is a widely used evaluation tool that illustrates the relationship between the true positive and the false positive data. In this context, a true positive refers to locations where the model correctly identifies the presence of flood in areas that are actually flood-prone, while a false positive occurs when the model incorrectly classifies a non-flood-prone area as flood susceptible. The AUC value, ranging from 0 to 1, provides an overall measure of model performance, where values above 0.5 indicate that the model performs better than random prediction and model validity. A higher AUC reflects greater predictive accuracy and stronger classification capability.

In this study, the landslide susceptibility model achieved an AUC value of 96 % (**Table 5-3**), indicating excellent predictive performance and a high level of reliability in distinguishing between landslide-prone and non–landslide-prone areas. (**Figure 5-10**) presents the receiver operating characteristics curve along with confusion matrix of the model. The confusion matrix revealed a high number of true negatives (561) and true positives (580), indicating that the model performs well in correctly identifying both stable and flood-prone areas.

*Table 5-3: Classification report of SVM model for Flood*

| | | | | SVM | |
|---|---|---|---|---|---|
| **Class** | **Precision** | **Recall** | **F1-score** | **Accuracy** | **Cohen's Kappa Score** |
| 0 | 0.90 | 0.87 | 0.88 | 0.885 | 0.771 |
| 1 | 0.87 | 0.90 | 0.89 | | |

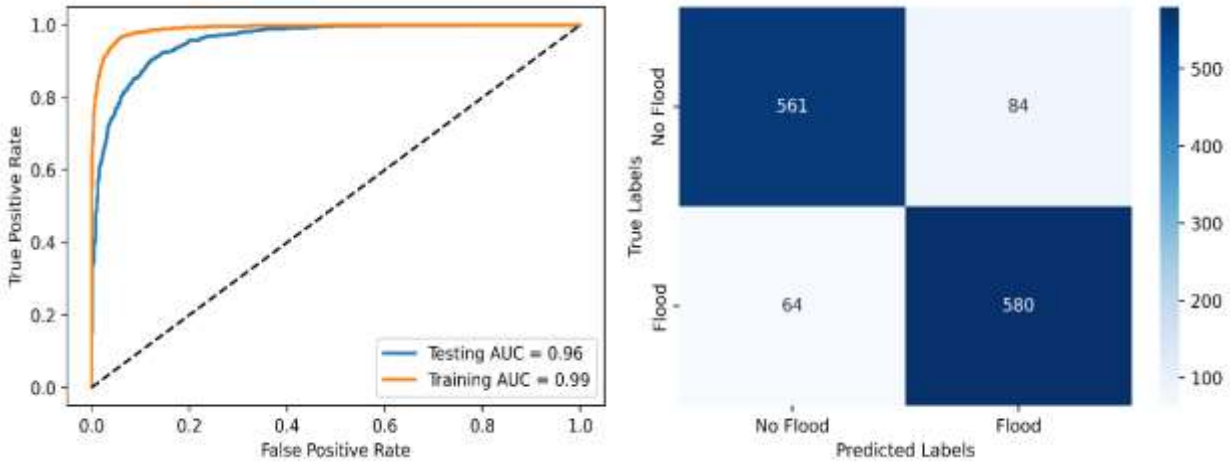


*Figure 5-10: Receiver Operating Characteristics curve and confusion matrix for SVM model for Flood susceptibility*

However, the presence of false negatives (64) suggests that a portion of actual flood prone locations were not detected by the model, which is a commonly observed limitation in flood susceptibility assessments. On the other hand, the low number of false positives (84) indicates that the model rarely classifies stable areas as susceptible to flooding, reflecting good classification precision. Overall, the SVM model achieved an accuracy of 0.885, indicating a high proportion of correctly classified instances. In addition, the Cohen's Kappa score of 0.771 suggests substantial agreement between the predicted and observed classes, confirming that the model performs reliably beyond chance level classification. Further, the correlation heat map of flood predictors illustrates strength and direction of relationships among the variables used in the landslide susceptibility model (**Figure 5-11**).

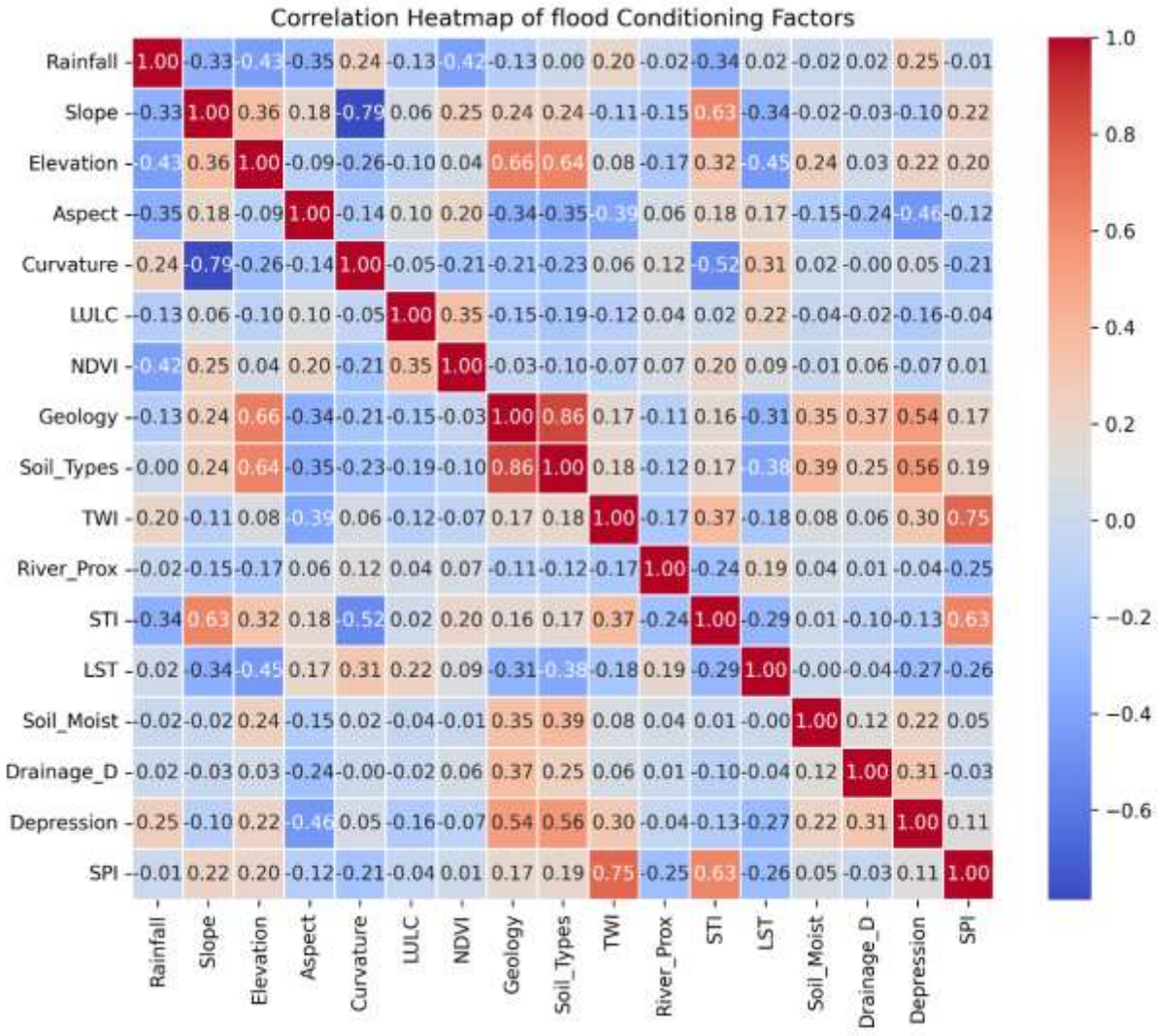


*Figure 5-11: Correlation Heatmap for Flood Conditioning Factors*

## 5.3 Soil Erosion Risk Assessment

The soil erosion risk assessment of the area was conducted using the erosion hazard classification erosion hazard map (**Figure 5-12A**). Erosion hazard is characterized by four major erosion potential classes: very low to low (3.54 %), low to moderate (51.42 %), moderate to high (43.79 %), and high to very high (1.25 %). The spatial distribution shows that the northern and north-western part of the basin are dominated by moderate to high and high to very high erosion potential zones. These areas correspond to rugged terrain and steeper slopes along the drainage and road network and its proximity where runoff

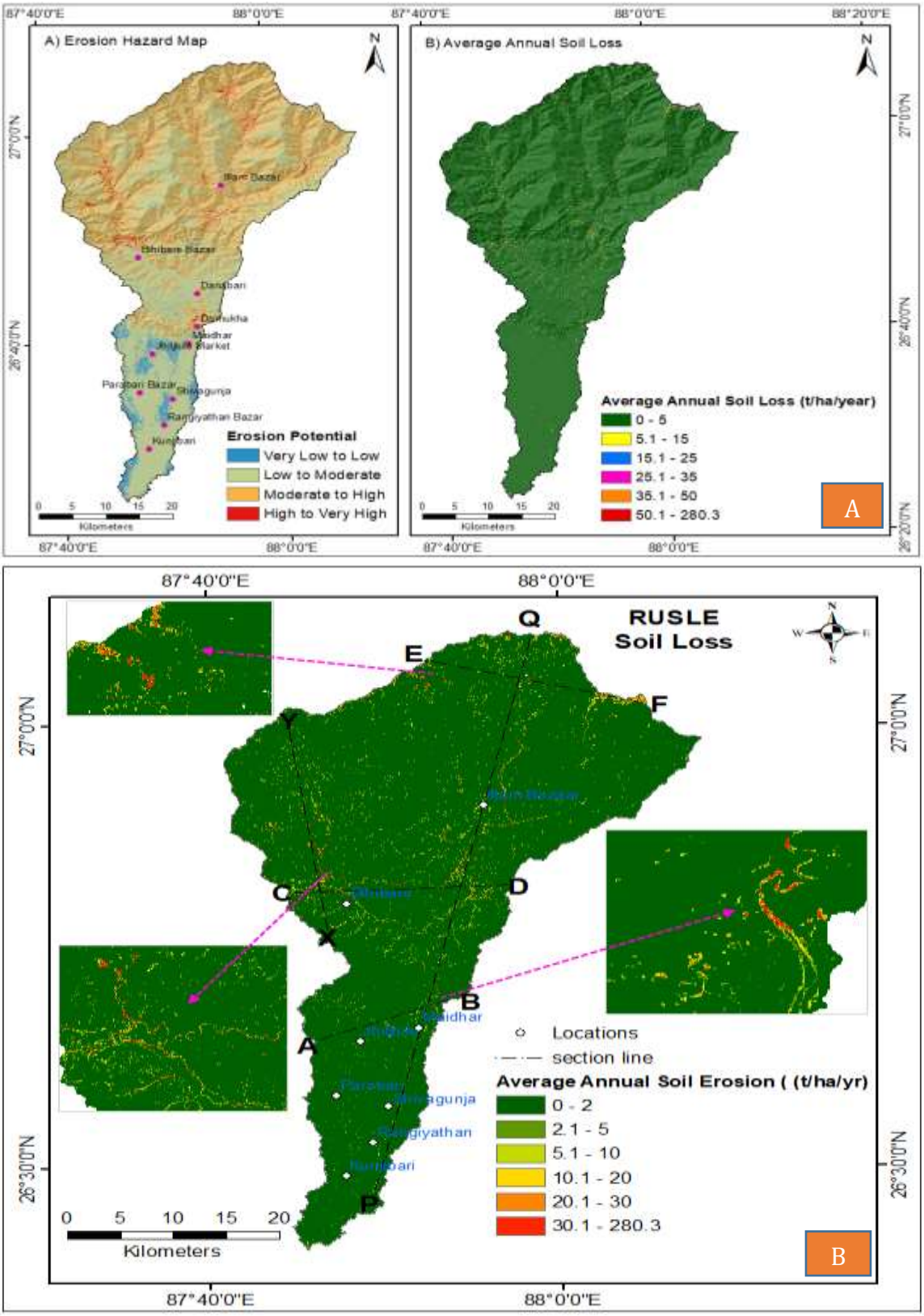


*Figure 5-12: Erosion Hazrd mapping A) Erosion Susceptibility map, B) Average annual soil loss estimation map*

velocity is comparatively higher, thereby increasing the susceptibility to soil detachment and transportation. In contrast, the central and southern parts of the watershed mainly fall within the very low to low and low to moderate erosion hazard classes. The relatively gentle slope conditions and better vegetation cover in these areas contribute to reduced soil erosion risk. hence, the analysis reveals a spatial variation in erosion susceptibility across the watershed, largely influenced by topographic characteristics, land cover conditions, and rainfall-induced runoff. The annual average soil loss map (**Figure 5-12B**) provides a quantitative estimate of soil erosion across the basin. The results indicate that the majority of the study area experiences very low soil loss rates ranging between 0 – 5 t/ha/year, suggesting relatively stable land conditions. However, some localized areas exhibit higher soil loss values ranging from 5.1–15 t/ha/year and 15.1 – 25 t/ha/year, while areas, particularly near to river banks show erosion rates exceeding 25 t/ha/year, with maximum value of 280.3 t/ha/yr. These higher erosion zones are mainly associated with steep slopes and areas are proximity to drainage network with limited vegetation protection, where rainfall impact and surface runoff contribute significantly to soil loss.

These hotspot areas are further clarified by the profiles along Section AB, CD, EF, PQ & XY (**Figure 5-13 - 5-17**). The elevation profile shows that soil loss remains minimal across gently undulating terrain in the initial segments, but increases sharply in zones characterized by abrupt elevation changes. This pattern is reinforced by the slope profile, where low-gradient areas (< 5°) correspond to negligible erosion, while steep slopes (>30°) coincide with pronounced spikes in soil loss, NDVI profile further highlights larger soil loss value at abrupt NDVI change location). Notably, the most extreme erosion peaks occur, where steep slopes and rapid elevation transitions with minimal vegetative cover likely enhance runoff velocity and sediment detachment. The combined analysis demonstrates that elevation alone does not directly control erosion intensity, the interaction of slope steepness, terrain variability and vegetative cover plays a critical role in accelerating soil loss. These findings indicate that erosion risk in the study area is highly localized and primarily controlled by topographic factors, underscoring the need for specific methods for conserving soil in steep and geomorphologically unstable zones rather than uniform interventions across the landscape.

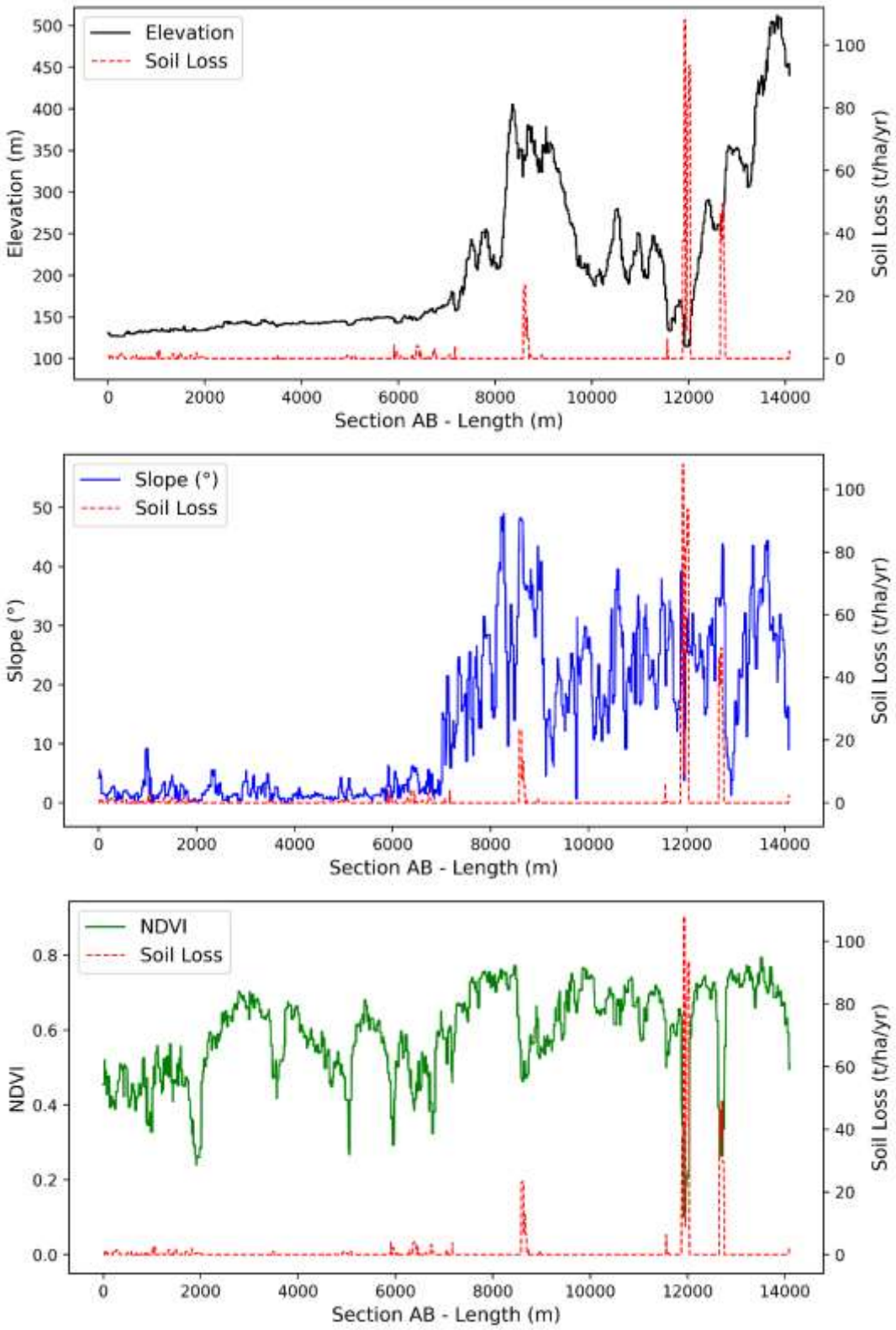


*Figure 5-13: Cross Sectional profile of soil erosion at AB– Elevation, Slope and NDVI vs Soil loss plot*

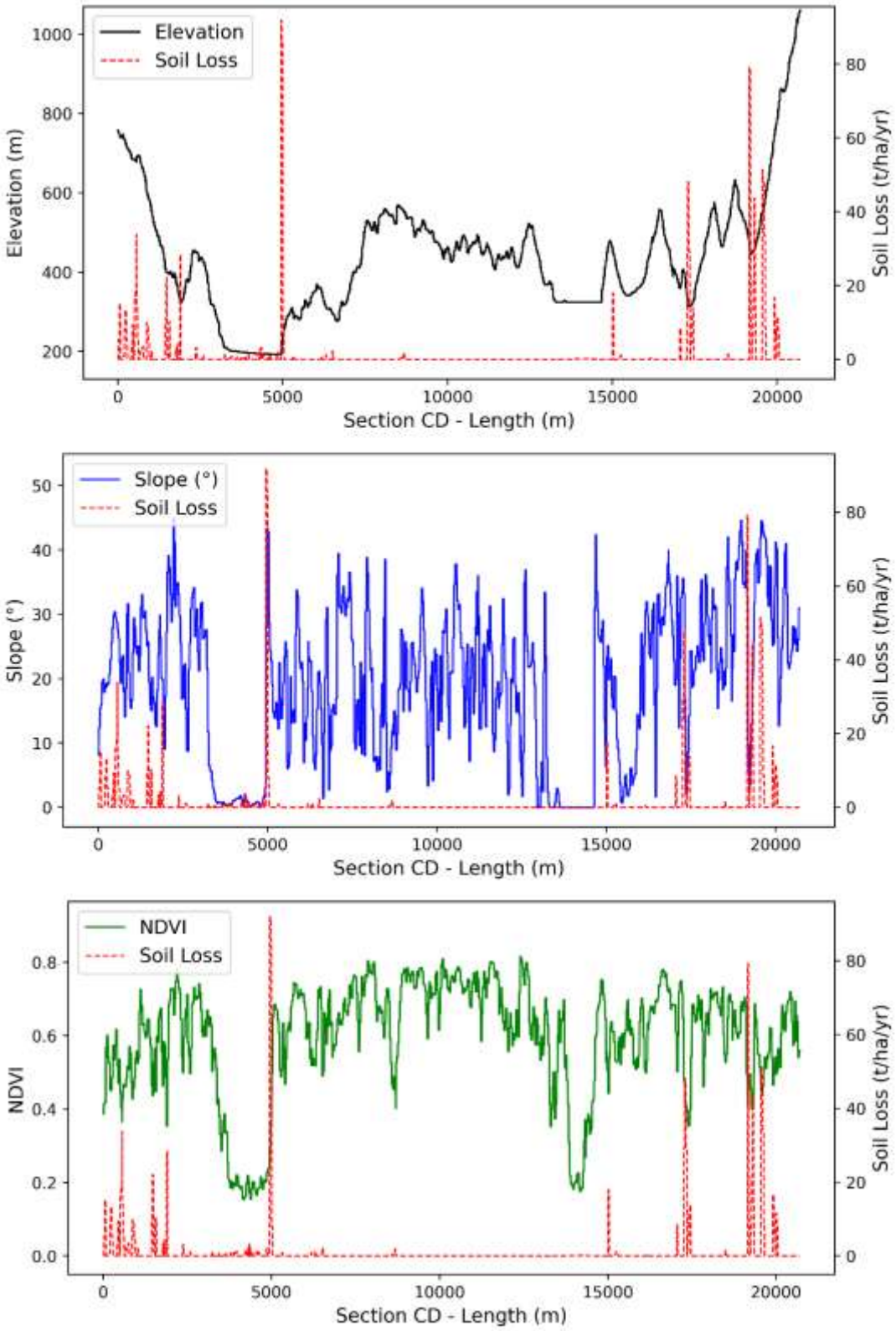


*Figure 5-14: Cross Sectional profile of soil erosion at CD – Elevation, Slope and NDVI vs Soil loss plot*

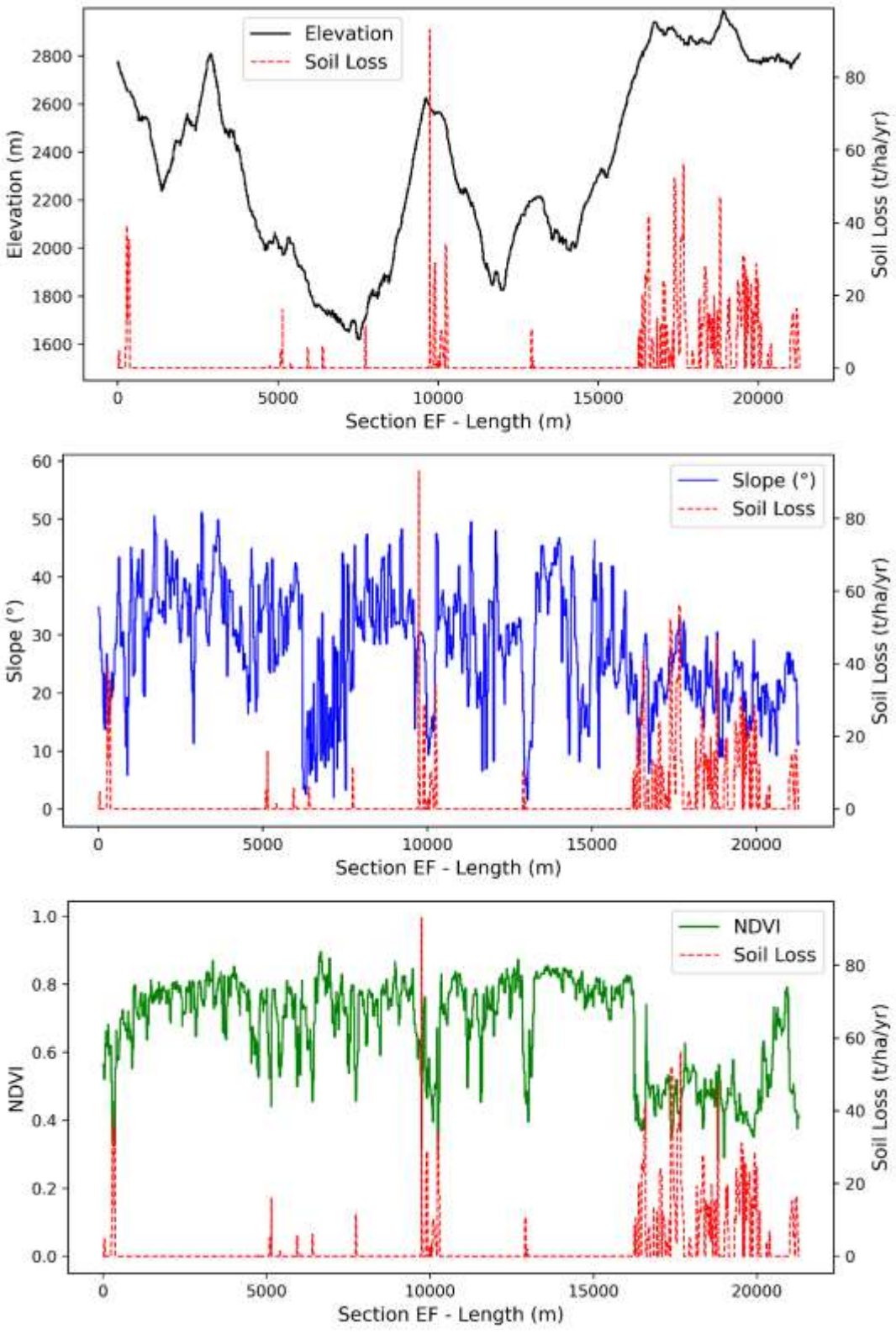


*Figure 5-15: Cross Sectional profile of soil erosion at EF – Elevation, Slope and NDVI vs Soil loss plot*

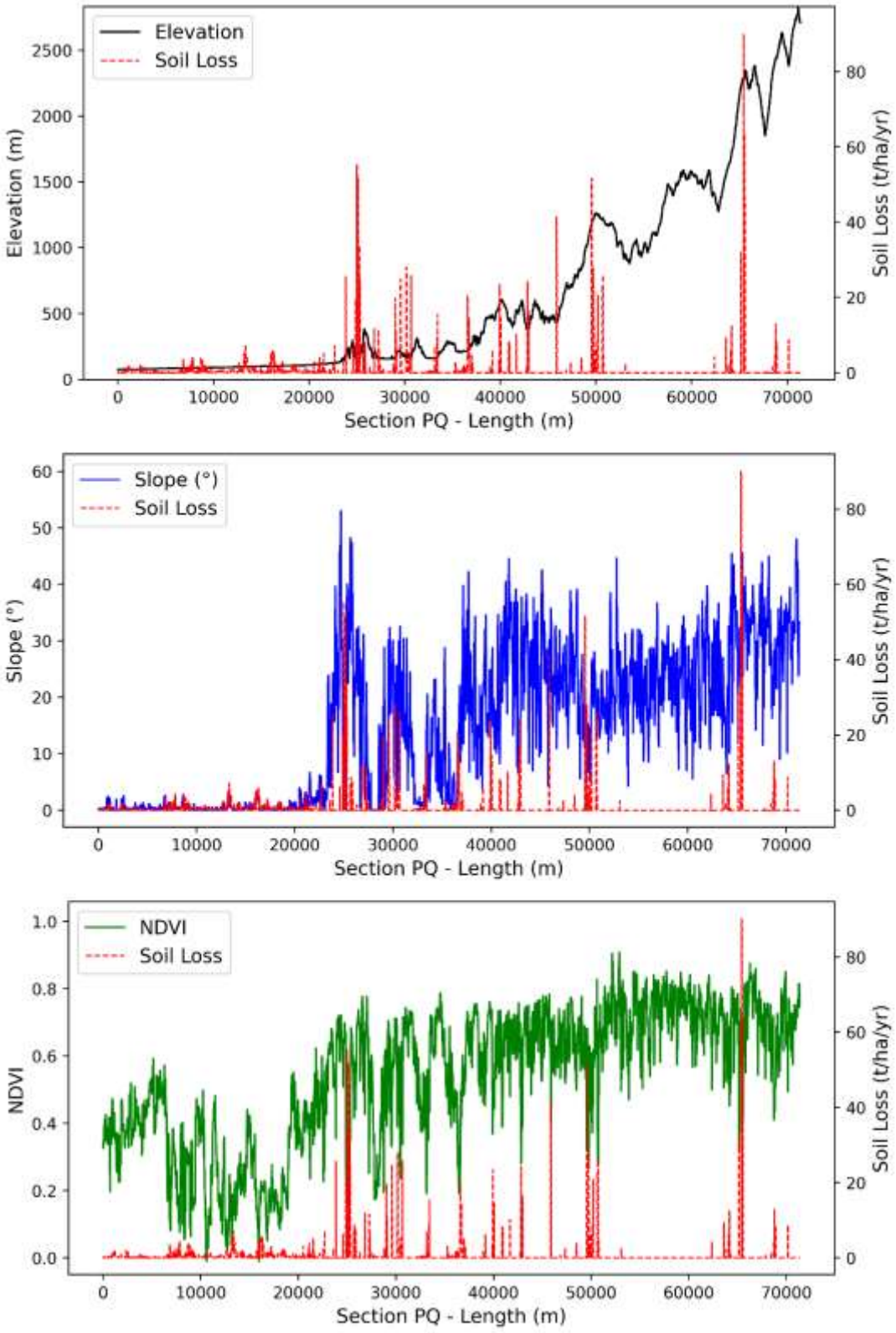


*Figure 5-16: Cross Sectional profile of soil erosion at PQ – Elevation, Slope and NDVI vs Soil loss plot*

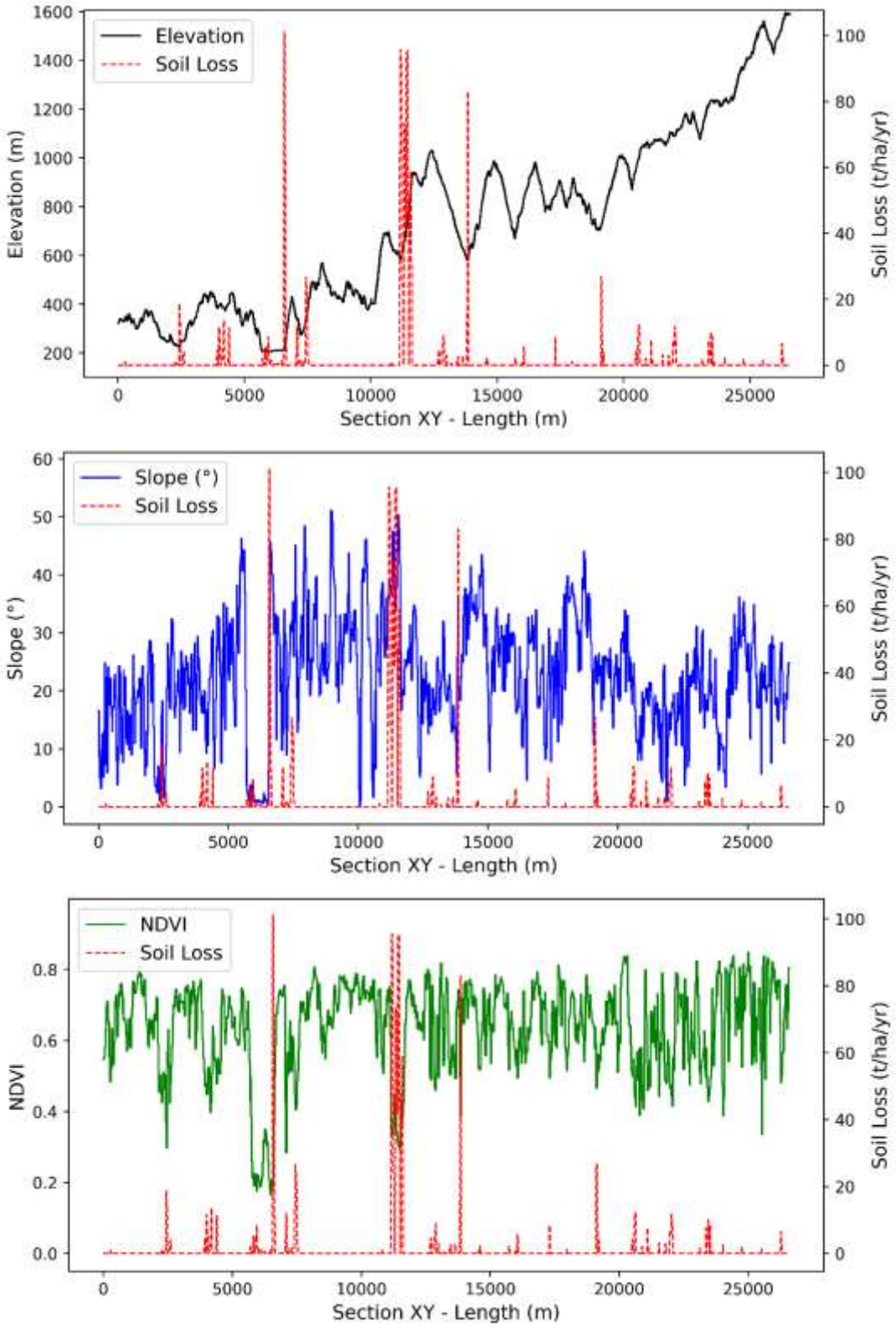


*Figure 5-17: Cross Sectional profile of soil erosion at XY – Elevation, Slope and NDVI vs Soil loss plot*

## 5.4 Integrated Cascading Hazard Assessment

This study presents an integrated multi-hazard framework combining machine learning, geospatial analysis, and Monte Carlo simulation incorporating AHP weights. A Support Vector Machine was applied to evaluate landslide susceptibility, using a multi-temporal inventory of 842 polygons and 13 conditioning factors including topography, lithology, rainfall, soil, land use, and proximity to roads, rivers, and faults. Similarly, flood susceptibility modeled using 2147 pixels (30 m resolution) of historical flood locations and 17 influencing factors in SVC framework. Soil erosion was estimated through a weighted overlay of six geomorphic and hydrological indicators, complemented by RUSLE calculations. A multi-hazard exposure map was then generated using a weighted overlay approach, with weights were first assigned using AHP and then tested with Monte-Carlo simulations to reduce uncertainty. A multi-hazard map was initially produced **(Figure 5-18A)** using a weighted overlay approach, assigning relative contributions of 44% (landslides), 39% (floods), and 17% (soil erosion) based on AHP weights **(Table 5-4).** However, this deterministic framework does not account for uncertainty in weight selection.

*Table 5-4: Pair-wise comparisons, weighting coefficients for multi-hazard evaluation*

| Hazards | Landslide | Flood | Erosion | Weight |
|---|---|---|---|---|
| Landslide | 1 | 1 | 3 | 0.44 |
| Flood | 1 | 1 | 2 | 0.39 |
| Soil Erosion | 1/3 | 1/2 | 1 | 0.17 |
| CR = 0.021 < 0.05 | | | | |

To address this, a Monte Carlo–based method was implemented to derive an uncertainty-aware composite risk metric. Spatial layers for soil erosion (S), flood hazard (F), and landslide susceptibility (L) were combined using baseline AHP weights ($W_S$, $W_F$, $W_L$). Weight uncertainty was incorporated by perturbing each weight within ± 20 % across number of simulations. In each iteration, perturbed weights were normalized to sum to unity and used

to compute the Multi-Hazard Index (MHI) as a weighted linear combination of the hazard layers.

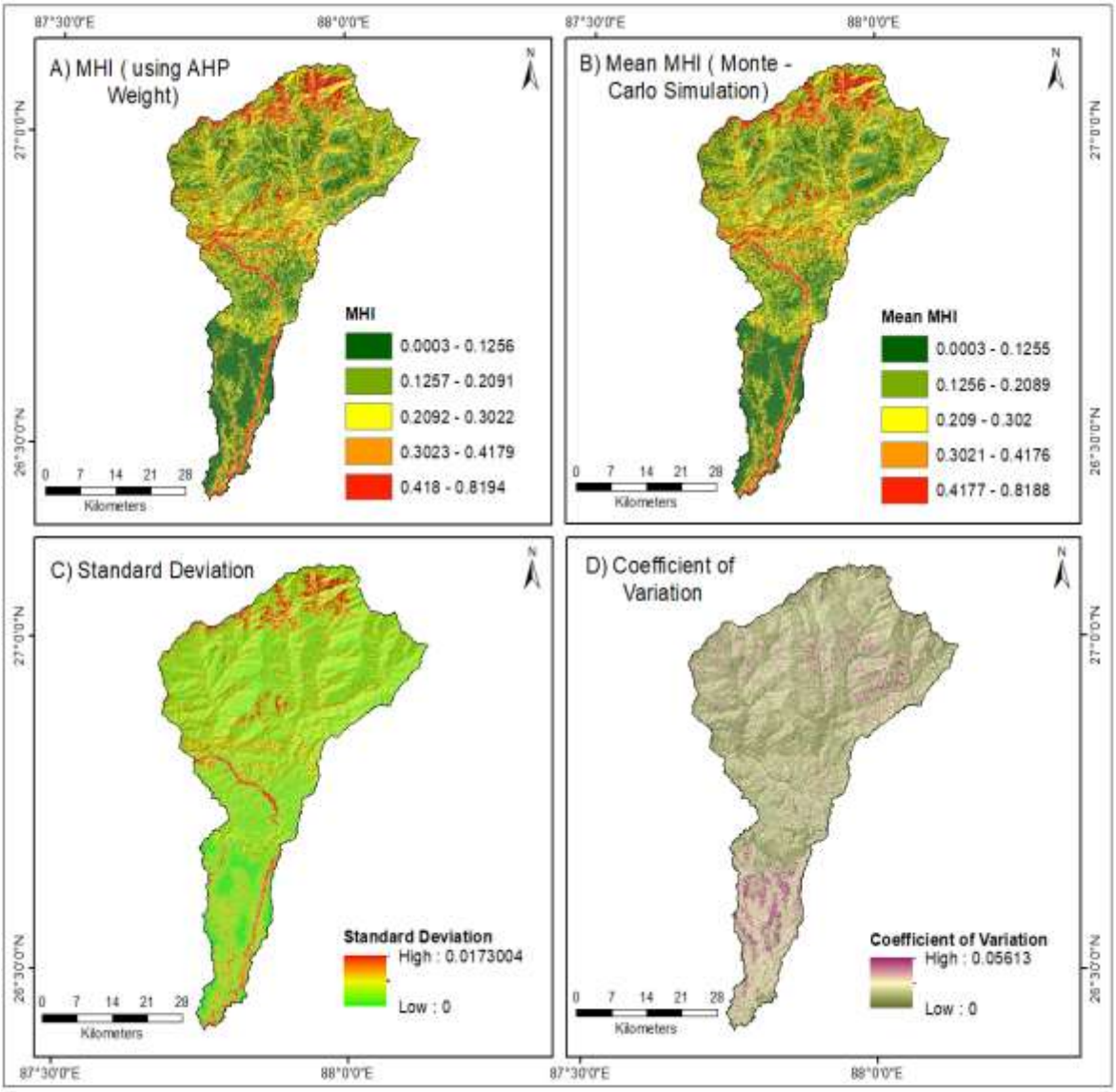


*Figure 5-18: Local Level wise Multi Hazard Suseptibility Assessment of Kankai Basin ( A) MHI,using AHP, ( B) Mean MHI , Monte- Carlo Simulation, (C) Standard Deviation, (D) Cofficient of Variation*

The simulation framework accumulates MHI values and their squares to estimate the mean and standard deviation, while also recording exceedance frequencies relative to a predefined threshold. Final outputs include maps of mean hazard intensity **(Figure 5-18B)**, standard deviation **(Figure 5-18C)**, coefficient of variation **(Figure 5-18D)**. This probabilistic

approach enhances the robustness and consistency of multi-hazard assessment by explicitly accounting for uncertainty in hazard weighting. **(Figure 5-18D)** show low uncertainty value (< 6 %) at high multi hazard index area of **(Figure 5-18A)**. Hence, initial weights assign and **(Figure 5-18A)** best represent the multi hazard integration reliability. Mean hazard intensity **(Figure 5-18B)** is considered as final output map of Integrated multi hazard susceptibility.

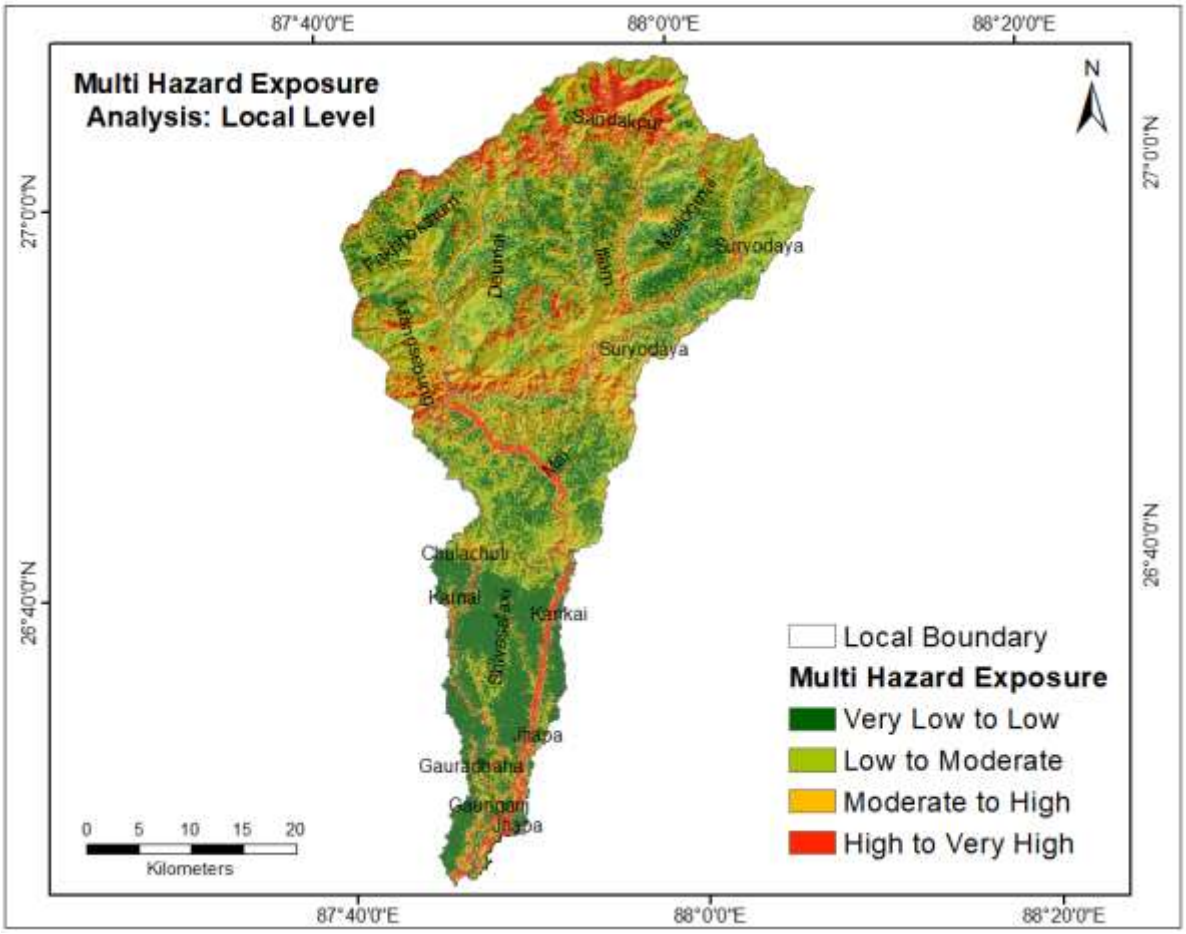


*Figure 5-19: Local Level wise Multi Hazard Suseptibility Assessment of Kankai Basin*

The multi-hazard susceptibility assessment of the Kankai Basin reveals a heterogeneous spatial distribution of hazard exposure influenced by landslide, flood, and soil erosion processes. The spatial distribution of multi hazard map reveals that 10.87 % of the area has high to very high 21.88 % of area has moderate to high, 37.58 % of the area has low to moderate susceptibility and 29.66 % of area has very low to low susceptibility (**Table 5-5,**

**Figure 5-20**). The resulting map **(Figure 5-19 & 21)** categorizes the basin into four hazard zones, where high susceptibility areas are predominantly concentrated in the upstream regions and along major river channels, reflecting the combined effects of steep topography and fluvial dynamics. Moderate hazard zones occupy the mid-basin areas, while the southern downstream regions are largely characterized by low to very low hazard levels. These findings highlight that the upper catchment is particularly vulnerable to cascading hazards, whereas the lower basin exhibits relatively stable conditions with localized flood risks. This spatial pattern provides critical insights for disaster reduction, land-use planning and targeted risk management in the basin.

*Table 5-5: Percentage Hazard by Area of the Basin for different Hazards*

| Hazard Class | % Erosion | % Flood | % Landslides | % Multi Hazard |
|---|---|---|---|---|
| Very Low to Low | 3.54 | 93.17 | 63.69 | 29.66 |
| Low to Moderate | 51.42 | 2.48 | 24.96 | 37.58 |
| Moderate to High | 43.79 | 1.59 | 7.6 | 21.88 |
| High to Very High | 1.25 | 2.76 | 3.75 | 10.87 |

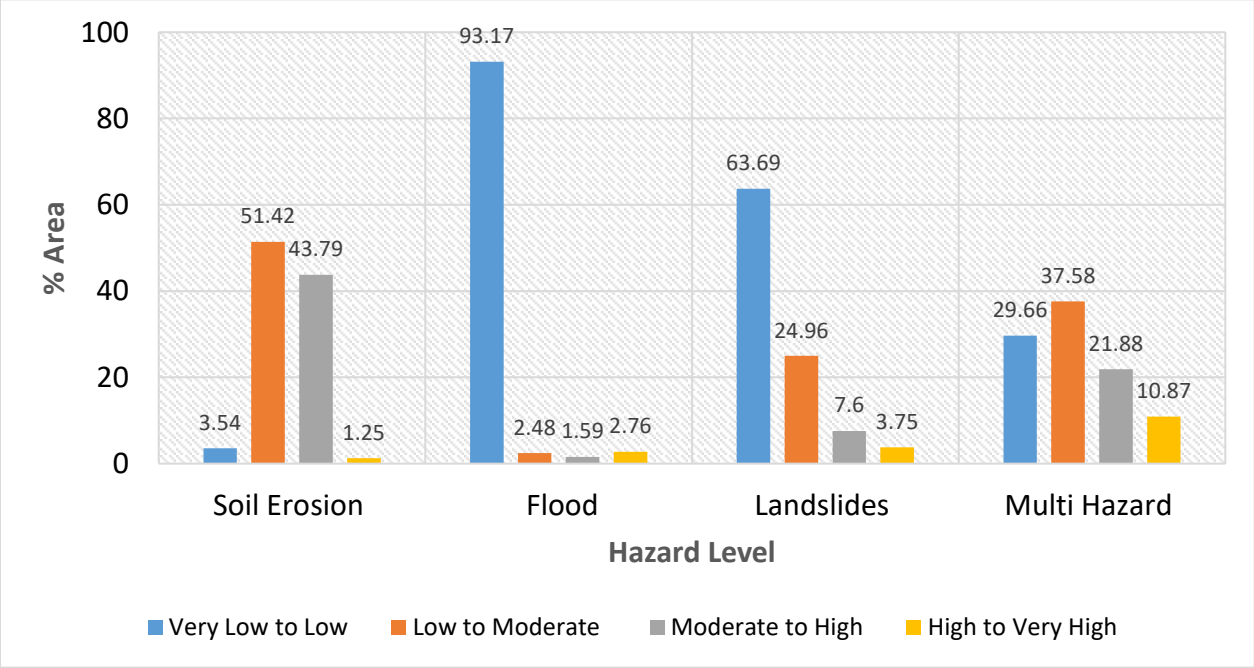


*Figure 5-20: Percentage area of different Hazard category for different hazards*

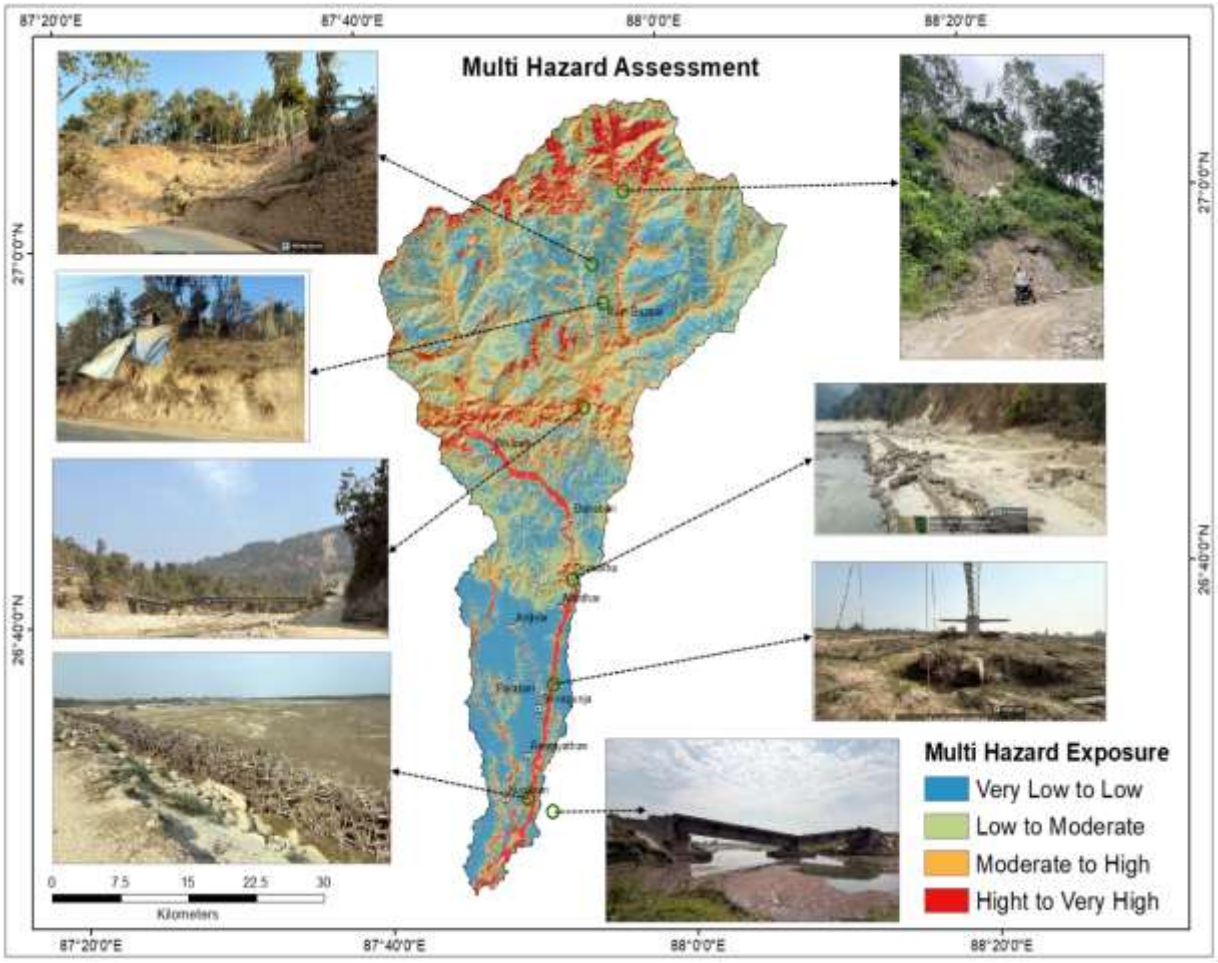


*Figure 5-21: Multi Hazard Suseptibility Assessment of Kankai Basin*

## 5.5 Multi Hazard Vulnerability and Risk Assessment

The multi-hazard risk assessment of the Kankai Basin was derived through an integrated geospatial analysis combining hazard intensity, population exposure, and spatial vulnerability indicators within a GIS environment. Individual hazard layers (e.g., flood, landslide, and erosion susceptibility) were first prepared using thematic variables such as slope, elevation, rainfall, drainage density, and land use, and each factor was standardized and weighted using Analytical Hierarchy Process approach. These hazard layers were then overlaid using a weighted linear combination to generate a composite hazard index. Population density was incorporated as an exposure layer, where higher population concentrations increase potential risk.

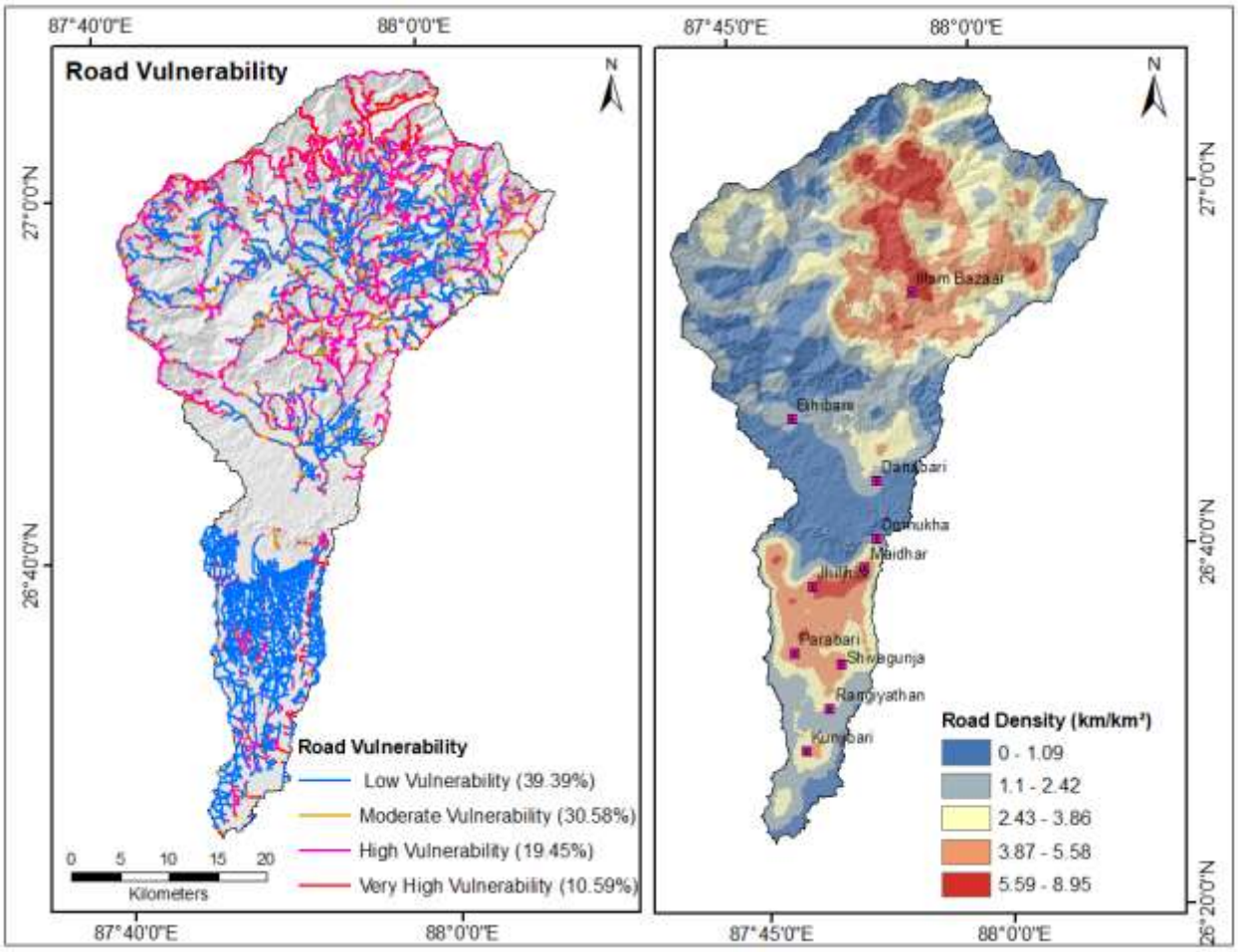


*Figure 5-22: Road Vulneralibity Assessment of Kankai Basin*

The final risk map **(Figure 5-24)** was generated by integrating the composite hazard index with the exposure layer through raster overlay analysis and reclassification into four categories from very low to very high risk. **Table 5-6** presents the distribution of road networks, building exposure, and areal extent across different vulnerability classes **(Figure 5-22 & 5-23)**, providing insight into the spatial pattern of multi-hazard risk (**Figure 5-24**). Overall, the low vulnerability class dominates the study area, covering 50.11 % of the basin area and containing the highest concentration of infrastructure, including 1208.9 km of roads and 28,880 buildings. This indicates that a significant portion of development is located in relatively safer zones. The moderate vulnerability class, accounting for 32.99 % of the area, also includes a substantial share of infrastructure (938.43 km of roads and 19976 buildings), suggesting that a large part of the

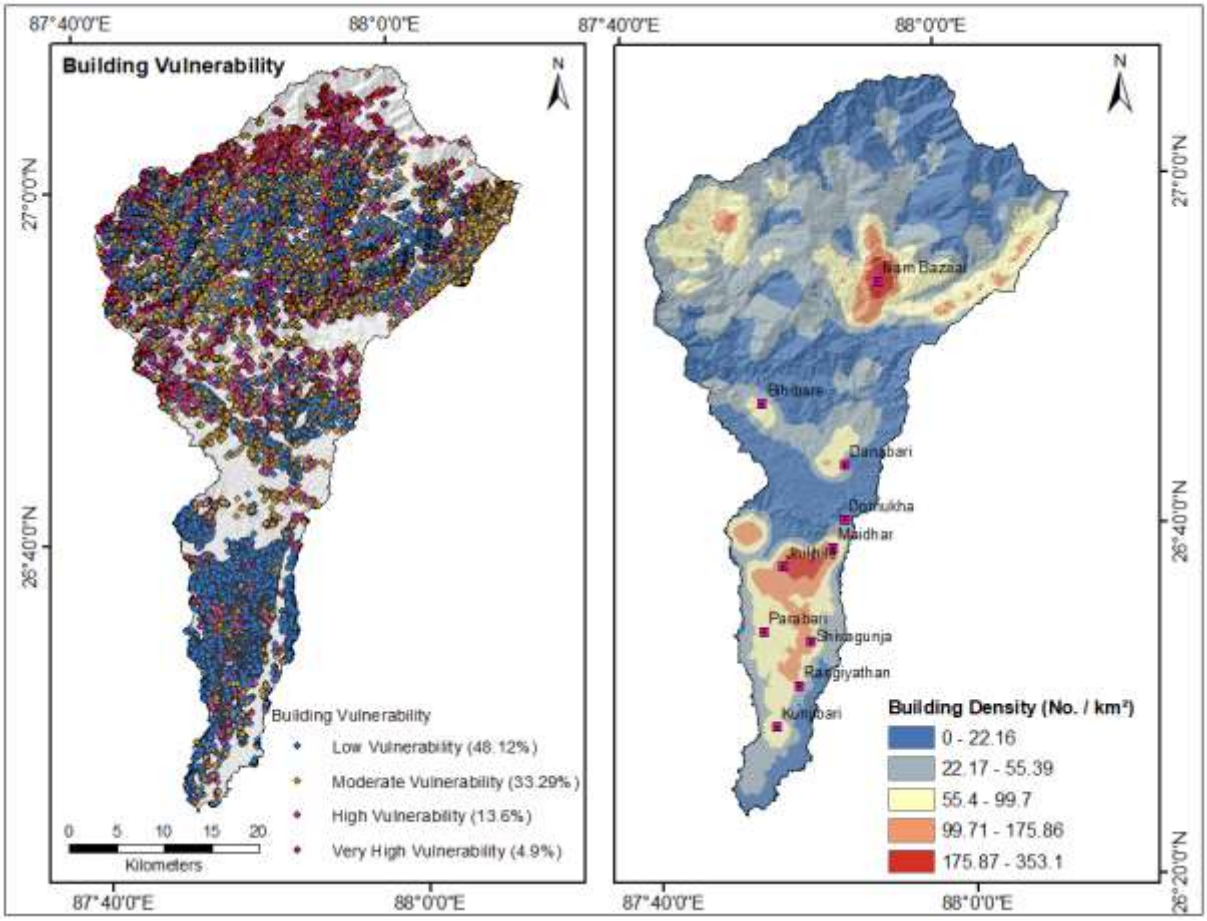


*Figure 5-23: Building Vulnerability Assessment of Kankai Basin*

*Table 5-6: Multiple Hazard Vulnerability & Risk assessment*

| Vulnerability Class | Road Vulnerability (km) | Building Vulnerability (No.) | MHRA by % Area |
|---|---|---|---|
| Low | 1208.9 | 28880 | 50.11 |
| Moderate | 938.43 | 19976 | 32.99 |
| High | 596.88 | 8163 | 13.10 |
| Very High | 325.06 | 2992 | 3.79 |

region lies in zones with intermediate risk, high and very high risk zones are concentrated mainly in the northern and central parts, particularly around Ilam Bazaar, reflecting the combined effect of higher hazard intensity and population concentration. Where hazards intensify under higher elevation, steep slope fragile geology and extreme environmental conditions such as heavy rainfall. In contrast, the high and very high vulnerability classes,

although covering a smaller proportion of the area (13.10 % and 3.79 % respectively), still contain a considerable amount of exposed infrastructure. Specifically, these zones include 596.88 km and 325.06 km of roads, and 8163 and 2992 buildings, respectively. This highlights that critical infrastructure and settlements are present within hazard-prone areas, increasing the potential risk of damage during multi-hazard events.

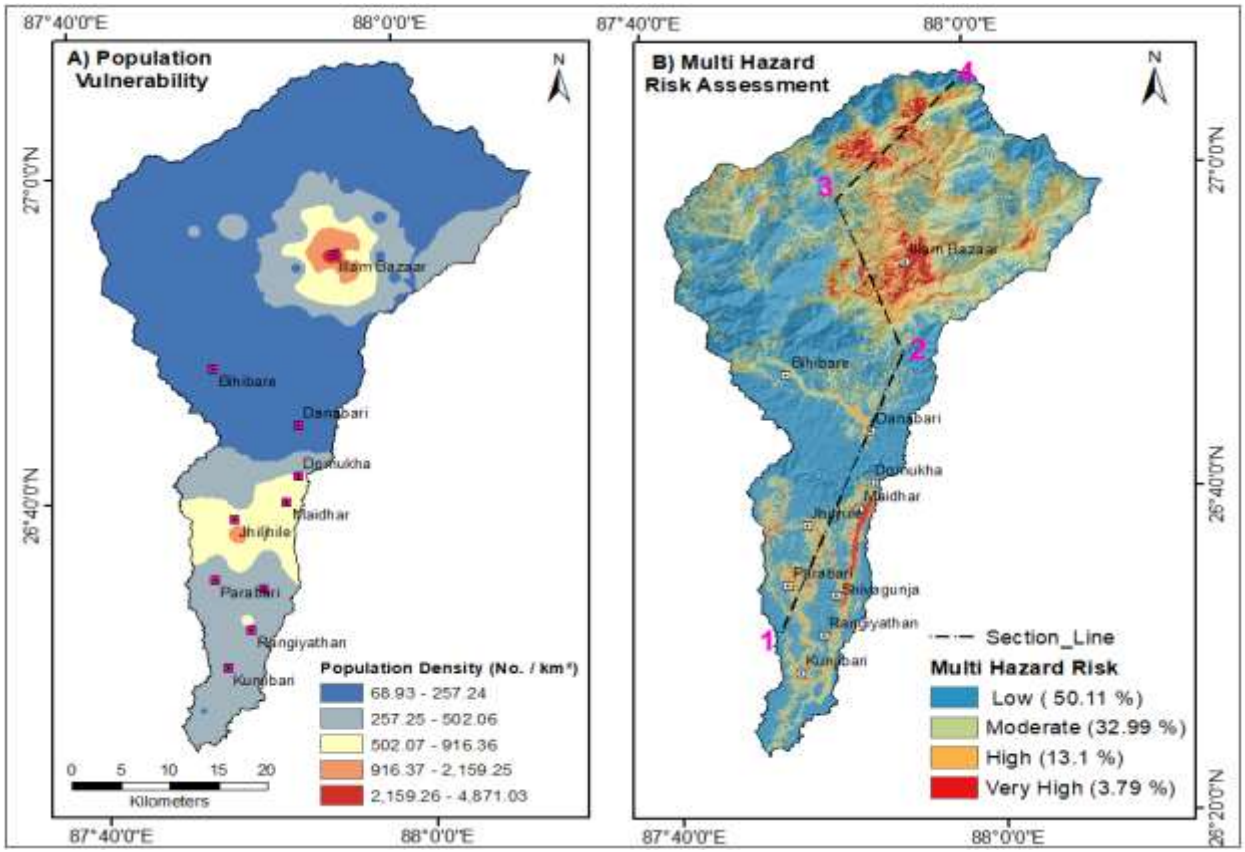


*Figure 5-24: Population vulnerability and Multi Hazard Risk Assessment of Kankai Basin*

**Figures 5-25** and **5-26** present the relationships between multi-hazard risk and distance from roads, and building density, respectively, along the transect 1–2–3–4 shown in **Figure 5-24(B)**. The results clearly indicate that multi-hazard risk generally decreases with increasing distance from roads, highlighting the strong influence of road proximity on hazard exposure. However, **Figure 5-26** reveals an exception along the upper segment of the transect (**3–4**), where multi-hazard risk remains relatively high despite low building density. This anomaly is primarily attributed to extensive local road construction in the upper basin

area, which has increased terrain disturbance and consequently elevated hazard susceptibility even in sparsely built-up zones.

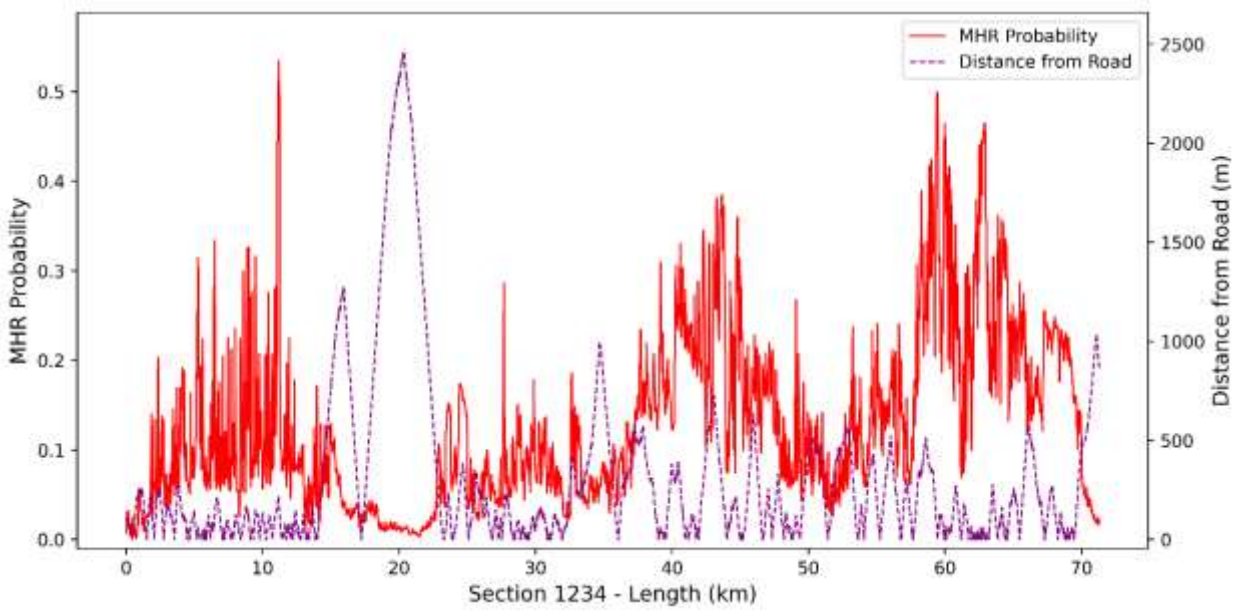


*Figure 5-25: Cross Sectional profile of soil erosion at 1234: Multi Hazard Risk Probability vs Distance from Road*

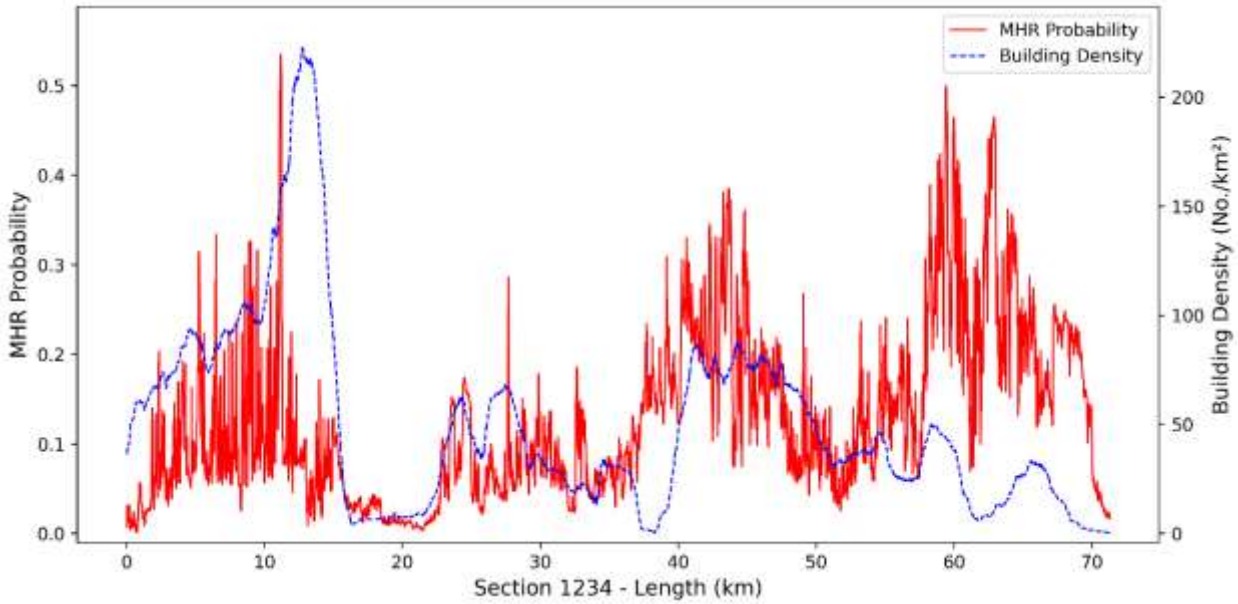


*Figure 5-26: Cross Sectional profile of soil erosion at 1234: Multi Hazard Risk Probability vs Building Density*

## 5.6 Discussion

*5.6.1 Hazard, Vulnerability and Risk Zonation*

Hazard assessment and mapping is the initial stage for disaster risk reduction particularly in mountainous region like Nepal, where complex geology and topography, intense rainfall patterns, and human activities interact to create hazardous conditions (R. K. Dahal, 2014; Hasegawa et al., 2009). The study integrated geospatial analysis of three rainfall induced hazards- landslide, flood and soil erosion to assess multi hazard risk assessment of Kankai Basin. The results reveal distinct spatial variability, with Highest Landslide susceptibility in the upper basin (Siwalik & Lesser Himalaya) due to steep fault-proximal slopes and fragile geology (Kayastha et al., 2013; Silwal et al., 2020), while flood and riverbank erosion dominate in the middle and lower basin with gentler terrain and active river dynamics (Hudait et al., 2024). Soil erosion analysis further reveals critical hotspots are along riverbanks, abrupt topographical change and exposed surfaces indicate significant localized geomorphic instability. Elevation, Slope, Geology, NDVI, and rainfall emerge as key drivers of cascading hazards consistent with previous studies (Khatakho et al., 2021; Nepal et al., 2019) in Nepal Himalaya, representing the validity of results. Furthermore, the result is validated using 133 multi-hazard hotspots obtained from field observations (**Figure 5-27**). The AUC value of 0.74 from field visit data (**Figure 5-28**) lower than testing (> 90 %) reflects spatial bias (roadside sampling), uncertainties, and unaccounted dynamic factors like rainfall and climate change. AUC > 70 % indicates acceptable performance (Bhandari et al., 2023; Joshi et al., 2026) of the model, thereby confirming the reliability of results.

Complex interplay between physical processes and human factors in shaping multi-hazard risk within the Kankai Basin (Nath & Hudait, 2024; Pudasaini et al., 2022). The upstream and mid-hill regions exhibit pronounced susceptibility to landslides not only trigger slope failures but also accelerate soil erosion (Aryal et al., 2023; Ulak, 1970). These processes collectively increase sediment load in river systems, thereby aggravating downstream flood risk. The exposure analysis at the local level reveals Significant exposure of roads, buildings, and population is observed along river valleys and transportation corridors are subject to moderate to very high exposure with overlapping hazards.

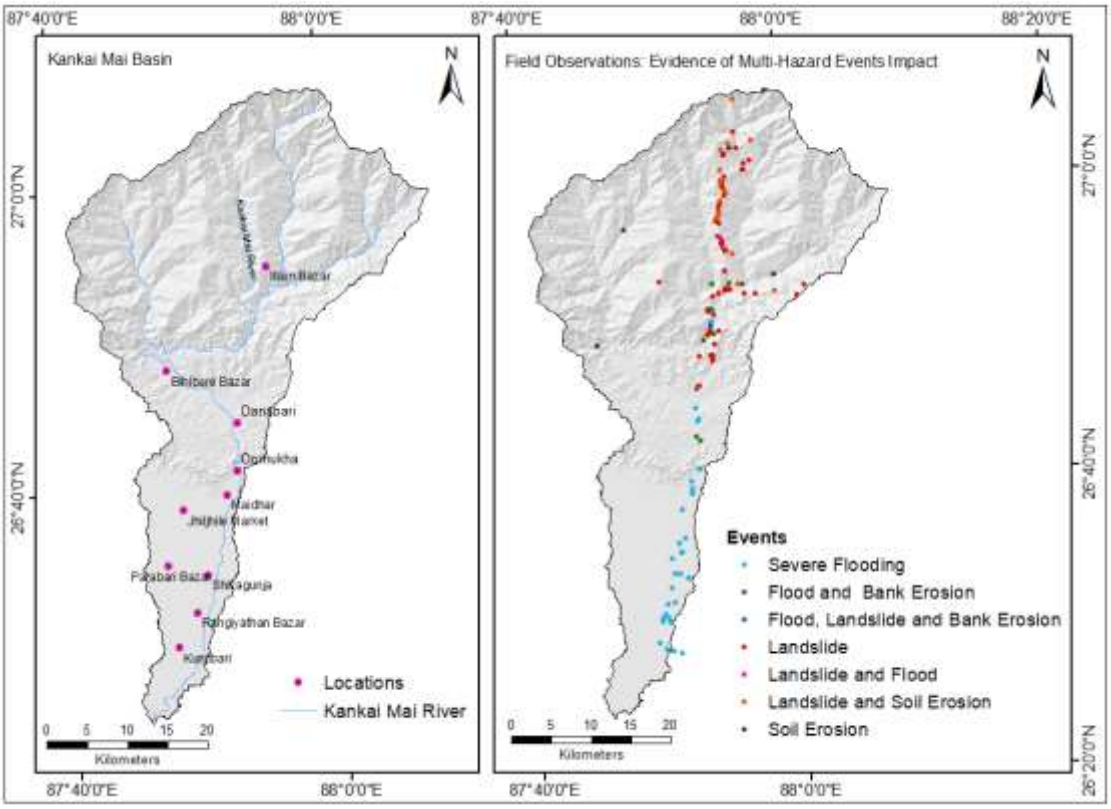


*Figure 5-27: Multi-Hazard Hotspots (total 133 locations) obtained from field visit*

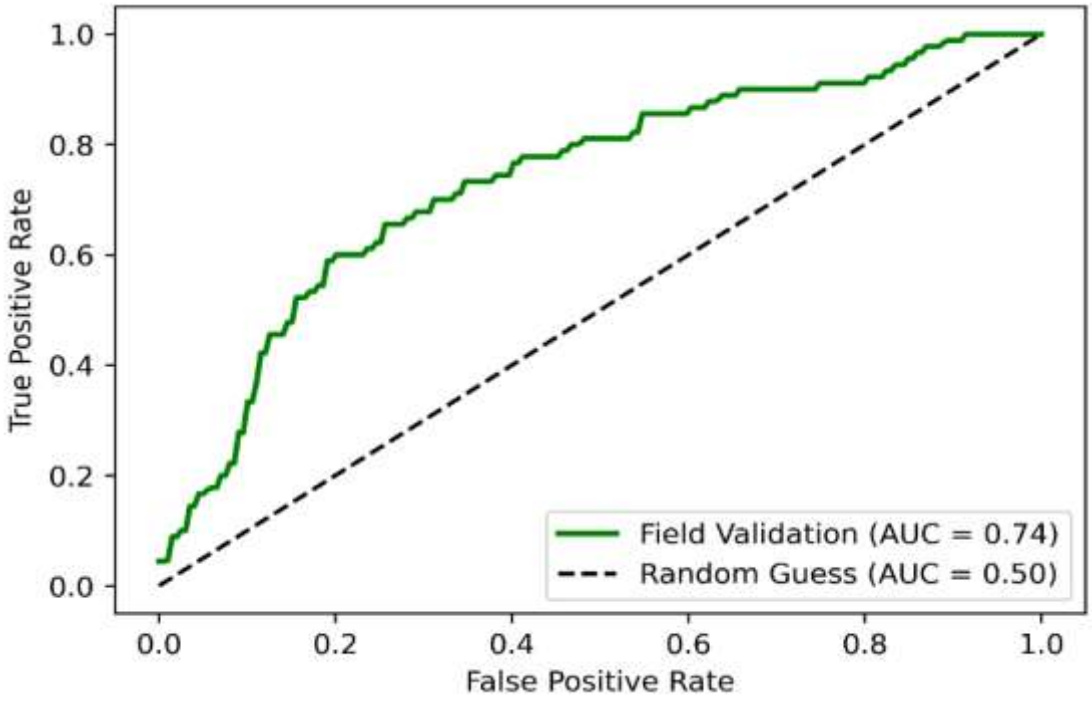


*Figure 5-28: Receiver Operating Characteristics curve from field visit data*

This is particularly concerning because such areas often represent economic and infrastructural hubs, where disruption can have far-reaching impacts beyond the immediate locality. Expanding settlements and unplanned land-use practices such as deforestation, road construction on unstable slopes, and encroachment into floodplains, are likely intensifying hazard susceptibility, especially in transitional zones between hill and Terai regions.

### *5.6.2 Contribution and Shortcomings*

This study contributes both methodologically and practically. Methodologically, it demonstrates the utility of machine learning techniques for generating reliable landslide susceptibility maps. Practically, it produces spatially explicit hazard, vulnerability, and risk maps that support disaster management, infrastructure planning, slope stabilization, and early warning systems in the Kankai Basin.

Despite its contributions, the study has some limitations. First, reliance on low resolution secondary data and sampling inconsistencies may have introduced uncertainties (Kc et al., 2024; Lamichhane et al., 2025). Second, dynamic factors such as seismic activity, land-use variability, and rainfall variability were not integrated into the modeling framework, potentially underestimating future risk (Jin et al., 2024; Lamichhane et al., 2025). Despite these limitations, our study provides a reliable tool for identifying landslide, flood and soil erosion-prone areas, as demonstrating its consistency with previous studies (Kayastha et al., 2013; Silwal et al., 2020; Nath & Hudait, 2024; Pudasaini et al., 2022).

# 6 Conclusions and Recommendations

## 6.1 Conclusions

The study demonstrates the effectiveness of integrated geospatial-SVM framework to assess rainfall-induced hazards and associated risk. Advancing multi-hazard mapping, the analysis highlights infrastructure exposure as a critical dimension in the Kankai Basin. Findings provide actionable insights for disaster risk reduction, land-use planning, watershed management, and safeguarding infrastructure. Following are major conclusions drawn from this study.

a) Landslide (Accuracy: 0.877, AUC: 0.95) and flood models (Accuracy: 0.885, AUC: 0.96) demonstrates strong predictive performance with key drivers include elevation, slope, geology, rainfall, soil type, fault proximity (Landslides) and slope, NDVI, rainfall, geology, soil types (Flooding).

b) Infrastructure vulnerability is notable, with 325.05 km (~10.6 %) of roads and 2,992 (~4.9 %) buildings exposed to very high-risk zone.

c) Landslide risk dominates in the Siwalik and Lesser Himalaya, particularly along the Main Boundary Thrust (MBT), where geological instability, steep slopes, and intense rainfall significantly increase slope failure, while flood risk is more pronounced in the Southern Terai, where unconsolidated alluvial deposits and active soil erosion along riverbanks heighten the likelihood of inundation.

d) The multi-hazard model achieved a field validation AUC of 0.74, slightly lower than internal results; likely due to sampling bias, uncertainties, and unaccounted dynamic factors.

e) Soil erosion is predominantly low (< 5 t/ha/yr), but localized hotspots reaching up to 280.3 t/ha/yr along river corridors and steep slopes, indicating strong topographic and fluvial controls.

## 6.2 Recommendations

The findings support integrated disaster risk reduction (DRR) and land-use planning by highlighting the spatial patterns of dominant hazards and their associated exposure. Hazard management should therefore be prioritized according to these spatial patterns, with greater focus on landslide-prone areas in the Siwalik and Lesser Himalaya, flood-prone zones in the southern Terai, and erosion hotspots along riverbanks. The notable vulnerability of infrastructure, including 10.6 % of roads and 4.9 % of buildings in very high-risk zones, underscores the need for targeted risk-informed planning and protection strategies. Structural interventions such as embankments, spurs, and gabion walls in erosion-prone river sections, along with slope stabilization measures (retaining structures, drainage control, and check dams) in upland areas, are supported by the results. In addition, flood-resilient construction practices, including elevated housing, can enhance short-term adaptation in vulnerable settlements, while nature-based approaches such as watershed restoration, bioengineering, and floodplain conservation contribute to sustainable risk reduction.

At the same time, the application of these results should account for underlying data and methodological limitations, including limited upstream data availability, uncertainties from moderate-resolution DEM and satellite imagery, and the simplified representation of complex hazard interactions. Non-structural measures, including land-use zoning, controlled settlement expansion, community preparedness, and early warning systems, remain essential for long-term resilience in light of these uncertainties. The framework demonstrates potential for application in other monsoon-dominated basins of Nepal, particularly in Himalayan and Siwalik regions, but requires careful local calibration of rainfall thresholds, slope conditions, land-use characteristics, and geological variability. Further refinement through improved field-based validation, development of systematic hazard inventories, and incorporation of multi-temporal climatic and hydrological datasets would enhance model reliability, better capture dynamic triggering mechanisms, and reduce uncertainty in future applications.

## References


1. Acharya, T. D. (2018). Regional scale landslide hazard assessment using machine learning methods in Nepal. *esis for: Doctor in Engineering Advisor,, esis for: Doctor in Engineering Advisor*.
2. Ader, T., Avouac, J. P., Liu-Zeng, J., Lyon-Caen, H., Bollinger, L., Galetzka, J., ... & Flouzat, M. (2012). Convergence rate across the Nepal Himalaya and interseismic coupling on the Main Himalayan Thrust: Implications for seismic hazard. *Journal of Geophysical Research: Solid Earth*, *117*(B4). https://doi.org/10.1029/2011JB009071
3. Aryal, A., Shrestha, M., Aryal, S., Upadhyay, S., & Maharjan, M. (2023). Spatio-temporal variability of streamflow in major and medium rivers of Nepal. *Journal of Hydrology: Regional Studies*, *50*, 101590. https://doi.org/10.1016/j.ejrh.2023.101590
4. Avand, M., Mohammadi, M., Mirchooli, F., Kavian, A., & Tiefenbacher, J. P. (2023). A new approach for smart soil erosion modeling: integration of empirical and machine-learning models. *Environmental Modeling & Assessment*, *28*(1), 145-160. https://doi.org/10.1007/s10666-022-09858-x
5. Bannari, A., Ghadeer, A., El-Battay, A., Hameed, N. A., & Rouai, M. (2017). Detection of areas associated with flash floods and erosion caused by rainfall storm using topographic attributes, hydrologic indices, and GIS. In *Global changes and natural disaster management: Geo-information technologies* (pp. 155-174). Cham: Springer International Publishing. https://doi.org/10.1007/978-3-319-51844-2_13
6. Bhatta, S., & Adhikari, B. R. (2024). Comprehensive risk evaluation in rapti valley, nepal: A multi-hazard approach. *Progress in Disaster Science*, *23*, 100346. https://doi.org/10.1016/j.pdisas.2024.100346
7. Borrelli, P., Alewell, C., Alvarez, P., Anache, J. A. A., Baartman, J., Ballabio, C., ... & Panagos, P. (2021). Soil erosion modelling: A global review and statistical analysis. *Science of the total environment*, *780*, 146494. https://doi.org/10.1016/j.scitotenv.2021.146494
8. Cenci, L., Pulvirenti, L., Boni, G., Chini, M., Matgen, P., Gabellani, S., ... & Pierdicca, N. (2017). An evaluation of the potential of Sentinel 1 for improving flash flood predictions via soil moisture–data assimilation. *Advances in Geosciences*, *44*, 89-100. https://doi.org/10.5194/adgeo-44-89-2017

9. Chauhan, V., Gupta, L., & Dixit, J. (2025). Machine learning and GIS-based multi-hazard risk modeling for Uttarakhand: integrating seismic, landslide, and flood susceptibility with socioeconomic vulnerability. *Environmental and Sustainability Indicators*, *26*, 100664. https://doi.org/10.1016/j.indic.2025.100664
10. Chen, T. H. K., Kincey, M. E., Rosser, N. J., & Seto, K. C. (2024). Identifying recurrent and persistent landslides using satellite imagery and deep learning: A 30-year analysis of the Himalaya. *Science of The Total Environment*, *922*, 171161. https://doi.org/10.1016/j.scitotenv.2024.171161
11. Cortes, C., & Vapnik, V. (1995). Support-vector networks. *Machine learning*, *20*(3), 273-297.
12. Cruden, D. M. (1993). Cruden, dm, varnes, dj, 1996, landslide types and processes, transportation research board, us national academy of sciences, special report, 247: 36-75. *Landslides Eng. Pract*, *24*, 20-47.
13. Dahal, R. K. (2014). Regional-scale landslide activity and landslide susceptibility zonation in the Nepal Himalaya. *Environmental Earth Sciences*, *71*(12), 5145-5164. https://doi.org/10.1007/s12665-013-2917-7
14. Dai, F. C., Lee, C. F., & Ngai, Y. Y. (2002). Landslide risk assessment and management: an overview. *Engineering geology*, *64*(1), 65-87. https://doi.org/10.1016/S0013-7952(01)00093-X
15. De Angeli, S., Malamud, B. D., Rossi, L., Taylor, F. E., Trasforini, E., & Rudari, R. (2022). A multi-hazard framework for spatial-temporal impact analysis. *International Journal of Disaster Risk Reduction*, *73*, 102829. https://doi.org/10.1016/j.ijdrr.2022.102829
16. Dou, J., Yunus, A. P., Tien Bui, D., Sahana, M., Chen, C. W., Zhu, Z., ... & Pham, B. T. (2019). Evaluating GIS-based multiple statistical models and data mining for earthquake and rainfall-induced landslide susceptibility using the LiDAR DEM. *Remote Sensing*, *11*(6), 638. https://doi.org/10.3390/rs11060638
17. Epple, L., Kaiser, A., Schindewolf, M., Bienert, A., Lenz, J., & Eltner, A. (2022). A review on the possibilities and challenges of today's soil and soil surface assessment techniques in the context of process-based soil erosion models. *Remote Sensing*, *14*(10), 2468. https://doi.org/10.3390/rs14102468

18. Feizbahr, M., Brake, N., Arbabkhah, H., Hariri Asli, H., & Woods, K. (2025). Flood Susceptibility Mapping Using Machine Learning and Geospatial-Sentinel-1 SAR Integration for Enhanced Early Warning Systems. *Remote Sensing*, *17*(20), 3471. https://doi.org/10.3390/rs17203471
19. Froude, M. J., & Petley, D. N. (2018). Global fatal landslide occurrence from 2004 to 2016. *Natural Hazards and Earth System Sciences*, *18*(8), 2161-2181. https://doi.org/10.5194/nhess-18-2161-2018
20. Gentile, R., Cremen, G., Galasso, C., Jenkins, L. T., Manandhar, V., Menteşe, E. Y., ... & McCloskey, J. (2022). Scoring, selecting, and developing physical impact models for multi-hazard risk assessment. *International Journal of Disaster Risk Reduction*, *82*, 103365. https://doi.org/10.1016/j.ijdrr.2022.103365
21. Ghimire, S. K., Higaki, D., & Bhattarai, T. P. (2013). Estimation of soil erosion rates and eroded sediment in a degraded catchment of the Siwalik Hills, Nepal. *Land*, *2*(3), 370-391. https://doi.org/10.3390/land2030370
22. Guzzetti, F., Mondini, A. C., Cardinali, M., Fiorucci, F., Santangelo, M., & Chang, K. T. (2012). Landslide inventory maps: New tools for an old problem. *Earth-Science Reviews*, *112*(1-2), 42-66. https://doi.org/10.1016/j.earscirev.2012.02.001
23. Khaliq, A. H., Basharat, M., Riaz, M. T., Riaz, M. T., Wani, S., Al-Ansari, N., ... & Linh, N. T. T. (2023). Spatiotemporal landslide susceptibility mapping using machine learning models: A case study from district Hattian Bala, NW Himalaya, Pakistan. *Ain Shams Engineering Journal*, *14*(3), 101907. https://doi.org/10.1016/j.asej.2022.101907
24. Hasegawa, S., Dahal, R. K., Yamanaka, M., Bhandary, N. P., Yatabe, R., & Inagaki, H. (2009). Causes of large-scale landslides in the Lesser Himalaya of central Nepal. *Environmental geology*, *57*(6), 1423-1434. https://doi.org/10.1007/s00254-008-1420-z
25. Hussain, A., Rasul, G., Mahapatra, B., Wahid, S., & Tuladhar, S. (2018). Climate change-induced hazards and local adaptations in agriculture: a study from Koshi River Basin, Nepal. *Natural Hazards*, *91*(3), 1365-1383. https://doi.org/10.1007/s11069-018-3187-1
26. Javidan, N., Kavian, A., Conoscenti, C., Jafarian, Z., Kalehhouei, M., & Javidan, R. (2024). Development of risk maps for flood, landslide, and soil erosion using machine learning

model. *Natural Hazards*, *120*(13), 11987-12010. https://doi.org/10.1007/s11069-024-06670-6

27. Joshi, B. R., Bhandary, N. P., Acharya, I. P., Niraj, K. C., & Bhandari, C. (2026). Integration of information value with machine learning method for an enhanced predictive performance in landslide susceptibility mapping. *Discover Geoscience*, *4*(1), 152. https://doi.org/10.1007/s44288-026-00517-2
28. Kavzoglu, T., Sahin, E. K., & Colkesen, I. (2014). Landslide susceptibility mapping using GIS-based multi-criteria decision analysis, support vector machines, and logistic regression. *Landslides*, *11*(3), 425-439. https://doi.org/10.1007/s10346-013-0391-7
29. Kayastha, P. (2012). Application of fuzzy logic approach for landslide susceptibility mapping in Garuwa sub-basin, East Nepal. *Frontiers of Earth Science*, *6*(4), 420-432. https://doi.org/10.1007/s11707-012-0337-8
30. KC, R., Sharma, K., Dahal, B. K., Aryal, M., & Subedi, M. (2024). Study of the spatial distribution and the temporal trend of landslide disasters that occurred in the Nepal Himalayas from 2011 to 2020. *Environmental Earth Sciences*, *83*(1), 42. https://doi.org/10.1007/s12665-023-11347-7
31. Khatakho, R., Gautam, D., Aryal, K. R., Pandey, V. P., Rupakhety, R., Lamichhane, S., ... & Adhikari, R. (2021). Multi-hazard risk assessment of Kathmandu Valley, Nepal. *Sustainability*, *13*(10), 5369. https://doi.org/10.3390/su13105369
32. Koirala, P., Thakuri, S., Joshi, S., & Chauhan, R. (2019). Estimation of soil erosion in Nepal using a RUSLE modeling and geospatial tool. *Geosciences*, *9*(4), 147. https://doi.org/10.3390/geosciences9040147
33. Lamichhane, K., Karki, S., Sharma, K., Khadka, B., Acharya, B., Biswakarma, K., ... & Bhattarai, P. K. (2025). Unraveling the causes and impacts of increasing flood disasters in the Kathmandu valley: lessons from the unprecedented September 2024 floods. *Natural Hazards Research*. https://doi.org/10.1016/j.nhres.2025.04.001
34. Lamichhane, S., Kansakar, A. R., Devkota, N., & Dahal, B. K. (2025). Integrating dynamic factors for predicting future landslide susceptibility. *Environmental Earth Sciences*, *84*(3), 89. https://doi.org/10.1007/s12665-025-12094-7

35. Lee, S., Hong, S. M., & Jung, H. S. (2017). A support vector machine for landslide susceptibility mapping in Gangwon Province, Korea. *Sustainability*, *9*(1), 48. https://doi.org/10.3390/su9010048
36. Luu, C., Ha, H., Bui, Q. D., Luong, N. D., Khuc, D. T., Vu, H., & Nguyen, D. Q. (2023). Flash flood and landslide susceptibility analysis for a mountainous roadway in Vietnam using spatial modeling. *Quaternary Science Advances*, *11*, 100083. https://doi.org/10.1016/j.qsa.2023.100083
37. Majhi, A., Shaw, R., Mallick, K., & Patel, P. P. (2021). Towards improved USLE-based soil erosion modelling in India: A review of prevalent pitfalls and implementation of exemplar methods. *Earth-Science Reviews*, *221*, 103786. https://doi.org/10.1016/j.earscirev.2021.103786
38. McAdoo, B. G., Quak, M., Gnyawali, K. R., Adhikari, B. R., Devkota, S., Rajbhandari, P. L., & Sudmeier-Rieux, K. (2018). Roads and landslides in Nepal: how development affects environmental risk. *Natural Hazards and Earth System Sciences*, *18*(12), 3203-3210. https://doi.org/10.5194/nhess-18-3203-2018
39. Merghadi, A., Yunus, A. P., Dou, J., Whiteley, J., ThaiPham, B., Bui, D. T., ... & Abderrahmane, B. (2020). Machine learning methods for landslide susceptibility studies: A comparative overview of algorithm performance. *Earth-Science Reviews*, *207*, 103225. https://doi.org/10.1016/j.earscirev.2020.103225
40. Moore, I. D., & Wilson, J. P. (1992). Length-slope factors for the Revised Universal Soil Loss Equation: Simplified method of estimation. *Journal of soil and water conservation*, *47*(5), 423-428. https://doi.org/10.1080/00224561.1992.12456740
41. Nath, U., & Hudait, M. (2024). Assessing the impact of channel migration and bank erosion on the loss of agricultural land and land use land cover change in the lower course of Kankai Mai River—a geospatial approach. In *Modern Cartography Series* (Vol. 12, pp. 439-456). Academic Press. https://doi.org/10.1016/B978-0-443-23890-1.00017-7
42. Niraj, K. C., Thapa, L., & Shukla, D. P. (2020). Fate of agricultural areas of Kailali District of Nepal: A temporal land use land cover change (LUCC) analysis. International Archives of the Photogrammetry, Remote Sensing and Spatial Information Sciences - ISPRS

Archives, 43(B3), 1601–1606. https://doi.org/10.5194/isprs-archives-XLIII-B3-2020-1601-2020

43. Okamura, M., Bhandary, N. P., Mori, S., Marasini, N., & Hazarika, H. (2015). Report on a reconnaissance survey of damage in Kathmandu caused by the 2015 Gorkha Nepal earthquake. *Soils and Foundations*, *55*(5), 1015-1029. https://doi.org/10.1016/j.sandf.2015.09.005
44. Pathak, L., Joshi, K., Ghimire, P., & Malla, R. (2026). Integrated multi-hazard assessment for climate-resilient watershed management: A transferable prioritization framework from Nepal's Mid-Hills. *Science of The Total Environment*, *1012*, 181239. https://doi.org/10.1016/j.scitotenv.2025.181239
45. Poudel, U., Adhikari, S., Karki, S., & Regmi, R. K. (2025). Climate change and hydropower resilience: a CMIP6-SWAT analysis of the Kankai River Basin's energy landscape. H2Open Journal, 8(6), 465–490. https://doi.org/10.2166/h2oj.2025.027
46. Pourghasemi, H. R., Kariminejad, N., Amiri, M., Edalat, M., Zarafshar, M., Blaschke, T., & Cerda, A. (2020). Assessing and mapping multi- hazard risk susceptibility using a machine learning technique. Scientific Reports, 1–11. https://doi.org/10.1038/s41598-020-60191-3
47. Rahman, G., Bacha, A. S., Farhan, M., Moazzam, U., Rahman, A. U., Mahmood, S., Almohamad, H., Abdullah, A., Dughairi, A., & Al-mutiry, M. (2022). Assessment of landslide susceptibility , exposure , vulnerability , and risk in shahpur valley , eastern hindu kush. August, 1–23. https://doi.org/10.3389/feart.2022.953627
48. Rai, P., Baral, A., Pokhrel, K., Sah, P. K., Magar, P. R., & Adhikari, B. R. (2025). Multi-hazard risk assessment of Waling Municipality, Syangja, Nepal. Geomatics, Natural Hazards and Risk, 16(1), 2485327. https://doi.org/10.1080/19475705.2025.2485327
49. Reichenbach, P., Rossi, M., Malamud, B. D., Mihir, M., & Guzzetti, F. (2018). A review of statistically-based landslide susceptibility models. Earth-Science Reviews, 180(November 2017), 60–91. https://doi.org/10.1016/j.earscirev.2018.03.001
50. Rusk, J., Maharjan, A., Tiwari, P., Chen, T. H. K., Shneiderman, S., Turin, M., & Seto, K. C. (2022). Multi-hazard susceptibility and exposure assessment of the Hindu Kush Himalaya. Science of the Total Environment, 804, 150039. https://doi.org/10.1016/j.scitotenv. 2021. 150039

51. Senanayake, S., Pradhan, B., Huete, A., & Brennan, J. (2020). A review on assessing and mapping soil erosion hazard using geo-informatics technology for farming system management. Remote Sensing, 12(24), 1–25. https://doi.org/10.3390/rs12244063
52. Sharma, K. K., Bhandary, N. P., Subedi, M., & Rajan, K. C. (2025). Integration of Landslide Susceptibility and Road Infrastructure Vulnerability for Risk Assessment and Mountain Road Resilience Enhancement. Indian https://doi.org/10.1007/s40098-025-01222-6
53. Shrestha, B. R., Rai, R. K., & Marasini, Saroj et al. (2020). Review of Flood Hazards Studies in Nepal. The Geographic Base, 7, 24–32. https://doi.org/10.3126/tgb.v7i0.34266
54. Silwal, C. B., Pathak, D., Adhikari, D., & Adhikari, T. R. (2020). Climate change and its possible impact in groundwater resource of the Kankai River Basin, East Nepal Himalaya. Climate, 8(11), 137. https://doi.org/10.3390/cli8110137
55. Skilodimou, H. D., Bathrellos, G. D., Chousianitis, K., Youssef, A. M., & Pradhan, B. (2019). Multi-hazard assessment modeling via multi-criteria analysis and GIS: a case study. Environmental Earth Sciences, 78(2), 0. https://doi.org/10.1007/s12665-018-8003-4
56. Sreelakshmi, S., Vinod Chandra, S. S., & Shaji, E. (2022). Landslide identification using machine learning techniques: Review, motivation, and future prospects. Earth Science Informatics, 15(4), 2063–2090. https://doi.org/10.1007/s12145-022-00889-2
57. Thapa, P. B., Lamichhane, S., Joshi, K. P., Regmi, A. R., Bhattarai, D., & Adhikari, H. (2023).
58. Thapa, P. B., Lamichhane, S., Joshi, K. P., Regmi, A. R., Bhattarai, D., & Adhikari, H. (2023). Landslide Susceptibility Assessment in Nepal's Chure Region: A Geospatial Analysis. Land, 12(12). https://doi.org/10.3390/land12122186
59. Uddin, K., Murthy, M. S. R., Wahid, S. M., & Matin, M. A. (2016). Estimation of Soil Erosion Dynamics in the Koshi Basin Using GIS and Remote Sensing to Assess Priority Areas for Conservation. PLoS ONE, 11(3). https://doi.org/10.1371/journal.pone.0150494
60. Wahid, S. M., Kilroy, G., Shrestha, A. B., Bajracharya, S. R., & Hunzai, K. (2016). Opportunities and challenges in the trans-boundary Koshi River Basin. River System Analysis and Management, 341–352. https://doi.org/10.1007/978-981-10-1472-7_18
61. Wischmeier, W. H., & Smith, D. D. (1978). Predicting rainfall erosion losses: a guide to conservation planning (Issue 537). Department of Agriculture, Science and Education Administration.

62. Youssef, A. M., Mahdi, A. M., & Reza, H. (2022). Landslides and flood multi - hazard assessment using machine learning techniques. Bulletin of Engineering Geology and the Environment. https://doi.org/10.1007/s10064-022-02874-x
63. Zhang, J., Regmi, A. D., Liu, R., & Khanal, N. (2017). Landslides Inventory and Trans-boundary Risk Management in Koshi River Landslides inventory and trans-boundary risk management in Koshi river. August. https://doi.org/10.1007/978-981-10-2890-8
64. Zhu, A. X., Miao, Y., Liu, J., Bai, S., Zeng, C., Ma, T., & Hong, H. (2019). A similarity-based approach to sampling absence data for landslide susceptibility mapping using data-driven methods. Catena, 183(October 2018), 104188. https://doi.org/10.1016/j.catena.2019.104188

# APPENDICES

## Appendix A: Field Observation and Survey Data

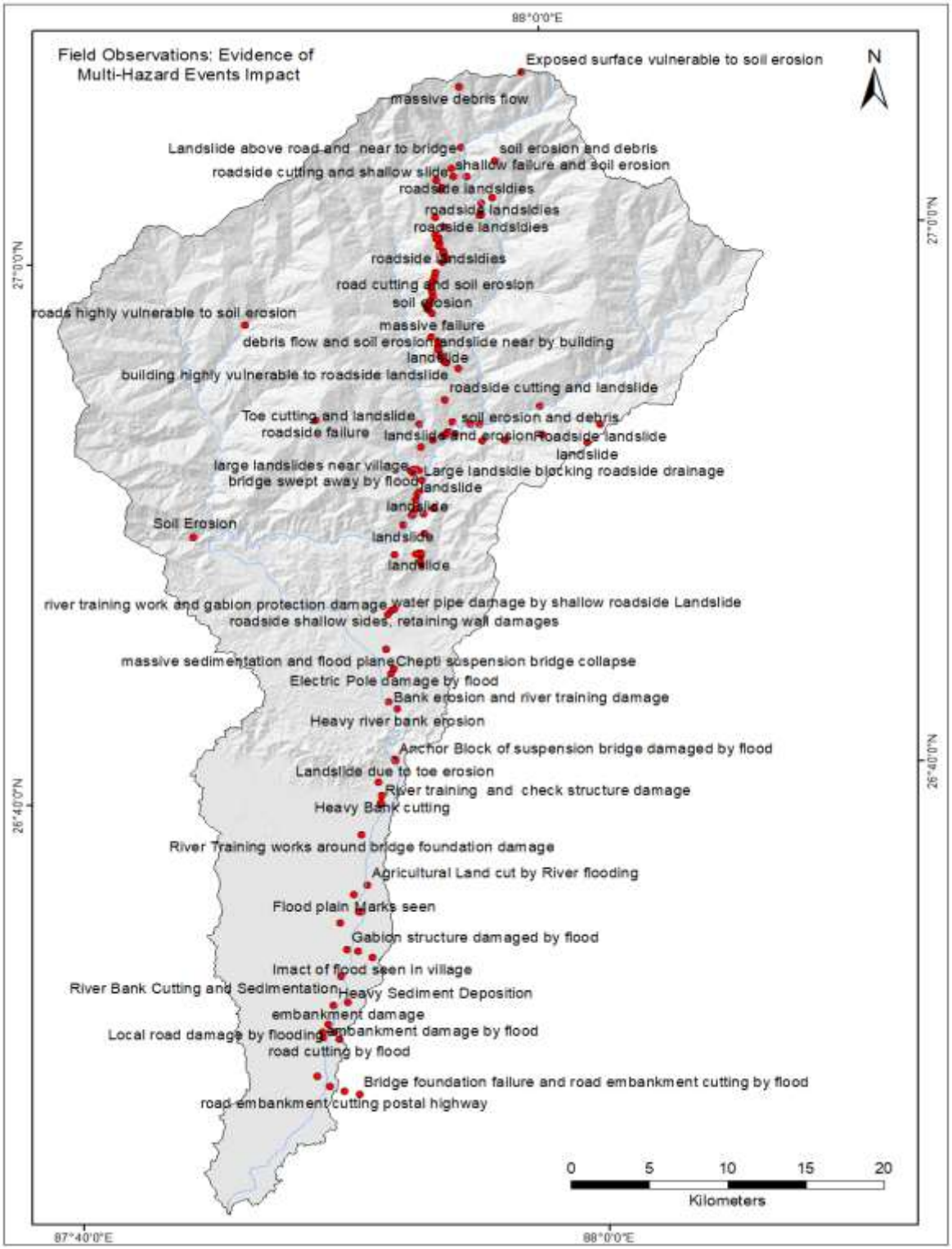


*Figure A-1: Map showing Multi Hazard Events obtained from field visit and survey*

*Table A-1: Details and Coordinates of Multi Hazard Events*

| SN. | Hazard events | Longitude | Latitude | Remarks |
|---|---|---|---|---|
| 0 | Flooding | 87.8358 | 26.509 | massive damage by flood |
| 1 | Flooding | 87.8525 | 26.591 | Lalpani- chandradangi suspension bridge anchor block & abutment damage |
| 2 | Flooding | 87.8437 | 26.568 | Gabion structure damaged by flood |
| 3 | Flooding | 87.8504 | 26.567 | Madargach - sivgungh bridge foundation impacted by flood |
| 4 | Flooding | 87.8594 | 26.563 | Impact of flood seen in village |
| 5 | Flooding | 87.829 | 26.523 | Local road damage by flooding |
| 6 | Flooding | 87.833 | 26.534 | Heavy sediment deposition |
| 7 | Flooding | 87.8421 | 26.536 | Embankment damage |
| 8 | Flooding | 87.8352 | 26.513 | Road cutting by flood |
| 9 | Flooding | 87.8324 | 26.518 | Heavy flooding - September 2024: causing house displacement |
| 10 | Flooding | 87.8464 | 26.478 | Bridge foundation failure and road embankment cutting by flood |
| 11 | Flooding | 87.8367 | 26.481 | Road embankment cutting postal highway |
| 12 | Flooding | 87.8277 | 26.484 | Heavy sedimentation on postal highway bridge under construction |
| 13 | Flooding | 87.8197 | 26.491 | River bank cutting, river training structure damage and flood overtopping embankment |
| 14 | Flooding | 87.8254 | 26.514 | Heavy sedimentation to agricultural fields, embankment cutting & overtopping |
| 15 | Flooding | 87.8248 | 26.518 | Embankment damage by flood |

| | | | | |
|---|---|---|---|---|
| 16 | Flooding | 87.8387 | 26.552 | River bank cutting and sedimentation |
| 17 | Flooding | 87.8401 | 26.585 | River training work around the bridge damaged by flood |
| 18 | Flooding | 87.85 | 26.602 | Flood plain marks seen |
| 19 | Flooding | 87.8569 | 26.639 | River training works around bridge foundation damage |
| 20 | Flooding | 87.8589 | 26.607 | Agricultural land cut by river flooding |
| 21 | Flooding | 87.8705 | 26.657 | Kankai bridge foundation scouring |
| 22 | Flooding | 87.8705 | 26.658 | River training and check structure damage |
| 23 | Flooding | 87.8713 | 26.662 | Heavy bank cutting |
| 24 | Flooding | 87.8695 | 26.671 | Gabion protection work around bridge foundation damage and heavy sedimentation by flash flood |
| 25 | Flood and bank erosion | 87.8806 | 26.684 | Landslide due to toe erosion |
| 26 | Flood | 87.881 | 26.683 | Anchor block of suspension bridge damaged by flood |
| 27 | Flood | 87.8796 | 26.752 | Massive sedimentation and flood plane |
| 28 | Flood | 87.8818 | 26.737 | Chepti suspension bridge collapse |
| 29 | Flood and bank erosion | 87.884 | 26.715 | Heavy river bank erosion |
| 30 | Landslide and soil erosion | 87.9048 | 26.804 | Massvie soil erosion |
| 31 | Flood and bank erosion | 87.9052 | 26.809 | Landslide and erosion |

| | | | | |
|---|---|---|---|---|
| 32 | Flood and bank erosion | 87.9049 | 26.81 | Heavy bank erosion |
| 33 | Flood and bank erosion | 87.904 | 26.811 | Heavy bank erosion |
| 34 | Flood and bank erosion | 87.8951 | 26.829 | Heavy bank erosion |
| 35 | Landslide | 87.9149 | 26.838 | Massive landslide and debris flow |
| 36 | Flood and bank erosion | 87.904 | 26.838 | Heavy bank erosion |
| 37 | Flood, landslide and bank erosion | 87.9041 | 26.844 | Heavy bank erosion leading landslides |
| 38 | Flood, landslide and bank erosion | 87.9051 | 26.847 | Heavy bank erosion leading landslide |
| 39 | Flood | 87.9056 | 26.862 | Bridge swept away by flood |
| 40 | Flood, landslide and bank erosion | 87.9072 | 26.862 | Large landslide blocking roadside drainage |
| 41 | Flood, landslide and bank erosion | 87.925 | 26.931 | Heavy bank erosion leading landslides |
| 42 | Landslide | 87.9239 | 26.938 | Massive Landslide |
| 43 | Landslide | 87.92 | 26.944 | Landslide nearby building |
| 44 | Landslide | 87.9213 | 26.958 | Massive failure |
| 45 | Landslide | 87.9187 | 26.961 | Roadside failure |
| 46 | Landslide | 87.9188 | 26.962 | Buildings highly vulnerable to landslides |
| 47 | Landslide | 88.0152 | 26.874 | Massive Landslide |

| | | | | |
|---|---|---|---|---|
| 48 | Flood and bank erosion | 87.8794 | 26.72 | Bank erosion and river training damage |
| 49 | Flood | 87.8835 | 26.74 | Electric pole damage by flood |
| 50 | Landslide | 87.882 | 26.774 | Water pipe damage by shallow roadside landslide |
| 51 | Flooding | 87.8841 | 26.776 | River training work and gabion protection damage |
| 52 | Landslide | 87.8865 | 26.777 | Roadside shallow sides, retaining wall damages |
| 53 | Landslide | 87.9047 | 26.806 | Roadside shallow sides |
| 54 | Landslide | 87.8884 | 26.81 | Severe landslide |
| 55 | Landslide | 87.9054 | 26.811 | Landslide and debris chocking roadside drainage |
| 56 | Landslide | 87.9021 | 26.81 | Shallow roadside slide |
| 57 | Landslide | 87.9079 | 26.823 | Roadside cutting and landslide |
| 58 | Landslide | 87.9007 | 26.834 | Rockfall and debris |
| 59 | Landslide | 87.9017 | 26.835 | Bridge foundation collapse, heavy landslides and flooding |
| 60 | Flood and bank erosion | 87.9083 | 26.835 | Heavy flooding, sedimentation and river bank erosion |
| 61 | Landslide | 87.9035 | 26.839 | Landslides blocking road |
| 62 | Flooding | 87.9062 | 26.849 | Heavy debris and sedimentation with minor bridge damage |
| 63 | Landslide | 87.9034 | 26.86 | Large landslides near village |
| 64 | Landslide | 87.9087 | 26.856 | Road damage due to heavy cutting and landslides |
| 65 | Landslide | 87.9016 | 26.862 | Retaining wall and gabion structure damage by landslide |
| 66 | Landslide | 87.9025 | 26.862 | Retaining wall and gabion structure damage by landslide |

| | | | | |
|---|---|---|---|---|
| 67 | Flood and bank erosion | 87.904 | 26.863 | Toe cutting and road subsidance and failure, gabion structure damage |
| 68 | Landslide | 87.9094 | 26.876 | House protected from landslide by gabion walls |
| 69 | Landslide | 87.9264 | 26.905 | Roadside cutting and landslide |
| 70 | Landslide | 87.9279 | 26.928 | Road side landslide damaging watersupply pipe and blockign side drain |
| 71 | Landslide | 87.9287 | 26.927 | Building highly vulnerable to roadside landslide |
| 72 | Landslide | 87.9276 | 26.928 | Heavy road sidecutting leading landslide and damaging electric pole |
| 73 | Landslide and soil erosion | 87.9258 | 26.932 | Heavy cutting leading roadside failure |
| 74 | Landslide | 87.924 | 26.935 | Landslide & debris flow damaging electric pole and gabion structure |
| 75 | Landslide | 87.9236 | 26.936 | Road side slide and soil erosion |
| 76 | Landslide and flood | 87.9238 | 26.941 | Debris flow and soil erosion |
| 77 | Landslide | 87.9181 | 26.962 | Roadside shallow slide |
| 78 | Landslide | 87.9181 | 26.963 | Roadside shallow slide |
| 79 | Landslide and soil erosion | 87.919 | 26.963 | Roadside shallow slide and soil erosion |
| 80 | Landslide and soil erosion | 87.9198 | 26.964 | Roadside shallow slide and soil erosion |
| 81 | Landslide and soil erosion | 87.9208 | 26.966 | Soil erosion |

| | | | | |
|---|---|---|---|---|
| 82 | Landslide and soil erosion | 87.9223 | 26.969 | Roadside shallow slide and soil erosion |
| 83 | Landslide and soil erosion | 87.9222 | 26.972 | Massive Soil erosion risk |
| 84 | Landslide and soil erosion | 87.922 | 26.974 | Roadside cutting and soil erosion |
| 85 | Landslide | 87.9229 | 26.978 | Roadside landslide and drainage blockage |
| 86 | Landslide | 87.9242 | 26.981 | Roadside landslide and gabion structure damage |
| 87 | Landslide and soil erosion | 87.9253 | 26.983 | Road cutting and soil erosion |
| 88 | Landslide | 87.93 | 26.99 | Road landslide and debris flow |
| 89 | Landslide and soil erosion | 87.9334 | 26.991 | Road cutting and soil erosion |
| 90 | Landslide and soil erosion | 87.9309 | 26.995 | Road landslide and debris flow near village |
| 91 | Landslide | 87.9307 | 26.996 | Heavy excavaton rock fall and erosion |
| 92 | Landslide and soil erosion | 87.9308 | 26.996 | Heavy soil erosion and exposed survace |
| 93 | Landslide and soil erosion | 87.9287 | 27.001 | Road side cutting and soil erosion |
| 94 | Soil erosion | 87.9285 | 27.005 | Exposed roadslope highly vulnareble to soil erosion |
| 95 | Landslide and soil erosion | 87.9265 | 27.007 | Soil erosion and shallow landslide |
| 96 | Landslide and soil erosion | 87.9269 | 27.004 | Shallow landslide and soil errosion |
| 97 | Landslide | 87.9173 | 26.88 | Shallow landslide along the road |

| | | | | |
|---|---|---|---|---|
| 98 | Flood and bank erosion | 87.909 | 26.89 | Toe cutting and landslide |
| 99 | Landslide | 87.9251 | 26.883 | Shallow landslide along the road blocking drainage |
| 100 | Landslide | 87.9264 | 26.885 | Massive landslide and protection work failure |
| 101 | Landslide | 87.9276 | 26.884 | Massive landslide and rock fall |
| 102 | Flood and bank erosion | 87.9302 | 26.89 | Toe cutting land slide debris flow and erosion |
| 103 | Landslide | 87.9314 | 26.883 | Shallow landslide and protection work failure |
| 104 | Landslide | 87.9484 | 26.878 | Shallow landslide and drainage blocked |
| 105 | Landslide and soil erosion | 87.9413 | 26.889 | Landslide and erosion |
| 106 | Flood and bank erosion | 87.9475 | 26.888 | Sediment deposition and bank cutting |
| 107 | Landslide | 87.9632 | 26.878 | Shallo failure at road side |
| 108 | Landslide and soil erosion | 87.9871 | 26.88 | Land slide and soil erosion near house |
| 109 | Soil erosion | 87.9866 | 26.898 | Soil erosion and debris |
| 110 | Soil erosion | 87.9401 | 27.042 | Roadside cutting and shallow slide |
| 111 | Landslide and soil erosion | 87.9292 | 27.04 | Roadside shallow slide and soil erosion |
| 112 | Landslide | 87.9315 | 27.034 | Roadside landslides |
| 113 | Landslide | 87.9327 | 27.036 | Roadside landslides |
| 114 | Landslide | 87.9319 | 27.011 | Roadside landslides |
| 115 | Landslide and soil erosion | 87.9272 | 27.017 | Roadside failure and soil erosion |
| 116 | Landslide | 87.9281 | 26.999 | Roadside landslides |

| | | | | |
|---|---|---|---|---|
| 117 | Landslide | 87.9553 | 27.018 | Roadside landslides |
| 118 | Landslide | 87.9566 | 27.018 | Roadside landslides |
| 119 | Landslide | 87.9567 | 27.025 | Roadside landslides |
| 120 | Landslide | 87.9642 | 27.028 | Roadside landslides |
| 121 | Landslide | 87.949 | 27.041 | Roadside landslides |
| 122 | Landslide | 87.9461 | 27.06 | Landslide above road and near to bridge |
| 123 | Landslide and soil erosion | 87.9391 | 27.047 | Shallow failure and soil erosion |
| 124 | Landslide | 88.0244 | 26.884 | Roadside landslide |
| 125 | Landslide | 87.9254 | 26.882 | Valley side of road damaged |
| 126 | Landslide and soil erosion | 87.9358 | 26.924 | Massive soil erosion and debris flow |
| 127 | Landslide and soil erosion | 87.9674 | 27.05 | Soil erosion and debris |
| 128 | Soil erosion | 87.9875 | 27.105 | Exposed surface vulnerable to soil erosion |
| 129 | Landslide and soil erosion | 87.9473 | 27.097 | Massive debris flow |
| 130 | Landslide | 87.8433 | 26.896 | Roadside failure |
| 131 | Soil erosion | 87.7609 | 26.828 | Exposed surface vulnerable soil erosion |
| 132 | Soil erosion | 87.8016 | 26.957 | Roads highly vulnerable to soil erosion |

## Appendix B: Photograph of Different Hazard taken during Field Visit

*Figure B-1: Photographs of Landslide and Flood events obtained from Field Visits*

*Figure B-2: Photographs of multi-hazard events obtained from Field Visits*

## Appendix C: Landslide and Corresponding BSI - NDVI Time Series Analysis

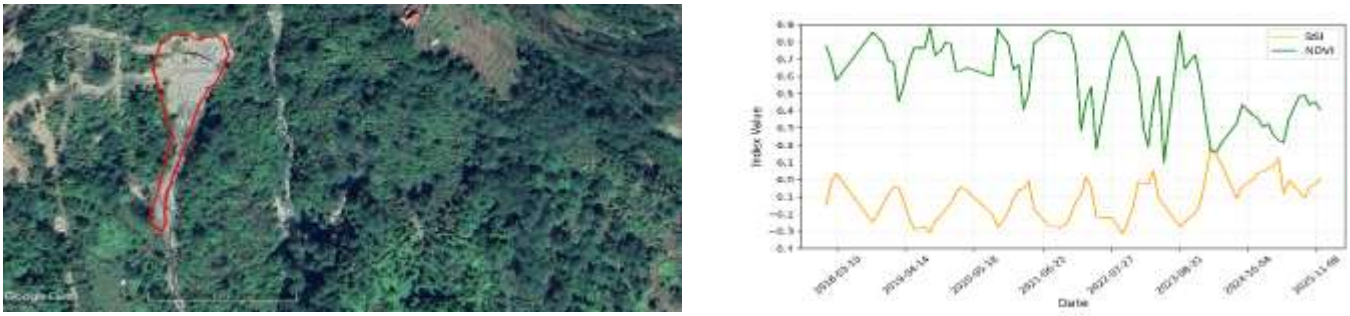


*Figure C-1: Landslide and corresponding BSI & NDVI time series analysis at (Latitude: 27° 3'48.69"N, Longitude: 87°55'47.08"E)*

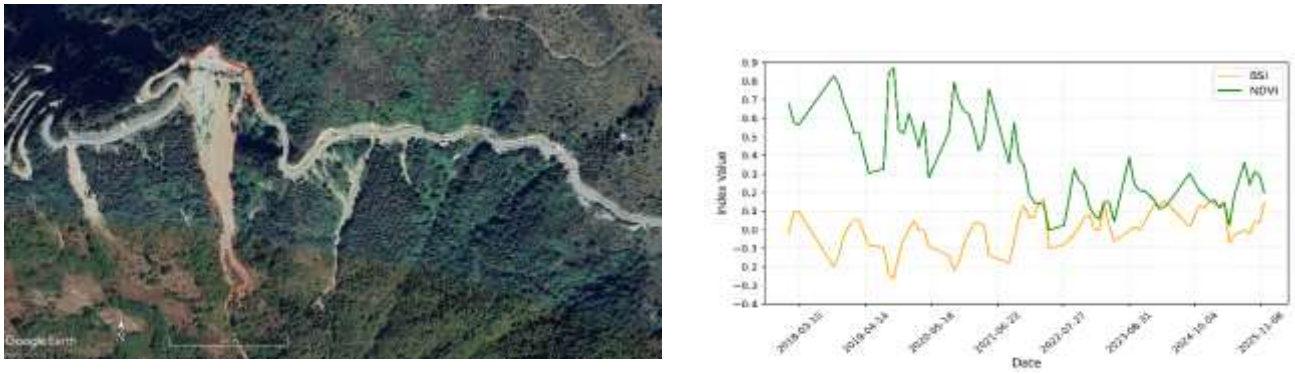


*Figure C-2: Landslide and corresponding BSI & NDVI time series analysis at (Latitude: 27° 3'4.33"N, Longitude: 87°58'2.25"E)*

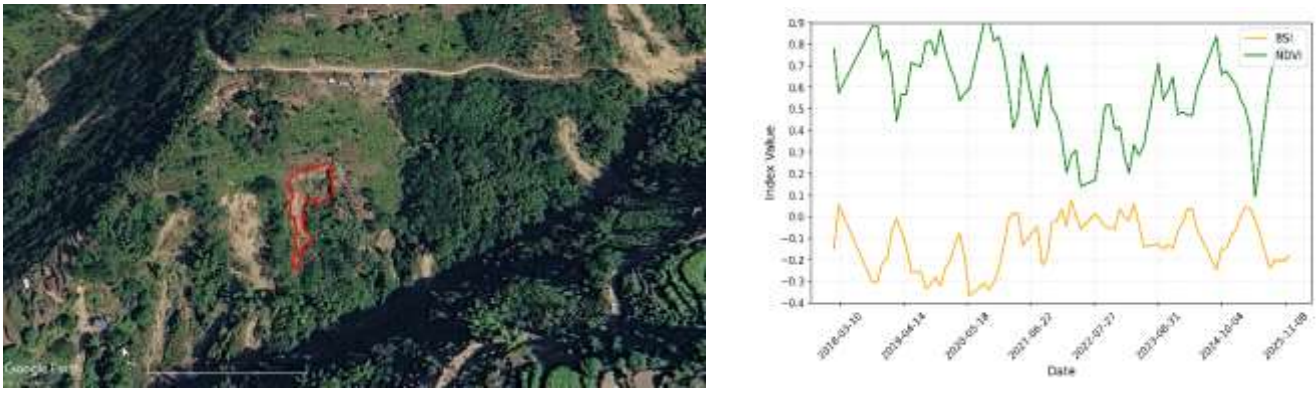


*Figure C-3: Landslide and corresponding BSI & NDVI time series analysis at (Latitude: 27° 1'45.45"N, Longitude: 87°53'45.16"E)*

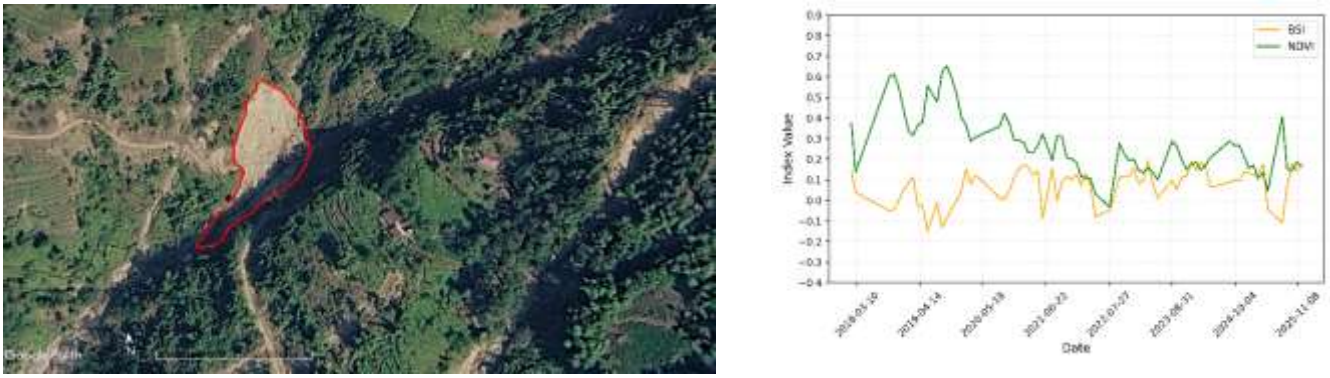


*Figure C-4: Landslide and corresponding BSI & NDVI time series analysis at (Latitude: 26°58'47.61"N, Longitude: 87°54'54.98"E)*


*Figure C-5: Landslide and corresponding BSI & NDVI time series analysis at (Latitude: 26°58'49.40"N, Longitude: 88° 6'20.96"E)*

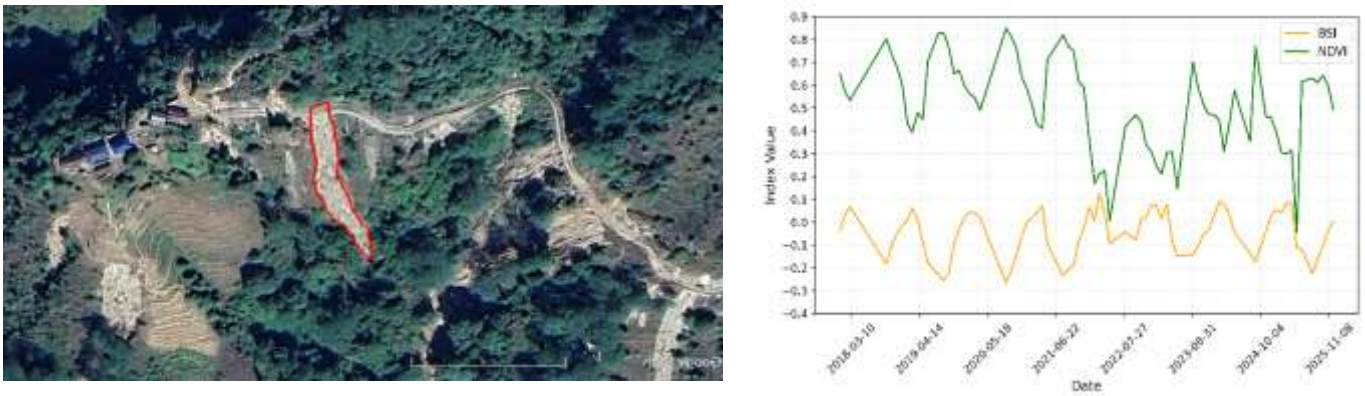


*Figure C-6: Landslide and corresponding BSI & NDVI time series analysis at (Latitude: 27° 3'27.06"N, Longitude: 87°59'27.45"E)*

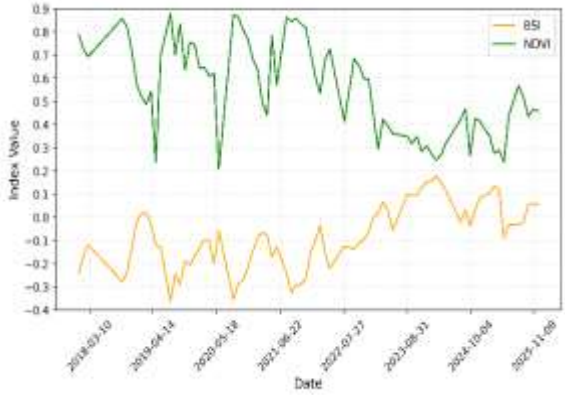


*Figure C-7: Landslide and corresponding BSI & NDVI time series analysis at (Latitude: 26°56'26.58"N, Longitude: 88° 3'9.55"E)*


*Figure C-8: Landslide and corresponding BSI & NDVI time series analysis at (Latitude: 26°49'51.83"N, Longitude: 87°56'21.81"E)*

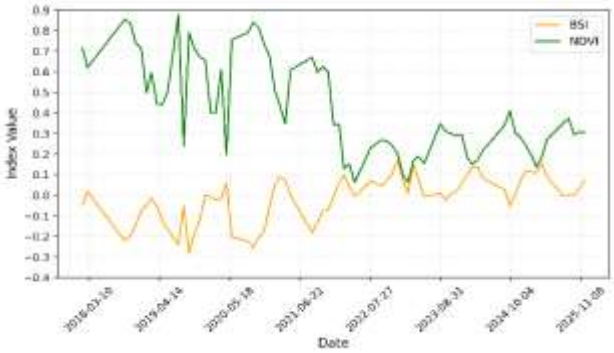


*Figure C-9: Landslide and corresponding BSI & NDVI time series analysis at (Latitude: 26°55'35.94"N, Longitude: 87°41'34.73"E)*

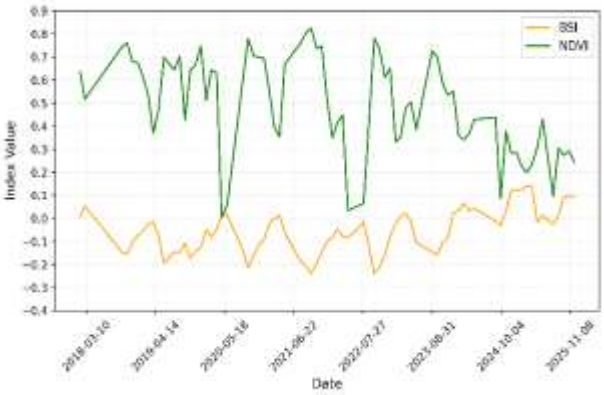


*Figure C-10: Landslide and corresponding BSI & NDVI time series analysis at (Latitude: 27° 0'22.67"N, Longitude: 87°43'51.21"E)*

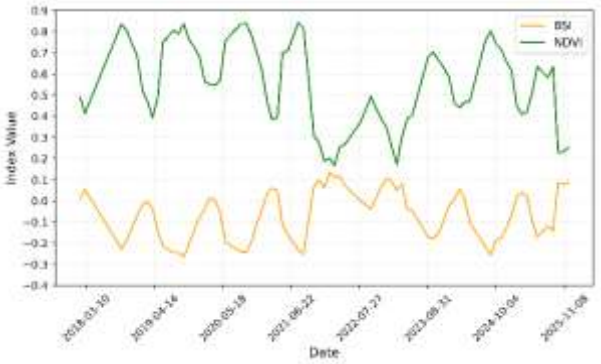


*Figure C-11: Landslide and corresponding BSI & NDVI time series analysis at (Latitude: 26°56'16.64"N, Longitude: 87°44'59.16"E)*

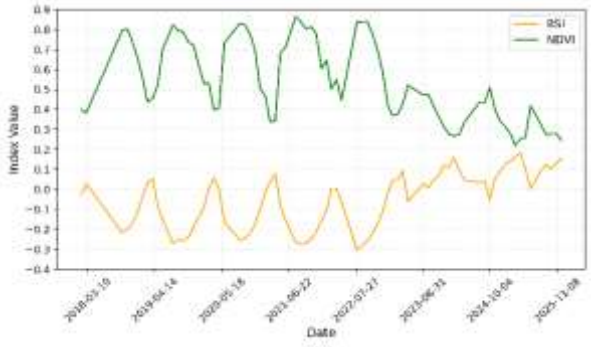


*Figure C-12: Landslide and corresponding BSI & NDVI time series analysis at (Latitude: 26°48'38.24"N, Longitude: 87°54'19.48"E)*

## Appendix D: Certificate of Conference Paper

774

# IOE Graduate Conference

## Certificate of Participation

This certificate is awarded to

*Suman Bahadur basnet*

in recognition of an invaluable contribution to
the academic discourse and research dessimination
at the 18th IOE Graduate Conference held from May 7 to 9, 2026
organized by Pulchowk Campus, Lalitpur, Nepal
through the Paper Presentation entitled

*"Rainfall-Induced Cascading Hazard Modeling: an Integrated Study of Landslides, Floods, and Soil Erosion in the Kankai Basin, Nepal."*

Prof. Sangeeta Singh
Conference Convener

Prof. Sanjay Uprety
Champus Chief, Pulchowk Campus

Prof. Sushil Bahadur Bajracharya
Dean, Institute of Engineering

## Appendix E: Plagiarism Report of the Thesis

# Suman Bahadur Basnet

## Rainfall-Induced cascading Hazard Modeling:An Integrated Study of Landslides,Floods and Soil Erosion in the Kankai Basi...

Tribhuvan University

### Document Details

Submission ID
trn:oid:::3117:585586899

Submission Date
May 3, 2026, 8:59 AM GMT+5:45

Download Date
May 3, 2026, 3:17 PM GMT+5:45

File Name
Final thesis suman for plagiarism checking, ioe.pdf

File Size
9.6 MB

109 Pages

24,804 Words

146,605 Characters



# 11% Overall Similarity

The combined total of all matches, including overlapping sources, for each database.

### Filtered from the Report

- Bibliography
- Quoted Text
- Cited Text
- Small Matches (less than 8 words)

### Match Groups

**224** Not Cited or Quoted 11%
Matches with neither in-text citation nor quotation marks

**0** Missing Quotations 0%
Matches that are still very similar to source material

**0** Missing Citation 0%
Matches that have quotation marks, but no in-text citation

**0** Cited and Quoted 0%
Matches with in-text citation present, but no quotation marks

### Top Sources

8% Internet sources
9% Publications
0% Submitted works (Student Papers)

### Integrity Flags

**1 Integrity Flag for Review**

**Hidden Text**
10 suspect characters on 3 pages
Text is altered to blend into the white background of the document.

Our system's algorithms look deeply at a document for any inconsistencies that would set it apart from a normal submission. If we notice something strange, we flag it for you to review.

A Flag is not necessarily an indicator of a problem. However, we'd recommend you focus your attention there for further review.

त्रिभुवन विश्वविद्यालय
TRIBHUVAN UNIVERSITY
इन्जिनियरिङ्ग अध्ययन संस्थान
INSTITUTE OF ENGINEERING
पुल्चोक क्याम्पस
PULCHOWK CAMPUS
Accredited by University Grants Commission (UGC) Nepal 2020
5-521260
5-521611
5-522104
5-522809
पुल्चोक, ललितपुर ।
Pulchowk, Lalitpur

Date: May 8, 2026

**To Whom It May Concern:**

This is to certify that the paper titled "*Rainfall Induced Landslide Risk Assessment of Kankai River Basin, Nepal*" (Submission ID #774), with **Suman Bahadur Basnet** as the first author, was accepted through the peer-review process and has been presented at the 18th IOE Graduate Conference, organized at Pulchowk Campus, Lalitpur, Nepal, from May 7 to 9, 2026.

Please note that inclusion of the accepted manuscript in the conference proceedings is contingent upon timely compliance with any further editorial requirements during the publication process.

Prof. Sangeeta Singh
Convener
18th IOE Graduate Conference